THERMAL SIMULATIONS FOR THE PREDICTION OF POROSITY IN INVESTMENT CASTINGS FOR STELLITE GRADE SUPERALLOYS

By

CHRISTOPHER MARC HERMESMANN

B.A.Sc., The University of British Columbia, 1994

A THESIS SUBMITTED IN PARTIAL FULFILLMENT OF
THE REQUIREMENTS FOR THE DEGREE OF

MASTER OF APPLIED SCIENCE

in

THE FACULTY OF GRADUATE STUDIES

(Department of Metals and Materials Engineering)

We accept this thesis as conforming
to the required standard

THE UNIVERSITY OF BRITISH COLUMBIA

December, 1996

© Christopher Marc Hermesmann, 1996

In presenting this thesis in partial fulfilment of the requirements for an advanced degree at the University of British Columbia, I agree that the Library shall make it freely available for reference and study. I further agree that permission for extensive copying of this thesis for scholarly purposes may be granted by the head of my department or by his or her representatives. It is understood that copying or publication of this thesis for financial gain shall not be allowed without my written permission.

Department of Metals and Materials Engineering

The University of British Columbia
Vancouver, Canada

Date Jan 2/97

DE-6 (2/88)

Abstract

A computer model was constructed and run to predict the thermal history of a Stellite alloy investment casting prone to the formation of microporosity. The thermal history of the casting was utilized to calculate the thermal gradient at a specified temperature, the rate of cooling during solidification, and the solidification velocity. These parameters were combined in a manner consistent with the formulation of two different criteria (Niyama and L.C.C. criteria) used to predict porosity. The Niyama and L.C.C. criteria successfully predicted the distribution of porosity found in the actual investment casting. Several new casting configurations were designed and modeled on computer until a configuration was constructed that predicted very little or zero porosity in the problematic areas. A new casting configuration, similar to the one designed in this study, was designed and cast by the industrial sponsor. The computer simulation of the casting configuration by the industrial sponsor predicted a small pocket of microporosity. Upon examination, some microporosity, consistent with the predictions by the model, was discovered. The finite element modeling software (ProCAST™) and the Niyama and the L.C.C. criteria served as excellent tools for predicting porosity in Stellite alloy castings.

Table of Contents

	Page
Abstract	ii
Table of Contents	iii
List of Tables	v
List of Figures	vi
Nomenclature	xiii
Acknowledgments	xv
1. Introduction	1
1.1 A Brief History of the Investment Casting Process	1
1.2 Background of the Investment Casting Process	2
1.3 Purpose of the Present Study	3
1.4 Porosity Background	3
2. Literature Review	6
3. Scope and Objectives	19
3.1 Scope	19
3.2 Objectives	20
4. Experimental Methods	21
4.1 Experimental Castings	21
4.1.1 Experimental Methodology and Procedures	22
4.2 Assessment of Porosity	24
4.2.1 X-ray Analysis of Porosity	25
4.2.2 Microstructural Assessment of the Porosity	26
5. Mathematical Model Formulation	33
5.1 Mathematical Formulation	33
5.2 Mathematical Model Development	34
5.2.1 Building the Finite Element Mesh	34
5.3 Pre-Process FEM in PreCAST	35
5.4 Post-Process Mathematical Formulations in PostCAST	36
6. Sensitivity Analysis and Model Validation	38
6.1 Sensitivity Analysis	38
6.1.1 Metal/Mould Interface Heat Transfer Coefficient	38
6.1.2 Mould Conductivity	40
6.1.3 Mould/Air Interfacial Heat Transfer Coefficient	41
6.1.4 Metal Initial Temperature	41
6.1.5 Mould Preheat Temperature	41
6.1.6 Stellite 3 Material Properties	42

6.2 Discussion of Results 42
6.2.1 Validation of Mould Shell Properties and Heat Transfer Coefficient Between the Mould and the Air (No Liquid Metal Present) 42
6.2.2 Validation of the Stellite 3 Properties and the Heat Transfer Coefficient Between the Mould and the Metal (Liquid Metal Present) 43
6.3 Summary 45

7. Investment Casting Thermal Simulation Results 57
7.1 Two Dimensional Model of the Valve Seal showing Porosity 57
7.2 Partial Three-Dimensional Model of the Diesel Valve Seal Showing Porosity 60
7.3 Heat Flux at the Inner Mould Surface 62

8. Reconfiguring the Mould to Obtain Zero Porosity using Modeling Techniques 74
8.1 Feeding the Diesel Valve Seat Casting Using Two Ingates 74
8.2 Feeding the Diesel Valve Seal Using Three Inner Ingates 76
8.3 Feeding the Diesel Valve Seal Using Four Inner Ingates 76
8.4 Discussion 77
8.5 Feeding the Diesel Valve Seal from the Top Using Four Ingates 78
8.6 Examination of Porosity in the Optimized Casting 80
8.7 Advantages and Disadvantages for the New Casting Configuration 80

9. Future Work 103

10. Summary and Conclusions 57

11. References 106

List of Tables

Table 4-1 Transfer time from the preheat furnace to the pouring of molten metal. 28

Table 4-2 The distribution of porosity in the ring casting measured as arc length and depth relative to the inner metal surface. Refer to Figure 4-3 for an illustrative description. 28

Table 6-1 Sensitivity Analysis Parameters 46

Table 6-2 Sensitivity Analysis Results 46

Table 6-3 Measured thermocouple depth relative to the outside of the cylindrical casting. 47

Table 6-4 Physical Properties of the Investment Mould[20] 47

Table 6-5 Boundary Conditions Between the Mould and the Air 47

Table 6-6 Physical Properties of Stellite Grade 3 48

Table 8-1 Summary of porosity predictions for the various models and the actual porosity found in the two castings (one outer feed ingate and four top feed ingates) 82

Table 8-2 The approximate weight of metal to make a single diesel valve seal (including gating, downsprue, and casting, this value does not take into account the pouring cup) 83

List of Figures

Figure 1-1 A diagram representing the investment casting process from pattern making to final inspection.[2] 5

Figure 1-2 Schematic representation of possible feeding mechanisms during solidification.[3] 5

Figure 2-1 Measured and predicted porosity in a 2 in. chilled casting by Suri *et al.*[8] 14

Figure 2-2 The temperature gradient (°C/cm) at the end of solidification from a finite difference model of a turbine casing casting. Note X indicates the location of actual shrinkage[11] 14

Figure 2-3 The temperature gradient (°C/cm) at the end of solidification from a finite difference model of a turbine casing casting with a chill. No Shrinkage was detected. 15

Figure 2-4 The Niyama criteria mapping from a two dimensional finite difference model of a ring casting; Note: X indicates the location of actual shrinkage.[12] 15

Figure 2-5 The effect of the calculated solidification time on the critical value of $G/\sqrt{R}$ as determine from experimental data.[12] 16

Figure 2-6 The correlation between the thermal gradient and porosity content for two casting configurations (D-15 and D-25) from a study by Lee *et al.*[13] 16

Figure 2-7 The correlation between the solidus velocity and porosity content for two casting configurations (D-15 and D-25) from a study by Lee *et al.*[13] 17

Figure 2-8 The correlation between the solidification time and porosity content for two casting configurations (D-15 and D-25) from a study by Lee *et al.*[13] 17

Figure 2-9 The correlation between porosity content and the feeding efficiency parameter (L.C.C.) from a study by Lee *et al.*[13] 18

Figure 2-10 Schematic illustration showing the distance through which liquid metal must flow to the solidification front with a steep (Δd_1) and shallow (Δd_2) thermal gradients. 18

Figure 4-1 A 2-d diagram showing the mould configuration used to validate the metal and mould (shaded) physical properties and the heat transfer boundary conditions in ProCAST™ 29

Figure 4-2 A schematic showing the mould configuration for the Stellite 3, Diesel Valve Seats used for the validation of porosity prediction. 29

Figure 4-3 Schematic Diagram showing the Distribution of Porosity (shaded area) in the Diesel Valve Seal. 30

Figure 4-4 A macro-photograph showing a transverse cut plane through the approximate center of the diesel valve seals showing the extent and distribution of porosity. (unetched) 31

Figure 4-5 A microphotograph of a transverse section through the approximate center of the diesel valve seal across from the ingate showing the depth and distribution of the microporosity from Figure 4-4. (unetched, mag. 6.4x) 31

Figure 4-6 A close-up of the porosity from Figure 4-5 showing the size and depth of porosity in the diesel valve. (etched, mag. 100x) 32

Figure 4-7 A histogram representing the percentage of porosity from the microstructure in Figure 4-5. 32

Figure 6-1 A graphical representation of gap formation at the mould/metal interface at the onset of solidification for a simple cylindrical mould configuration. 48

Figure 6-2 Varying the Mould/Metal Heat Transfer Coefficient Parameter from a base value of 2500 $W/m^2/°C$ to 1250 $W/m^2/°C$. 49

Figure 6-3 Varying the Mould/Metal Heat Transfer Coefficient Parameter from a base value of 2500 $W/m^2/°C$ to 5000 $W/m^2/°C$. 49

Figure 6-4 A schematic diagram showing the inhomogeneous gap formation in a simple two dimensional model. 50

Figure 6-5 Model results by varying the Mould Conductivity from the base value of 1.0 W/m/K to 1.2 W/m/K. 50

Figure 6-6 Model results by varying the Metal Initial Temperature from the base value of 1482 °C (2700 °F) to 1532 °C (2790 °F). 51

Figure 6-7 Model results by varying the mould preheat temperature from a base value of 1037 ° C (1900 °F) to 987 °C (1810 °F). 51

Figure 6-8 Model results by varying the air/mould heat transfer coefficient from a base value of 20 $W/m^2/°C$ to 40 $W/m^2/°C$. 52

Figure 6-9 The one-dimensional axis symmetric computer model configuration used to simulate the cylindrical test mould air cool experiment. 52

Figure 6-10 Validation of the mould physical properties and the heat transfer coefficient between the mould and the air against thermocouple data. 53

Figure 6-11 One-dimensional axis symmetric computer model configuration used to simulate the cylindrical test mould solidification experiment 53

Figure 6-12 Thermocouple and thermal simulation (#1) results for the test cylindrical mould, mould preheat=1800 °F, metal temperature=2700 °F, refer to Table 6-3 for thermocouple position. 54

Figure 6-13 Thermocouple and thermal simulation (#2) results for the test cylindrical mould, mould preheat=1800 °F, metal temperature=2700 °F, refer to Table 6-3 for thermocouple position 54

Figure 6-14 Graphical representation of the heat transfer coefficient between the metal and mould as a function of the interfacial temperature. 55

Figure 6-15 Variation in heat capacitance with temperature 55

Figure 6-16 Variation in conductivity with temperature 56

Figure 7-1 Two-dimensional finite element mesh used to simulate the heat flow through a transverse section of a single cluster for an investment cast diesel seal. 65

Figure 7-2 Contour Plots showing the front of the solidus isotherm for a single diesel valve seal at a)the onset of solidification, b) 20 seconds into solidification, c) 140 seconds into solidification d) 960 seconds into solidification (the mould is not shown in the diagram) 66

Figure 7-3 Diagram showing the removal of heat through radiation and heat conduction/convection from the outer surface of the mould. 67

Figure 7-4 Solidification Time (sec.) for the two-dimensional analysis of the diesel valve seal. 67

Figure 7-5a A contour plot showing the thermal gradient (°C/cm) when any particular element begins to solidify (1320 °C) 68

Figure 7-6 A contour plot showing the thermal gradient (°C/cm) at 70% solidified (1260 °C) 69

Figure 7-7 Two dimensional analysis showing the porosity prediction (in red) for a single diesel valve casting using the Niyama criteria ($°C^{1/2}/cm\ min^{1/2}$). 70

Figure 7-8 Diagram showing the boundary conditions for the partial three-dimensional model used to simulate the diesel valve casting 70

Figure 7-9 The solidification time (sec.) of a transverse slice through the diesel valve seal. 71

Figure 7-10 Thermal Gradient contour plot of a transverse slice through the diesel valve seal. 71

Figure 7-11 A transverse slice of the diesel valve seal showing the porosity prediction (in red) using the Niyama criteria ($°C/cm/min^{1/2}$), θ = 116.0, d = 5.9 mm 72

Figure 7-12 A transverse slice through the diesel valve seal showing the porosity prediction (in red) using the L.C.C criteria ($°C\ min^{5/3}/cm^2$), θ=107°, d=6.2 mm 72

Figure 7-13 Graph showing the two sets Thermal Histories for Nodes 3280, 3279, 3370. No Flux assumes perfect insulation at the mould inner surface, Flux assumes an air/mould heat transfer coefficient. 73

Figure 7-14 Results of a transverse slice through the diesel valve seal showing the porosity prediction (in red) using the Niyama criteria ($°C^{1/2}/cm/min^{1/2}$), assumes no heat flux through the inner mould surface. θ=101°, d=3.46 mm. 73

Figure 8-1There dimensional diagram for a new diesel valve seal configuration using two ingates to feed the casting. 84

Figure 8-2 Three dimensional model used to simulate the configuration in Figure 8-1; a) without the mould shell, b) with the mould shell showing the boundary conditions. 84

Figure 8-3 Solidification Time contour plot through the mid-plane of the Diesel Valve Seal Casting using two ingates to feed the casting. 85

Figure 8-4 Thermal Gradient (°C/cm) Contour Plot through the mid-plane of the Diesel Valve Seal Casting using two ingates, Thermal Gradient taken when an element obtains 70% volume fraction Solid (1260 °C). 85

Figure 8-5 Niyama criteria ($°C^{1/2}$ $min^{1/2}$/cm) Contour Plot through the mid-plane of the Diesel Valve Seal, Thermal Gradient (°C/cm) taken at 1260 °C 86

Figure 8-6 L.C.C. criteria (°C $min^{5/3}/cm^2$) Contour Plot through the mid-plane of the Diesel Valve Seal, Thermal Gradient (°C/cm) taken at 1260 °C 86

Figure 8-7 Three dimensional schematic of the new casting configuration using three ingates to feed the casting. The mould is not included in this diagram. 87

Figure 8-8 The model configuration using three ingates to feed the casting. This mould is not included in this diagram. 87

Figure 8-9 Solidification Contour Plot through the mid-plane of the Diesel Valve Seal using three ingates to feed the casting. 88

Figure 8-10 Thermal Gradient (°C/cm) Contour Plot through the mid-plane of the Diesel Valve Seal Casting using three ingates, Thermal Gradient taken when an element obtains 70% volume fraction Solid (1260 °C). 88

Figure 8-11 Niyama criteria ($°C^{1/2}$ $min^{1/2}$/cm) Contour Plot through the mid-plane of the Diesel Valve Seal using three ingates, Thermal Gradient (°C/cm) taken at 1260 °C 89

Figure 8-12 L.C.C. criteria (°C $min^{5/3}/cm^2$) Contour Plot through the mid-plane of the Diesel Valve Seal using three ingates, Thermal Gradient (°C/cm) taken at 1260 °C 89

Figure 8-13 Three dimensional schematic of the new casting configuration using four ingates to feed the casting from the inner surface. The mould is not included in this diagram. 90

Figure 8-14 Three dimensional model diagram using four ingates to feed the casting from the inner surface. The mould is not included in this diagram. 90

Figure 8-15 Solidification Time contour plot through the mid-plane of the casting using four inner surface ingates to feed the diesel valve seal. 91

Figure 8-16 Thermal Gradient (°C/cm) Contour Plot through the mid-plane of the Diesel Valve Seal Casting using four inner surface ingates, Thermal Gradient taken when an element obtains 70% volume fraction Solid (1260 °C). 91

Figure 8-17 Niyama criteria ($°C^{1/2}$ $min^{1/2}$/cm) Contour Plot through the mid-plane of the Diesel Valve Seal using four inner surface ingates, Thermal Gradient (°C/cm) taken at 1260 °C 92

Figure 8-18 L.C.C. criteria (°C $min^{5/3}/cm^2$) Contour Plot through the mid-plane of the Diesel Valve Seal using four inner surface ingates, Thermal Gradient (°C/cm) taken at 1260 °C 92

Figure 8-19 Three dimensional schematic of the new casting configuration using four top feeding ingates to feed the casting. The mould is not included in this diagram. 93

Figure 8-20 Three dimensional model diagram using four top feeding ingates to feed the casting. The mould is not included in this diagram. 93

Figure 8-21 Solidification Time contour plot through the mid-plane of the casting using four top feeding ingates to feed the diesel valve seal. 94

Figure 8-22 Thermal Gradient (°C/cm) Contour Plot through the mid-plane of the Diesel Valve Seal Casting using four top feeding ingates, Thermal Gradient taken when an element obtains 70% volume fraction Solid (1260 °C). 94

Figure 8-23 Niyama criteria ($°C^{1/2}$ $min^{1/2}$/cm) Contour Plot through the mid-plane of the Diesel Valve Seal using four top feeding ingates, Thermal Gradient (°C/cm) taken at 1260 °C 95

Figure 8-24 L.C.C. criteria (°C $min^{5/3}/cm^2$) Contour Plot through the mid-plane of the Diesel Valve Seal using four top feeding ingates, Thermal Gradient (°C/cm) taken at 1260 °C. 95

Figure 8-25 Three dimensional model diagram using three layers of four top feeding ingates to simulate the new casting configuration from Deloro Stellite. The mould is not included in this diagram. 96

Figure 8-26 Thermal Gradient (°C/cm) Contour Plot through the mid-plane of the Diesel Valve Seal Casting using four top feeding ingates, model incorporates three layers of the casting, Thermal Gradient taken when an element obtains 70% volume fraction Solid (1260 °C). 97

Figure 8-27 Niyama criteria ($°C^{1/2}$ $min^{1/2}/cm$) Contour Plot through the mid-plane of the Diesel Valve Seal using four top feeding ingates, model incorporates three layers of the casting, Thermal Gradient (°C/cm) taken at 1260 °C 98

Figure 8-28 L.C.C. criteria (°C $min^{5/3}/cm^2$) Contour Plot through the mid-plane of the Diesel Valve Seal using four top feeding ingates, model incorporates three layers of the casting,Thermal Gradient (°C/cm) taken at 1260 °C. 99

Figure 8-29 Schematic diagram of the diesel valve seal showing the circumferential angle and depth of porosity for the model results in Table 8-1. 100

Figure 8-30 A quarter section of the new Diesel Valve Seal casting showing an obvious network of porosity in the downsprue. No visible porosity in the casting at this magnification. 101

Figure 8-31 A magnified photograph of microporosity found on the surface of the casting at Point A from Figure 8-30 . (unetched, mag.=12.8x) 101

Figure 8-32 A close up of the porosity found in Figure 8-31. Porosity = 2.75 % area (etched, mag.=100x) 102

Nomenclature

Chapter 2

P_a	pressure at the groove entrance for flow in a pipe (eqn. 2-1)
P_L	pressure at the root of groove for flow in a pipe (eqn. 2-1)
V	velocity of liquid flow into groove (eqn. 2-1)
μ	viscosity of liquid
L	length of pipe (eqn. 2-1)
r	radius of pipe (eqn. 2-1)
P_a	pressure in riser (eqn. 2-2)
P_L	pressure at L (eqn. 2-2)
L	length of casting (eqn. 2-2)
β'	$=\beta/(1-\beta)$
β	shrinkage due to solidification
t	tortuosity factor
n	number of flow channel
R	cylinder radius
r	radius of liquid channel
λ	heat flow constant[5]
v_x	velocity of liquid metal in the x-direction (eqn. 2-3)
K	permeability constant
g_L	volume fraction of liquid
dP	pressure drop due to fluid flow (eqn. 2-3)
τ	tortuosity factor (eqn. 2-3)
ΔT	the freezing range of the alloy (eqn. 2-4)
ρ_L	liquid density
G	thermal gradient
V_s	solidification front growth velocity (eqn. 2-4)
D	primary dendrite are spacing (eqn. 2-4)

Nomenclature (cont.)

Chapter 5

ρ	density
H	enthalpy term
C_p	Heat Capacitance
T	Temperature
k	thermal conductivity
t	time
$\frac{\partial}{\partial x}, \frac{\partial}{\partial y}, \frac{\partial}{\partial z}$	partial derivative with respect to x, y, z
L	latent heat of solidification
f_s	fraction of solid
L	rate of cooling (eqn. 5-4)
R	solidification velocity
G	thermal gradient

Acknowledgments

I would like to thank my adviser, Dr. Steve Cockcroft for his support, guidance and patients during the course of my thesis and Mr. Bob Dawson of Deloro Stellite Inc. for providing the opportunity to run my experiments in an industrial setting. I am also indebted to a host of other people; in particular my Father (Fred), Mother (Lorraine), and my siblings (Caroline, Kirsten and Micah) for their unfailing support, my office mates for their good spirits, and of course all my friends who have helped me along the way. I would also like to acknowledge the Natural Sciences and Engineering Research Council (NSERC) for providing the necessary funding for this project.

1. Introduction

1.1 A Brief History of the Investment Casting Process

Investment casting, otherwise known as the lost wax process or precision casting, is one of the oldest metal forming techniques. Over 4000 years ago during the Shang Dynasty, investment castings of various statuary and jewelry were made[1]. Other early investment castings include delicate bronze statues from China dating back 1500 years and jewelry by Aztec goldsmiths from Mexico made well before Columbus discovered America[2].

Earlier this century, investment casting made its first commercial appearance in the dental sector with the manufacturing of gold fillings and crowns. However, the true potential of this casting process was not fully recognized until the Second World War when components for high altitude bombers and fighters were in demand. Investment cast turbine blades, fabricated from a cobalt-chrome alloy which offered strength in a very hot, high-stress environment, found their way into jet engines. In addition to strength, the investment casting techniques offered excellent as-cast surface finishes which negated or minimized the need for supplemental machining or finishing.

After World War II, the demand for investment casting grew throughout the 1950's, predominantly in aircraft and military applications. During the past several decades, many improvements in the investment casting process have been made through the use of moulding robotics and better moulding materials. These improvements have made it economically feasible to use this process in areas outside of the aircraft and the

military sectors. Investment casting is being discovered by more and more industrial sectors seeking a process alternative for the production of cheaper and higher quality products.

1.2 Background of the Investment Casting Process

Fabrication of an investment mould incorporates a series of steps. The initial step is the construction of the wax "positive". This includes the wax pattern of the desired component(s), the feeding channels, gating, risers, and the pouring cup. These wax components are usually cast using an injection moulding process and then hand assembled. Depending on the size of the component, several parts can be assembled into a tree-like structure and cast simultaneously.

After the wax "tree" has been assembled, the next step is the application of ceramic coatings which will serve as the mould. The wax assembly is immersed in a ceramic slurry, which consists of very fine refractory flour or sand, and then allowed to air dry. This step is usually repeated. These initial ceramic layers form the face coat for the mould that may be used for a number of reasons including: to minimize chemical reaction between the liquid metal and the mould, to produce a desired surface finish, and to act as either a grain nucleation agent (multi-crystal castings) or as an inhibitor to the formation of nuclei (directional or single crystal castings). The backup coatings provide the structural integrity for the mould and contain coarser ceramic materials (usually sand or stucco) with the coarsest material on the exterior. Five to eight backup coatings are usually applied.

Once the investment mould is built, the mould is placed in a de-waxing chamber, and the wax is melted and/or burnt out leaving an empty core. Quite often the mould is then fired for strength and placed within a preheat furnace before pouring. The metal is then poured into the mould in either a vacuum or air atmosphere, depending on the metal. Once the metal has cooled, the mould is removed along with the metal distribution system and then may be further machined depending on the component requirements. A schematic representation of the investment casting process is shown in Figure 1-1.

1.3 Purpose of the Present Study

Investment casting, like many other casting processes, can produce surface and interior defects during processing, that lead to poor component performance and/or component rejection. Computer systems and modeling software have evolved over the years and have the capability to simulate the thermal histories of complex casting with a reasonable amount of accuracy. This study examined the capability of a commercially available software package to predict microporosity in a complex investment castings manufactured from a multi-component cobalt based alloy. Following validation of the model to predict porosity, the model was used to explore alternative mould designs/configurations to minimizing and/or eliminating porosity.

1.4 Porosity Background

Porosity in castings can be grouped into one of two broad categories (macroporosity or microporosity) on the basis of scale and mechanism of formation. Macroporosity is generally large in scale and forms as a result of solidification of a liquid

that has been encapsulated by a solidified material. The size of the resulting pore or cavity is dependent upon the volume of encapsulated liquid and the volume shrinkage associated with the liquid-to-solid phase transformation. Macroporosity is easily corrected by proper gates and risers within the mould and/or by using chills and/or exothermics to control the progress of solidification.

In contrast, microporosity forms interdendritically at the scale of the microstructure. Thus, its formation is more complex mechanically, more difficult to predict, and generally more difficult to correct. There are two primary sources microporosity: solute gas precipitation in the interdendritic liquid, and/or poor liquid feeding from volume shrinkage within the mushy zone. In an attempt to describe the latter, the different networks through which material must flow within the mushy zone have been subdivided into different regimes by Campbell[3], as illustrated schematically in Figure 1-2. (In this description, solid feeding is somewhat of a misnomer since it actually pertains to distortions as surface depressions[3] instead of feeding). The interdendritic regime is presently believed to be the most important to microporosity formation in most casting processes[3], since it offers the greatest resistance to liquid feeding during the crucial last stages of solidification. In comparison, the liquid and mass feeding regimes may be ignored since they have much lower feeding resistances.[4]

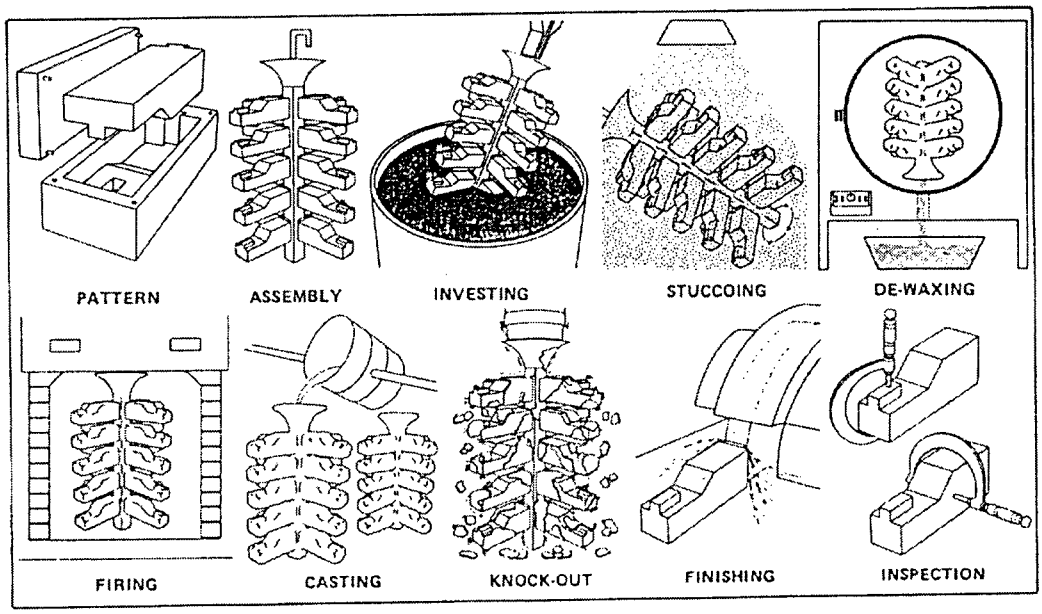

Figure 1-1 A diagram representing the investment casting process from pattern making to final inspection.[2]

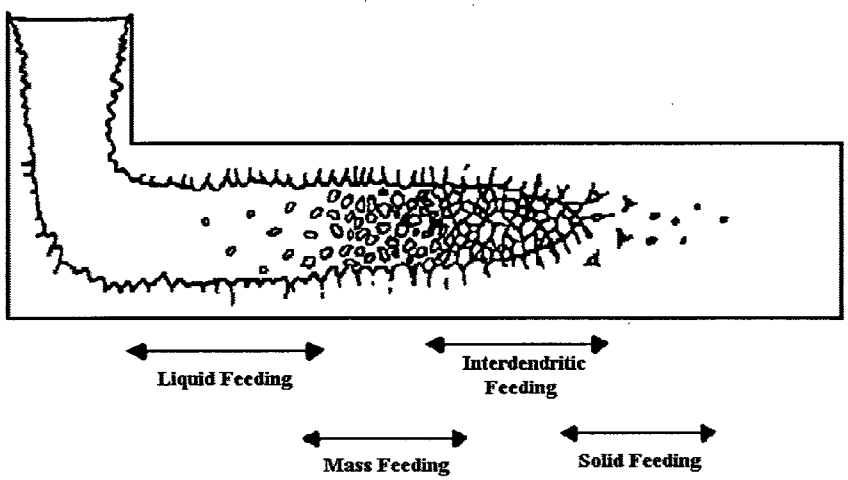

Figure 1-2 Schematic representation of possible feeding mechanisms during solidification.[3]

2. Literature Review

One of the first attempts to understand and characterize porosity formation from a semi-fundamental mathematical approach was undertaken by Piwonka and Flemings.[5] Their investigation involved the application of D'Arcy's Law of laminar flow through a pipe (eqn. 2-1) to mathematically describe the flow of liquid metal through a dendritic structure (eqn. 2-2). Using this approach, they were able to quantify the pressure drop required for flow through a dendritic array while taking into account the number of flow channels (n), tortuosity (t), liquid metal viscosity (μ) and a number of other variables. Their work demonstrated that "centerline" shrinkage and microporosity forms as a result of the pressure difference caused by the restriction of liquid metal movement through the mushy zone to the solidification front. They also demonstrated the influence of dissolved gases and surface tensions in the precipitation and distribution of porosity. With these two porosity sources in mind, they attempted to predict the resulting porosity radius in several castings, but their predictions achieved only limited agreement with actual observations.

$$P_a - P_L = -\frac{8V_s \mu L}{r^2} \qquad \text{eqn. 2-1}$$

$$P_a - P_L = \frac{32\mu\beta'\lambda^2 L^2}{r^4}\left(\frac{t^2}{\pi R^2 n}\right) \qquad \text{eqn. 2-2}$$

Davies[6] studied the formation of centerline porosity in the cross section of a plate using simple two-dimensional computer modeling techniques and employing the

application of Darcy's Law in a post-model analysis calculation. Based on his results, Davies was able to calculate the critical feeding distance for several alloy systems. The critical feeding distance is the maximum distance a riser can feed liquid metal to the solidification front while avoiding the formation of porosity. Davies also showed that for alloys with a large solidification temperature range, mass feeding to the solidification front occurs until there is a network of solidified crystals that prevent further feeding. The volume percent of solidified crystals to prevent further feeding varies with alloy content and grain size, but for most alloy systems, this value is approximately 70% solid.

Minakawa *et al.*[7] used the methodology of Piwonka *et al.*[5] to formulate the flow velocity of a liquid through interdendritic channels at steady state using eqn. 2-3

$$v_x = -\frac{K}{\mu g_L}\frac{dP}{dx} \qquad \text{eqn. 2-3}$$

where: $K = \frac{g_L^2}{8n\pi\tau^3}$

Their approach was applied to a simple two-dimensional plate configuration with a riser at one end and zero heat flow in the third dimension (a valid assumption for simple plate geometries). They were able to achieve good agreement between the model predictions and the porosity distribution from plate castings obtained in a study by Pellini *et al.*[9,10]. However, the application of porosity models to complex alloys and casting configurations presents a number of difficulties. One difficulty is that fluid flow analysis requires quantification of variables such as the number of flow channels, tortuosity, and viscosity These parameters are difficult to obtain or estimate and especially in complex alloy

systems. For example, the viscosity of the liquid metal will change significantly as solidification proceeds due to solute segregation, especially in the solute rich, interdendritic, areas at high volume fraction of solid. Furthermore, at high fraction solids, flow may also be restricted by surface tension effects. One drawback of adopting an empirical approach is it is only applicable to the conditions for which it was developed. A change in the casting variables results in a change in the dendritic structure, which in turn influences the key variables. Thus, for broad applications, the approach by Minakawa *et al.*[7] requires prediction of dendritic growth morphologies and mass transport, as a function of casting process variables, as well as the relation between composition, temperature and viscosity.

In a different, more empirical approach, Suri *et al.*[8] developed a porosity parameter based on the feeding resistance number (FRN) defined in eqn. 2-4. Their criteria attempts to account for such variables as liquid viscosity, solidification shrinkage, primary dendrite arm spacing (in either columnar or equiaxed dendrites), and solidus velocity. The result was a dimensionless number, which was used to assess the onset of microporosity, based on its magnitude relative to some critical threshold.

$$FRN = \frac{n\mu\Delta T}{\rho_L G V_s \beta D^2} \qquad \text{eqn. 2-4}$$

For example, Suri *et al.*[8] used the FRN criteria to predict measured porosity in plate castings by correlating the FRN with percent porosity using a second order polynomial. The resulting correlation from eqn. 2-5, is shown in Figure 2-1.

$$\text{Porosity } \% = -23.9 + 9.6e\text{-}6 \cdot FRN - 9.1e\text{-}13 \cdot (FRN)^2 \qquad \text{eqn. 2-5}$$

They also attempted to apply the FRN criteria to more complex aluminum castings with varying degrees of success. Although the results from the aluminum castings look promising, there is some concern with the application of the FRN and the applicability of the polynomial coefficients of eqn. 2-5 to other alloy systems and casting configurations. Another drawback with this approach is that it requires quantification of casting variables such as the liquid metal viscosity and the primary dendrite arm spacing, and this limits the model's applicability to specific alloy systems for which this information is available. Nevertheless, the FRN criteria by Suri *et al.*[8] seems to be quite effective in predicting porosity.

Some of the earliest work to link porosity to thermal history was done by Pellini[9] and Bishop and Pellini[10]. In their respective studies, they instrumented several rectangular and circular castings with thermocouples, in an attempt to obtain a better understanding of solidification kinetics and the correlation between thermal history and porosity formation. Based on their results, they were able to show that, in some steels, areas with very shallow thermal gradients at or near the solidus temperature, developed porosity. Specifically, porosity was found to develop when the thermal gradient was between 1.3 to 2.6 °C/cm for cast bars and 0.2 to 0.4 °C/cm for cast plates in a steel alloy system. The reason for the geometry dependence was not discussed.

Niyama *et al.*[11] also used a thermal criterion to predict shrinkage porosity in steel castings, however, their criterion was based on thermal gradients predicted from a

computer analysis. The castings examined were more geometrically complex than those of Pellini *et al.*[9,10] which made Niyama's analysis more applicable to the complex configurations typical of investment castings. Niyama *et al.*[11] examined a gas turbine casing casting with porosity found in its middle. A two-dimensional finite difference (FD) model was constructed and run to compute the casting's thermal history. The results presented in Figure 2-2 show the thermal gradients in the casting at the end of solidification and the location of porosity found in the actual casting. The investigators reported that porosity was found in association with thermal gradients below approximately 2 °C/cm. Based on these results, the gas turbine casing mould model was reconfigured using chills and rerun to assess the extent to which the temperature gradient had increased. The result was a new gas turbine casing mould that produced no detectable shrinkage in the actual casting (Figure 2-3) designed with the aid of a computer.

In their investigation, Niyama *et al.*[11] raised some concerns regarding the uncertainty of the specific temperature at which the thermal gradient is evaluated. They correctly pointed out that the temperature gradient in the mushy zone changes as solidification proceeds, and thus the gradient should be calculated at a specified temperature or solid fraction.

Comparing the work of Niyama *et al.*[11] with that of Pellini [9] and Bishop and Pellini[10], there is nothing fundamentally obvious that would account for their differences; Niyama predicted porosity will occur at thermal gradients below 2 °C/cm for steel gas turbine casings while Pellini and Bishop predicted porosity below 1.3 to 2.6 °C/cm for

cast steel bars and 0.2 to 0.4 °C/cm for cast steel plates. The only difference between these two studies, was possibly the effect of alloy compositions and/or casting configurations on the critical thermal gradient for porosity formation.

Expanding further on their earlier work, Niyama *et al.*[12] developed the Niyama criteria for porosity prediction, which was derived in part from Darcy's Law of fluid flow through porous media[5]. The parameter on which the criterion is based is presented as eqn. 2-6 and is the ratio of the thermal gradient (G) to the inverse square root of the cooling rate (R).

$$\text{Niyama Criterion} = \frac{G}{\sqrt{R}} \quad (\sqrt{°C} \cdot \sqrt{min}/cm) \qquad \text{eqn. 2-6}$$

Using an approach similar to their previous study[11], Niyama *et al.*[12] examined a ring casting using a two-dimensional finite difference thermal model and produced a contour map (Figure 2-4) which showed the variation in the Niyama parameters (eqn. 2-6) with the position in the casting. By correlating the model results with the distribution of porosity found in the experimental castings, they showed that areas with a $G/R^{1/2}$ ratio of less than about 1 $°C^{1/2} \cdot min^{1/2}/cm$, were highly prone to porosity nucleation (Figure 2-4). They went on to demonstrate experimentally (Figure 2-5) that the Niyama criteria of approximately 1 $°C^{1/2}\ min^{1/2}/cm$ was applicable to various alloy grades as well as casting sizes and shapes. The authors were careful to point out that their approach was highly empirical and that more refinement may be required before it can be applied to a wider range of alloys and casting configurations. In addition, this approach does not lend

itself well to the quantitative prediction of porosity (e.g. size and/or distribution), rather it is suitable for identifying regions within a casting that are prone to porosity formation.

In another study, Lee *et al.*[13] took a similar approach to that of Niyama *et al.*[12] by deriving a thermal based criteria for the prediction of porosity. Their parameter, defined in eqn. 2-7, is an semi-empirical formulation also derived using D'arcy's law and has been called the Feeding Efficiency Parameter F.E.P. (also referred as the L. C. C. criteria).

$$\text{Feeding Efficiency Parameter} = \frac{G \cdot t^{2/3}}{V_s} \quad (^{\circ}\text{C min}^{5/3}/\text{cm}^2) \qquad \text{eqn. 2-7}$$

The work of Lee *et al.*[13] focused on plate castings with varying lengths and riser sizes. The porosity content was calculated down the length of the casting and correlated with the thermal gradient (Figure 2-6), solidus velocity (Figure 2-7), solidification time (Figure 2-8), and the L.C.C. parameter (Figure 2-9). Their results demonstrated that areas in a casting with L.C.C. values of 1 °C $\text{min}^{5/3}/\text{cm}^2$ or less tend to contain porosity.

Although the two previous criteria used only thermally derived parameters (thermal gradient, solidification time and solidus velocity), these parameters can be representative of the solidification characteristics of the system. For example, the thermal gradient can be related to the length of the interdendritic feeding channel over which fluid flow occurs as illustrated in Figure 2-10 - e.g. the farther the feed liquid metal has to travel to the solidification front through the mushy zone (shallow thermal gradient), the greater the resistance to flow.

The solidification time (t) and the solidus velocity (V_s) have a bearing on the feeding rate. A shorter solidification time and/or a faster solidus velocity will result in a greater inflow rate of feed liquid metal to fill the areas undergoing solidification. Also, there is an effect on the scale of the microstructure and hence its tortuosity.

From the above discussion, it is clear that the semi-empirical approach of Niyama *et. al.*[12] and Lee *et. al.*[13], are better suited to investment castings than the more fundamentally based approaches of Minakawa *et al.*[14], Piwonka *et al.*[5] and Davies[6] because they require only a straightforward thermal analysis.

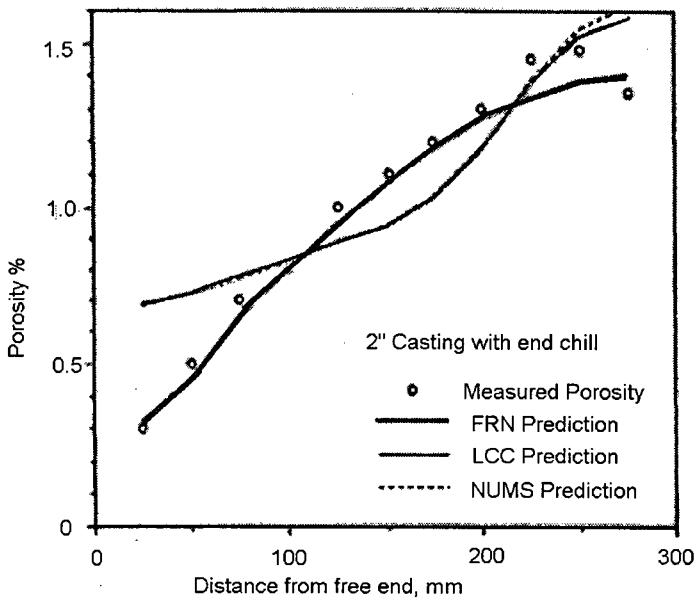

Figure 2-1 Measured and predicted porosity in a 2 in. chilled casting by Suri *et al.*[8]

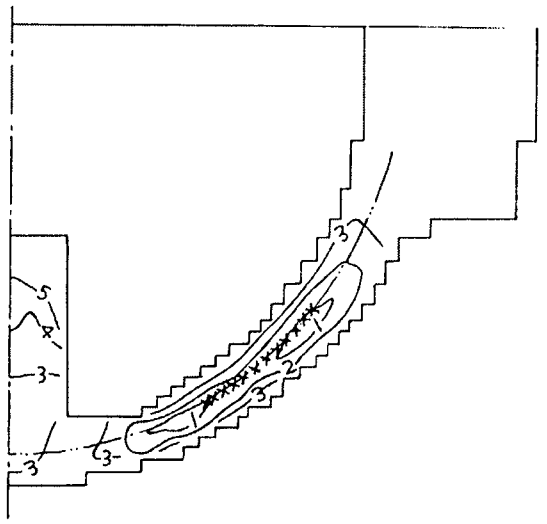

Figure 2-2 The temperature gradient (°C/cm) at the end of solidification from a finite difference model of a turbine casing casting. Note X indicates the location of actual shrinkage[11]

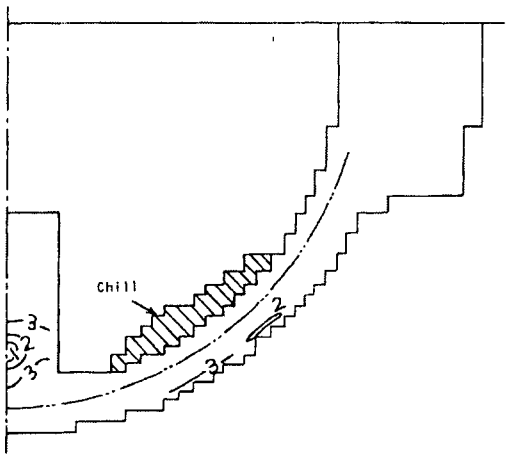

Figure 2-3 The temperature gradient (°C/cm) at the end of solidification from a finite difference model of a turbine casing casting with a chill. No Shrinkage was detected.

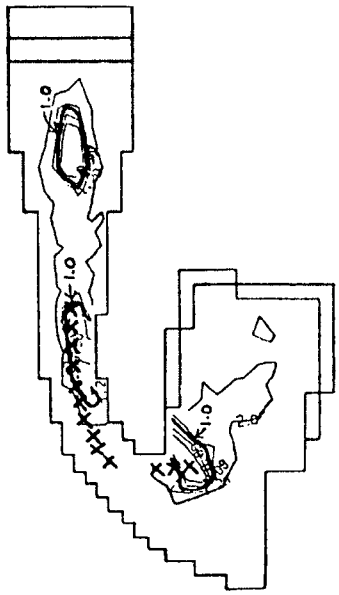

Figure 2-4 The Niyama criteria mapping from a two dimensional finite difference model of a ring casting; Note: X indicates the location of actual shrinkage.[12]

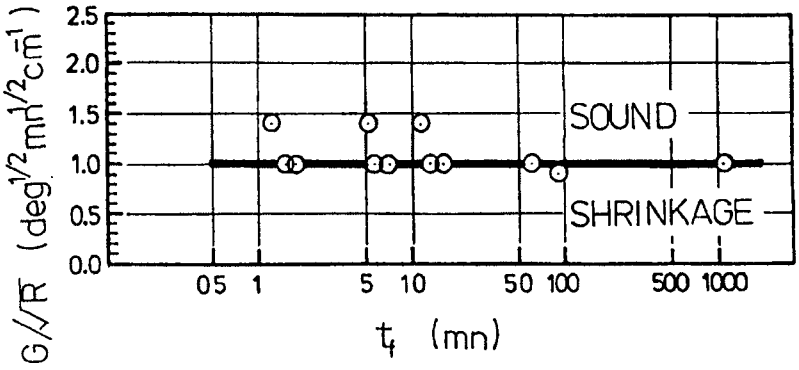

Figure 2-5 The effect of the calculated solidification time on the critical value of $G/\sqrt{R}$ as determine from experimental data.[12]

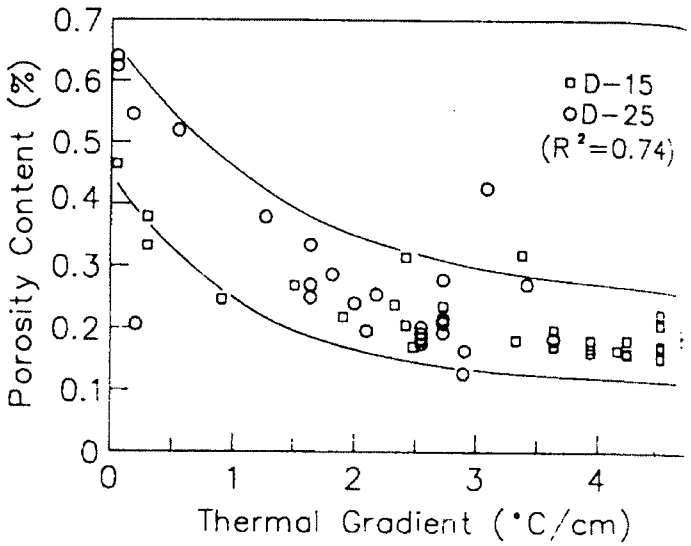

Figure 2-6 The correlation between the thermal gradient and porosity content for two casting configurations (D-15 and D-25) from a study by Lee *et al.*[13]

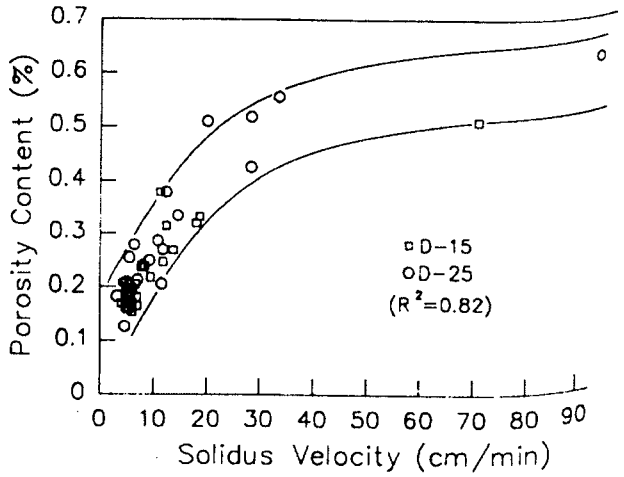

Figure 2-7 The correlation between the solidus velocity and porosity content for two casting configurations (D-15 and D-25) from a study by Lee *et al.*[13]

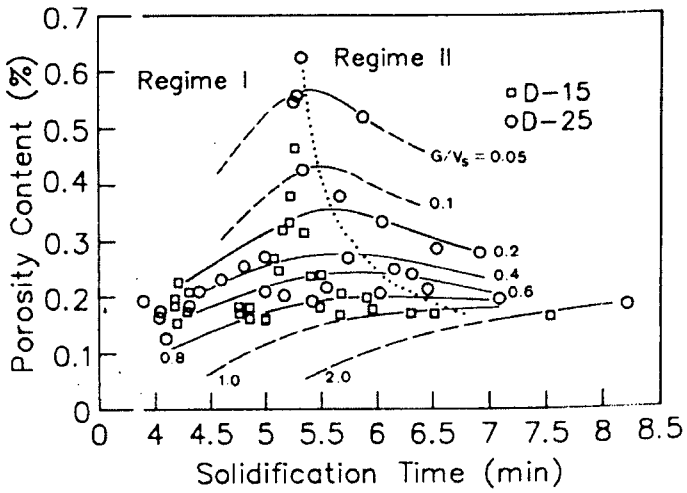

Figure 2-8 The correlation between the solidification time and porosity content for two casting configurations (D-15 and D-25) from a study by Lee *et al.*[13]

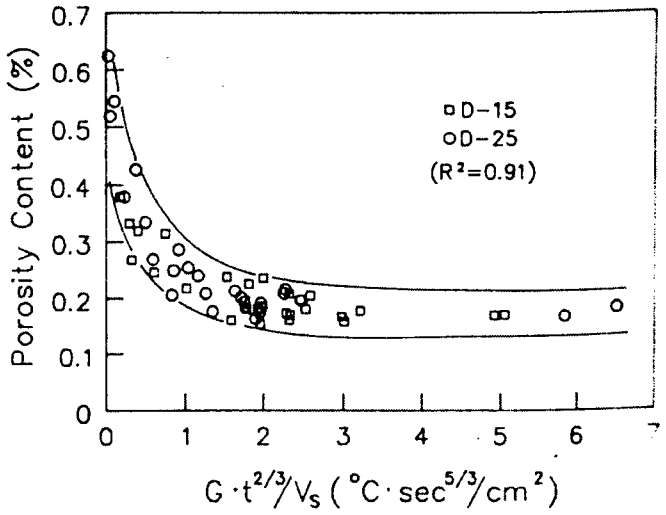

Figure 2-9 The correlation between porosity content and the feeding efficiency parameter (L.C.C.) from a study by Lee *et al.*[13]

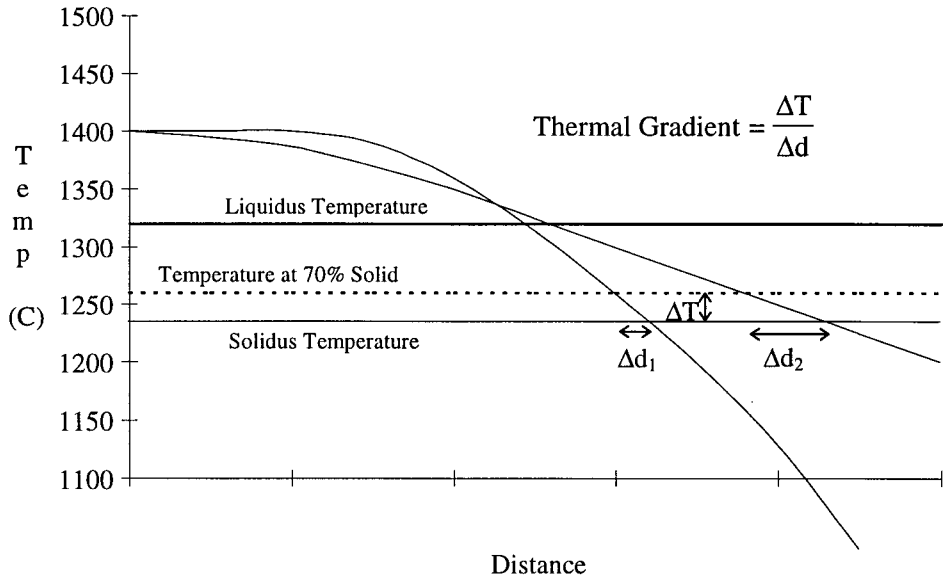

Figure 2-10 Schematic illustration showing the distance through which liquid metal must flow to the solidification front with a steep (Δd_1) and shallow (Δd_2) thermal gradients.

3. Scope and Objectives

3.1 Scope

Investment casting, like various other casting methods, can produce defects, such as microporosity, during processing that can inhibit component performance and/or even cause component rejection. In order to alleviate this problem, one would have to reconfigure the gates and risers of the system in order to yield a quality product. For many castings, this is a difficult task and may require several iterations by trial and error to obtain the desired results.

Rather than a trial and error approach through test castings, computers and commercial modeling software now have the capability to simulate the thermal history of complex castings with a reasonable degree of accuracy. Reconfiguration of the mould that was once made on the foundry floor, can now be made on a computer and simulated. Through this analysis software, the thermal history of a casting can then be examined and areas prone to porosity evolution can be calculated through criteria found in the literature.

Utilizing a commercial finite element package (ProCAST™), the present study will attempt to predict the thermal history and the distribution of porosity for a Stellite alloy investment casting that is prone to microporosity. The mould gates and risers will then be reconfigured and simulated through a computer workstation such that zero or very little porosity is predicted within the problematic areas of the casting.

3.2 Objectives

The objectives for the present study are as follows:

1. Develop and verify a mathematical model capable of predicting the evolution of temperature during solidification in an investment cast component using the commercial finite element code, ProCAST™.

2. Characterize the distribution of porosity in a component prone to porosity formation.

3. Verify the ability of various porosity criteria (Niyama and L.C.C.) to predict the porosity in (2).

4. To propose reconfigured moulds to reduce or eliminate porosity in the component in (2).

4. Experimental Methods

The experimental methods for this study involved measuring temperature in moulds instrumented with thermocouples as well as conducting an assessment of the distribution of porosity in an industrial casting prone to porosity formation. The thermocouple measurements were conducted at Deloro Stellite Inc. in Belleville, Ontario. The sample industrial casting was provided by Deloro Stellite Inc. and was analyzed for porosity using equipment and facilities in both Belleville and UBC

4.1 Experimental Castings

The experimental castings were made to quantify important boundary conditions and verify material property data obtained from a number of literature sources, including a previous study at UBC[20]. A cylinder, as shown in Figure 4-1, was adopted for the experiments so a computationally efficient axisymmetric analysis could be used. The mould was instrumented with thermocouples at various locations to record the change of temperature over time. Two separate experiments were completed. In the first experiment, the mould was heated in the preheat furnace and then allowed to air cool while recording temperature. This experiment quantified the mould/air interface heat transfer coefficient and validated the mould thermophysical properties without the added complication of molten metal. In the second experiment, temperatures were recorded in a mould subjected to standard casting practices, which included the solidification and subsequent cooling of molten metal. This experiment quantified the boundary conditions at the metal/mould interface and verified the thermophysical properties for the metal.

4.1.1 Experimental Methodology and Procedures

The cylindrical test mould, shown in Figure 4-1, was employed because of its large height-to-radius ratio. Thus, over a significant portion of the casting, there was no heat transfer in the axial direction and only a simple one-dimensional axisymmetric model was required.

The wax patterns and moulds were constructed by Deloro Stellite following normal production procedures[15,16]. The cylindrical test moulds were instrumented with 0.032" type K (Chromel-Alumel) thermocouples. These thermocouples were used primarily for their high operating temperatures and their availability within the department of Metals and Materials Engineering at UBC. They are recommended for oxidizing environments with a maximum service temperature of 1260 °C (2300 °F). The initial calibration tolerance for a type K thermocouple from ANSI MC96.1 is +/- 2.2 °C or +/- 0.75% (whichever is greater), and this is well within the tolerances for this study.

The thermocouple wire junctions were cleaned to ensure a good contact between the leads, and the bare wires were twisted one-and-a-half times around each other. A hand-held disc grinder was then used to cut a groove into the mould shell and the thermocouple junction was placed inside. The thermocouples were then cemented in place using Sairset[17], a mould repair ceramic. The bare wires were insulated using silica sheaths to protect the thermocouples from short circuiting.

The data acquisition system consisted of an Omega Engineering Inc. OM160 Portable Intelligent Data Logger. It was chosen for its portability and compatibility with

the Type K thermocouples. The data was acquired at a rate of 1 Hz, and was later downloaded onto a computer using the software and hardware provided by Omega. The preheat furnaces were fueled by natural gas using four pyronics #10NM-Ga burners located at the top of the furnace. The alloys were melted in either a 20 or 35 lb. "roll over" furnace using a ViP Trak 75 inductor which operated at a maximum power output of 75 kW. Argon gas was introduced through the top of the induction furnace to provide an inert shroud to avoid oxidation of the reactive alloy constituents. The test moulds were sectioned after they were cast to verify the thermocouple locations.

The cylindrical test moulds were heated in the preheat furnaces at 1040 °C (1900°F) for approximately two hours, and the Stellite alloys were melted in the induction furnace to a superheat of 1482 °C (2700 °F). The test mould was transferred from the preheat furnace and placed on a bed of sand.* The Stellite alloy in the induction furnace was transferred to the mould using a preheated (2700 °F) 30 lb. ladle. The transfer time was recorded (Table 4-1) and was defined as the point at which the mould was removed from the preheat furnace to the time at which the metal was poured.

---

* The 'normal' practice for investment casting is to place the investment mould upside-down on the roll-over induction furnace. The mould is then clamped into place and the contents of the furnace are poured into the mould by rolling over the entire furnace. Due to the presence of thermocouples on the investment mould, there was concern that rolling over the furnace may fracture the silica sheathing on the wire leads and short out the thermocouples. For this reason, the investment mould was placed in a bed of sand and the molten metal was transferred from the furnace to the mould via a preheated ceramic ladle.

4.2 Assessment of Porosity

To investigate the ability of ProCAST™ to predict the distribution of porosity in the investment casting process, a production casting prone to porosity formation was selected for analysis. The investment casting studied was a Stellite 3 diesel seat casting with the configuration shown in Figure 4-2. The casting was assembled with four seats per cluster and seven clusters per stand.

The valve seal moulds were poured using normal roll over furnace pouring practice[18]. These moulds were allowed to soak in the preheat furnaces for two hours at 1040 °C (1900 °F), and the Stellite alloy was melted and superheated to a temperature of 1482 °C (2700 °F). The mould was removed from the preheat furnace, placed upside down on the roll-over furnace and secured. The entire furnace and mould was "rolled" over and the contents of the furnace poured into the mould. The mould was then removed from the furnace and allowed to air cool.

After casting, the diesel seat was sectioned and polished to view the microstructure and assess the extent to which porosity had formed. A Bueller Cutting Machine using a SiC disc was used to section the Stellite castings. Several diesel valve seats from the middle of the investment stand were sectioned, mounted in an epoxy resin, and polished using SiC polishing wheels with grit size ranging from 50 to 600μm. The final polish was done on a cloth lap using a 5 μm and a 1 μm diamond slurry.

4.2.1 X-ray Analysis of Porosity

Each diesel seat casting was X-rayed using the facilities at Deloro Stellite Inc. to examine and quantify the extent of porosity in the component. The X-ray photos were directed through the thickness of the ring casting with the component in plan view, as shown in Figure 4-3. Thus the view only represents a two dimensional distribution of the porosity in the circumferential direction. Using this techniques, the positions of the porosity through the thickness of the casting could not be assessed. Unfortunately, it was very difficult to produce a positive photo due to the quality of the X-ray negatives. Instead, the X-ray negatives were viewed under a bright light, and the extent of porosity was tabulated based on observation.[†]

A schematic diagram of the variables measured to quantify the distribution of the porosity from the X-ray results is shown in Figure 4-3. The arc length (measured in degrees) and the average approximate radial depth (d) of the porosity was recorded for the ring casting and presented in Table 4-2. In Figure 4-3, the porosity is distributed over approximately half the circumference of the seal along the inner half radius and is located on the side of the seal opposite to the in-gate. A detailed examination of the porosity is presented in the following section.

[†] Porosity on an X-ray negative is defined as a localized darker region contrasting the porosity free, lighter areas of the casting.

4.2.2 Microstructural Assessment of the Porosity

The diesel valve seat was sectioned into several parts to validate the results obtained from X-ray analysis. A macrophotograph showing the distribution of porosity across a transverse section through the mid-plane of the casting is illustrated in Figure 4-4. In this figure, the porosity encompasses approximately half of the casting to approximately the half radius, similar to the X-ray results found in Figure 4-3. However, there are some differences between the two figures due to the fact that the X-ray results show the cumulative effect of the porosity on the transmission of the X-rays through the thickness of the seal. In contrast, the results from the metallographic examination only show the results for a specific plane.

Upon closer inspection, the microporosity is comprised of a network of pores (Figure 4-5) that are clustered along lines directed toward the inside of the casting. A sample of the casting at a higher magnification (Figure 4-6) shows that the pores are found within the interdendritic region of the microstructure and thus are at the scale of the dendrite spacing. The scale together with the orientation of the network of pores suggests that the microporosity formed as a result of poor feeding through the dendritic array. However, based on these photomicrographs, there is no evidence that indicates the exact cause for porosity formation (i.e. gas evolution, shrinkage, or a combination of both). This particular alloy is comprised of extremely reactive constituents (for example chromium) that "tie" up any dissolved oxygen in the molten bath. Very low concentrations of dissolved oxygen results, and this restricts the dissolution of oxygen

during solidification. With the absence of dissolved oxygen, the porosity forms as a result of poor feeding during the solidification process.

In an attempt to quantify the porosity in the casting, a section of the valve seal, shown in Figure 4-5, was examined using image analysis. From the microstructure in Figure 4-5, twenty-two sample frames[‡] were taken; eleven were adjacent to the inner diameter and eleven were 2 mm away from the inner diameter. The dark areas on the polished surface (representing porosity) were counted and their percent areas were calculated based on the total area of each frame. A histogram of the twenty two fields is shown in Figure 4-7. The first eleven fields, representing the region adjacent to the inner diameter, shows a relatively high area fraction of porosity, ranging from approximately 1.5% to 13%. This range implies that the porosity is not homogeneous but rather has localized regions or clusters of pores. Moving 2 mm away from the inner diameter, the sample fields in the histogram, from 12 to 22, have a different appearance than the values closer to the inner diameter. The values found in this part of the histogram are, on average, much smaller.

[‡] The area per frame =1.54x2.044 mm^2

Table 4-1 Transfer time from the preheat furnace to the pouring of molten metal.

Experiment Designation	Transfer Time (sec.)
MP1 (Metal Pour 1)	100 sec.
MP2 (Metal Pour 2)	105 sec.
Investment Cast Diesel Valves, Four Seals per Cluster	22 sec.
Investment Cast Diesel Valves, One Seal per Cluster	22 sec.

Table 4-2 The distribution of porosity in the ring casting measured as arc length and depth relative to the inner metal surface. Refer to Figure 4-3 for an illustrative description.

Arc Length (degrees)	Maximum depth (d) of porosity relative to the inner seal casting surface. (mm)
204°	5.6
184°	5.7
188°	5.5
186 ° (average)	5.6 (average)

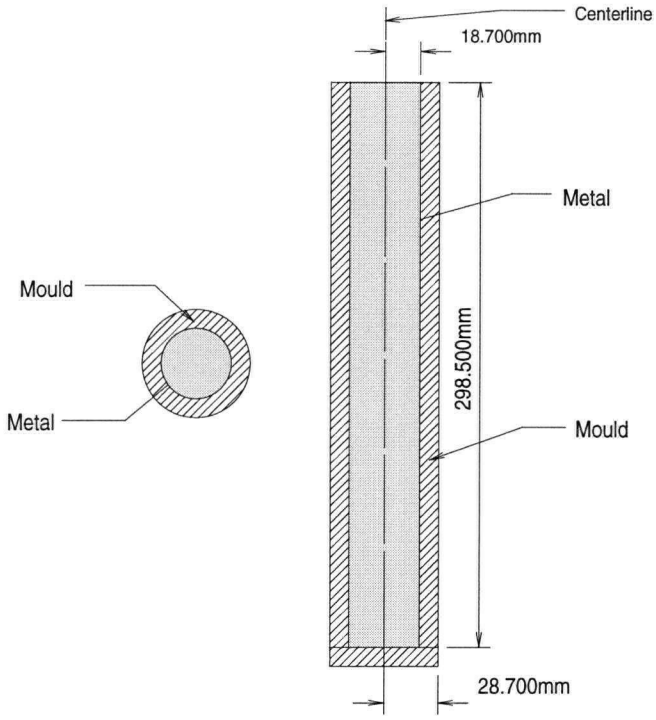

Figure 4-1 A 2-d diagram showing the mould configuration used to validate the metal and mould (shaded) physical properties and the heat transfer boundary conditions in ProCAST™

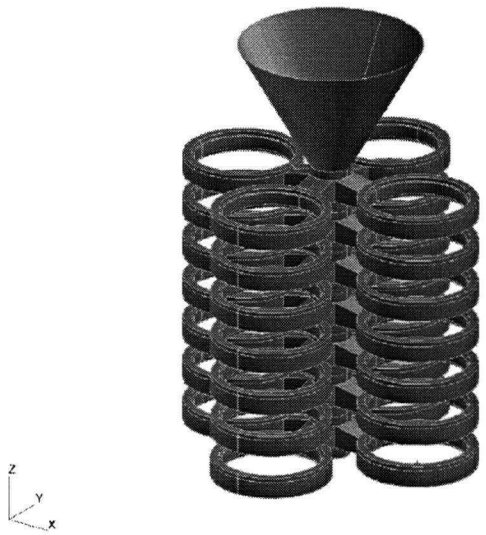

Figure 4-2 A schematic showing the wax pattern configuration for the Stellite 3, Diesel Valve Seats used for the validation of porosity prediction,

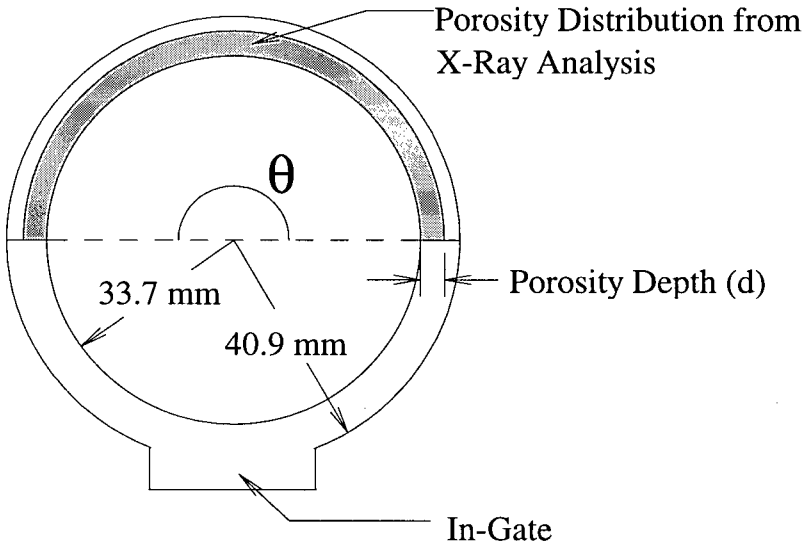

Figure 4-3 Schematic Diagram showing the Distribution of Porosity (shaded area) in the Diesel Valve Seal.

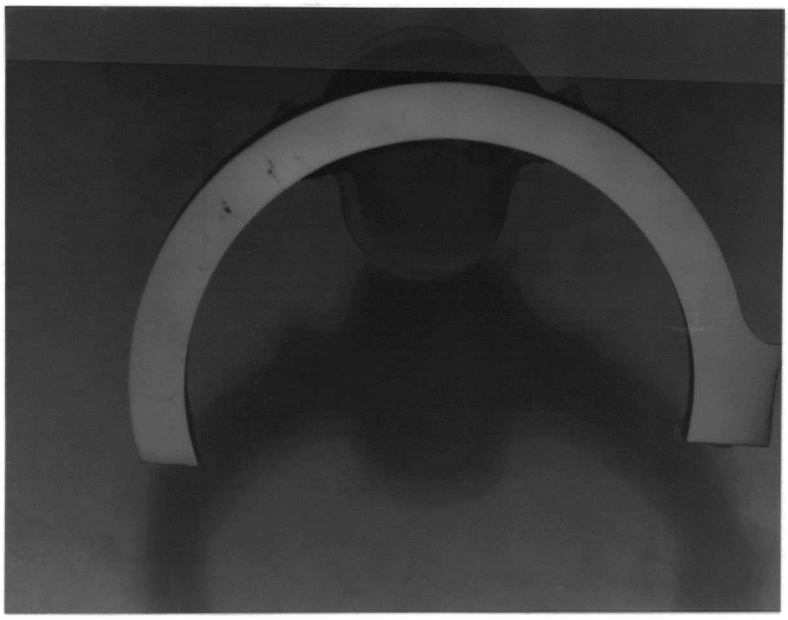

Figure 4-4 A macro-photograph showing a transverse cut plane through the approximate center of the diesel valve seals showing the extent and distribution of porosity. (unetched)

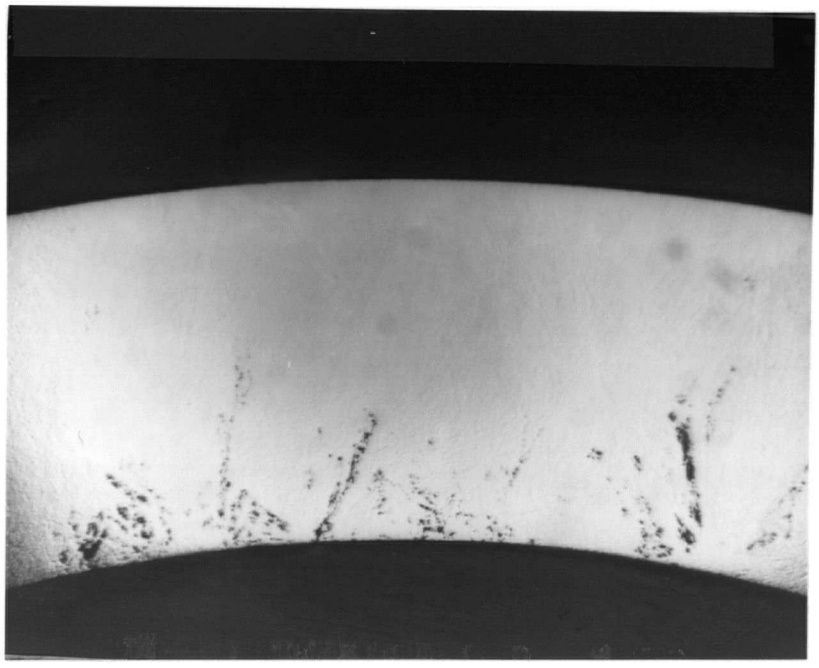

Figure 4-5 A microphotograph of a transverse section through the approximate center of the diesel valve seal across from the ingate showing the depth and distribution of the microporosity from Figure 4-4. (unetched, mag. 6.4x)

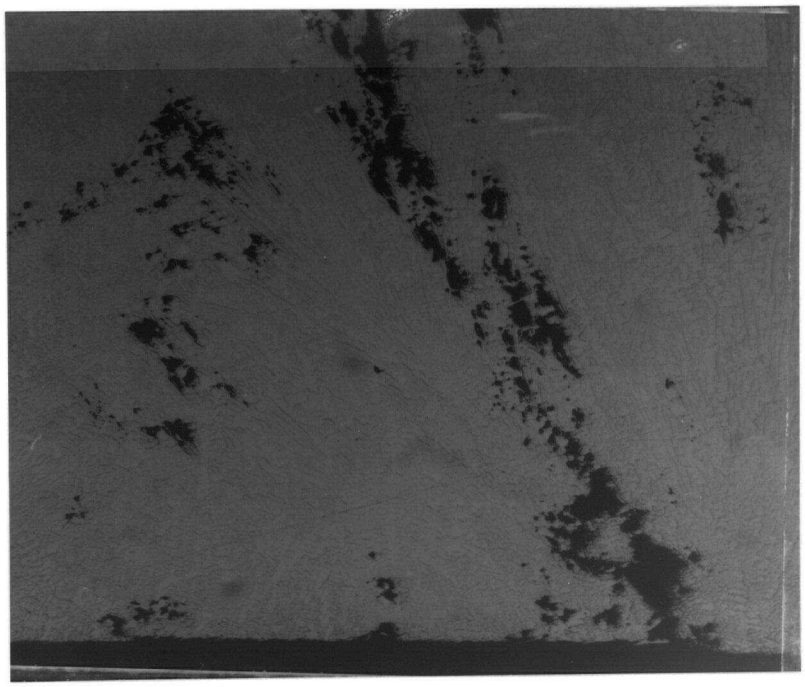

Figure 4-6 A close-up of the porosity from Figure 4-5 showing the size and depth of porosity in the diesel valve. (unetched, mag. 50x)

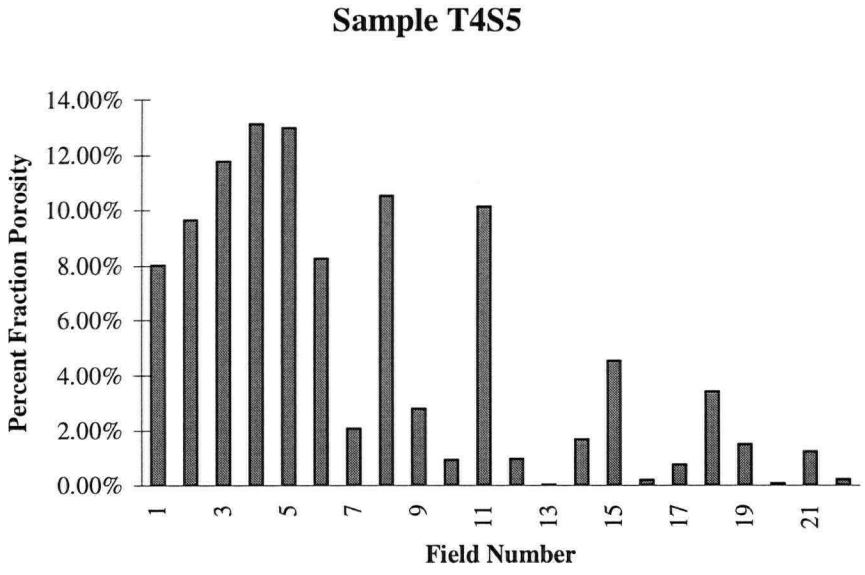

Figure 4-7 A histogram representing the percentage of porosity from the microstructure in Figure 4-5.

5. Mathematical Model Formulation

ProCAST™ provides the computational engine and framework necessary to conduct the heat flow analysis required to predict the evolution of temperature in the investment casting process. Below in the following sections, the formulation of the basic heat flow equations and the model construction are discussed.

5.1 Mathematical Formulation

In a casting process, heat flows by diffusion through the metal and mould (in the absence of fluid flow of the molten metal) and is removed from the mould surface by natural convection and radiation. The flow of heat is transient, i.e. the temperatures in the casting and mould vary with time. The governing partial differential equation describing the flow of heat is as follows:

$$\rho\frac{\delta H}{\delta t}-\nabla[k\nabla T]=0 \qquad \text{eqn. 5-1}$$

where $\nabla=\frac{\partial}{\partial x}+\frac{\partial}{\partial y}+\frac{\partial}{\partial z}$, k is the thermal conductivity, ρ is the density and H is the enthalpy. The enthalpy term (H) encompasses both the specific heat term (Cp), and the evolution of latent heat during solidification as shown in eqn. 5-2

$$H(T)=\int_0^T C_p dT+L[1-f_s(T)] \qquad \text{eqn. 5-2}$$

Within ProCAST™, the set of conditions described above are solved using the finite element method (FEM), which is a general purpose numerical method for solving equations of the type presented in eqn. 5-1. To account for the effect of re-radiation that can occur between adjacent sections of the same casting or casting assembly, ProCAST™ contains a "ray tracing" utility which calculates the necessary view factors. The details of this technique and its applications are available in the ProCAST™ User's Manual[19].

5.2 Mathematical Model Development

The information needed for ProCAST™ to develop the model is: the geometry of the problem as defined by the finite element mesh, the relevant material property data, and the relevant boundary and initial conditions. The material property data was found from various literature sources and the initial conditions were measured for a casting cycle. The relevant boundary conditions were determined by comparing model predictions to measured thermocouple data. These conditions are discussed in greater detail in the following sections.

5.2.1 Building the Finite Element Mesh

In the past, mesh generation for finite element analysis was done by hand and was a tedious and time consuming process. The geometry in this study was not too complex,

but it was difficult enough to warrant the use of a commercial code called Patran V5 (a CADD package, FE mesh generation and FEM software[§]).

The initial step in developing the finite element mesh was to input the geometry in the form of a "solid model". Mesh seeds, which define the mesh size, were applied to the boundaries and edges of the casting and the mould surfaces. A triagonal surface mesh was generated based on the mesh seeds and the nodes and elements were exported to a neutral file. This file was imported into a tetrahedral mesher called MeshCAST which computed the solid tetrahedral mesh for the casting and mould. Although not explained in the ProCAST manuals[19], the mesher referenced the boundaries at the mould/metal interfaces in the solid mesh for future use in the FEM preprocess module, PreCAST. This process was quite cumbersome, and depending on the complexity of the geometry, can be one of the most time consuming steps in the model development.

5.3 Pre-Process FEM in PreCAST

ProCAST™ uses a pre-process module called PreCAST to apply such FEM parameters as material properties, initial and boundary conditions. This operation was straightforward and is not be discussed in detail. Further information on this subject can be found in the ProCAST reference manual.[19]

[§] This software package was only used for its CADD and surface mesh generation capabilities.

5.4 Post-Process Mathematical Formulations in PostCAST

Once fully developed and submitted to the computation engine or solver, the results were processed in a separate module called PostCAST. Within this module, the thermal history of the casting and mould can be examined and the parameters (or a combination there of) such as the thermal gradient, solidification rate, and isotherm velocities could be calculated. These three sets of calculations formed the foundation for the various porosity criteria formulations.

For example, the thermal gradient expressed in eqn. 5-3a, was calculated at particular nodal temperatures. The software cycled through the thermal history and whenever a nodal temperature reached a predetermined temperature, the thermal gradient (G) was calculated at that point. The results were then viewed graphically in the form of contour plots. For the two dimensional analysis, the models were constructed in the x-y plane and eqn. 5-3a reduced to eqn. 5-3b.

$$G = \left[\left(\frac{\partial T}{\partial x} \right)^2 + \left(\frac{\partial T}{\partial y} \right)^2 + \left(\frac{\partial T}{\partial z} \right)^2 \right]^{1/2} \qquad \text{eqn. 5-3a}$$

$$G = \left[\left(\frac{\partial T}{\partial x} \right)^2 + \left(\frac{\partial T}{\partial y} \right)^2 \right]^{1/2} \qquad \text{eqn. 5-3b}$$

The rate of cooling during solidification was defined as the time taken for a particular node to cool from the liquidus to solidus temperature as shown in eqn. 5-4.

$$L = \left[\frac{T_{liquidus} - T_{solidius}}{t_{liquidus} - t_{solidius}} \right] \qquad \text{eqn. 5-4}$$

The solidification velocity was more difficult to calculate but straightforward to apply in the post process operations. The ProCAST™ User Manual described the solidification velocity as:

> "When each node reaches a specified temperature (solidus), a point is located along the temperature gradient some distance away and the time that it takes for the isotherm to reach that point is determined. R (solidification velocity) is then calculated as that distance divided by the difference in time."[19]

6. Sensitivity Analysis and Model Validation

6.1 Sensitivity Analysis

An extensive sensitivity analysis was conducted by Dominik[20] on a cylindrical component vacuum investment casting at Deloro Stellite. Dominik assessed the influence of boundary conditions and material properties on the prediction of a finite element thermal model. Owing to similar aspects of the present study, a number of the results from her investigation were applied to the present work.. The parameters that warranted a re-examination were those pertaining to the boundary conditions that distinguish air investment casting (examined in the present study) from vacuum investment casting (examined in the previous study[20]). In addition, differences in the alloy systems studied necessitated a re-examination of the model's sensitivity to those parameters specific to the alloy.

6.1.1 Metal/Mould Interface Heat Transfer Coefficient

The interface heat transfer coefficient between the metal and the mould is difficult to quantify. When the molten metal is initially poured into the mould, there is intimate contact at the mould/metal interface, and the heat transfer coefficient is extremely high. However, at the onset of solidification, the metal contracts and pulls away from the mould surface which creates a gap and a barrier for heat flow as illustrated in Figure 6-1. In Dominik's study[20], the gap occurred in a vacuum environment and the only mode of heat transfer from the metal to the mould was by radiation and by conduction at contact points. In this study, casting occurred in atmospheric pressures and any gap that formed

contained air. Thus, the heat transfer from the metal to the mould occurred by radiation (at the higher temperatures), by conduction/convection through the air gap, and by conduction across contact points between the metal and the mould.

Dominik[20] showed that the initial heat transfer coefficient between the metal and the mould had negligible effects on the solidification time but did influence the mould temperature profiles. Two model runs were performed on a simple one-dimensional, axi-symmetric system (Figure 6-11) to establish the sensitivity of the mould thermal profile and the time for complete solidification to the heat transfer coefficient. The base value for the heat transfer coefficient was 2500 $W/m^2/°C$ and was adjusted to 1250 and 5000 $W/m^2/°C$. The results are tabulated in Table 6-2 and presented graphically in Figure 6-2 and Figure 6-3 respectively. These figures show that changing the metal/mould heat transfer coefficient had very little effect on the solidification time for the metal but it did affect the thermal profiles through the mould thickness. Due to its uncertainty, this parameter was one of the casting variables that was adjusted in the model to fit the thermocouple data.

In complex investment moulds, gap formation at the mould/metal interface does not occur uniformly throughout the casting. Depending on the configuration, metal contraction and/or distortion can either increase the size of a gap, or maintain intimate contact at the metal/mould interface. This phenomena is best explained schematically in Figure 6-4. Due to non-uniform cooling and component configuration, metal/mould contact may remain at points, even after complete solidification. Consequently these contact areas will see higher metal/mould heat transfer coefficients than areas where a

gap formed. The work by Dominik[20], showed that varying the mould/metal contact time had a minor influence on the solidification time of the metal, and a large influence on the thermal profile through the casting wall. Hence, the contact time was taken into consideration when the mould/metal heat transfer coefficient was applied for boundary condition verification.

6.1.2 Mould Conductivity

The mould conductivity was another investment casting variable that was not documented very well in the literature. The investment ceramic mould is an inhomogeneous structure which consists of layers of different densities of stucco or flour (a binder type compound) together with gas porosity. Therefore, it may be anticipated that heat was transported in the mould by diffusion and radiation, thus an effective conductivity term was difficult to quantify. Consequently, mould conductivity must be determined by comparing model predictions with thermocouple measurements.

The work by Dominik[20] showed that the ceramic mould thermal conductivity had a significant role on the solidification time of the metal and the thermal profile through the mould thickness. The results for this study are presented in Figure 6-5 and tabulated in Table 6-2. Increasing the thermal conductivity from 1.0 W/m/K (base value) to 1.2 W/m/K, decreased the solidification time by 5% and changed the thermal profile through the thickness of the mould shell. Due to its uncertainty, mould conductivity was adjusted to fit the thermocouple data.

6.1.3 Mould/Air Interfacial Heat Transfer Coefficient

The effect of changing the mould/air interfacial heat transfer coefficient from a base value of 20 $W/m^2/°C$ to 30 $W/m^2/°C$ is presented graphically in Figure 6-8 and tabulated in Table 6-2. Increasing this parameter by 50 % decreased the solidification time by an insignificant 8%. However, Figure 6-8 shows that the mould thermal profiles were affected by this coefficient. Due to the uncertainty of the air/mould heat transfer coefficient, this parameter was one of those adjusted to fit the experimental thermocouple data.

6.1.4 Metal Initial Temperature

At Deloro Stellite Inc., the initial temperature of the metal was well controlled. Although this had some effect on the mould thermal profiles (Figure 6-6) and solidification time (Table 6-2), the initial temperature was not adjusted from the measured value to fit the thermocouple data.

6.1.5 Mould Preheat Temperature

At Deloro Stellite Inc., the preheat temperature of the mould was also well controlled. Although this had some effect on the mould thermal profiles (Figure 6-7) and solidification time (Table 6-2), the mould preheat temperature was not adjusted from the measured value to fit the thermocouple data.

6.1.6 Stellite 3 Material Properties

The material properties for Stellite Grade 3 were taken for similar alloy grades from handbooks[21,22,23,24] and an additional document[25]. Due to the good characterization of these values (heat capacitance, conductivity, latent heat evolution, and liquidus/solidus values), they were not adjusted to fit the experimental thermocouple data.

6.2 Discussion of Results

As previously discussed, two sets of test moulds were utilized to quantify the heat transfer coefficient at the mould/air and the metal/mould interface and to validate the thermophysical properties used in the model. Thermocouple measurements were taken without and with liquid metal present.

6.2.1 Validation of Mould Shell Properties and Heat Transfer Coefficient Between the Mould and the Air (No Liquid Metal Present)

Two thermocouples were inserted into the wall of the cylindrical test mould (Figure 4-1) approximately 3 and 9 mm beneath the outer surface. The investment mould was placed in a preheat furnace and allowed to soak at 1040 °C for approximately two hours. The mould was then removed from the furnace and allowed to air cool while the temperature was recorded with time.

A one-dimensional, axi-symmetric computer model was constructed (Figure 6-9) to simulate air-cooling of the investment mould. The heat flux of the inner surface of the mould was assumed to be zero. This is a valid assumption as the interior of the mould

only contains heated air with a heat capacity of approximately 240 $J/m^3/K$; three orders of magnitude less than the mould material. The heat transfer coefficient between the outside of the mould and the air was then calculated by trial and error and by the results from the sensitivity analysis. The physical properties of the mould were obtained from a previous study[20] and re-evaluated for the present study. The results from the model run, using the mould physical properties presented in Table 6-4, are shown in Figure 6-10.

Figure 6-10 shows the boundary conditions presented in Table 6-5 and the physical properties of Stellite 3 presented in Table 6-6 predict results that agree with the thermocouple values. These results confirm that the parameters utilized in the model were suitable.

6.2.2 Validation of the Stellite 3 Properties and the Heat Transfer Coefficient Between the Mould and the Metal (Liquid Metal Present)

Two castings were poured to determine the heat transfer coefficient between the mould and metal and validate the physical properties of Stellite 3. Thermocouples were inserted into the test mould of Figure 4-1 at varying depths (Table 6-3), preheated to a known temperature, and the molten metal was poured.

The finite element model in Figure 6-10 was constructed and run. This model configuration was selected to evaluate the boundary conditions between the metal and mould because of its minimal computational requirements. The boundary conditions were adjusted by trial and error to fit the thermocouple data, so a small model was required to produce a fast turn around of the results.

After several iterations, a good model/thermocouple convergence was achieved. The results for the two solidification experiments and the thermal model are presented in Figure 6-12 and Figure 6-13. These figures show that the thermocouples located on the outside of the mould display an initial cooling trend, caused by heat loss from the outside of the mould during transfer from the preheat furnace. However, the thermocouple 0.65 cm from the outer mould surface in Figure 6-12, did not exhibit this cooling trend and this was probably due to poor thermal conductivity of the mould. The temperature increased dramatically with the introduction of molten metal. A decrease in the cooling rate occurred after a short time because of the release of latent heat from the solidifying metal. Once the metal was solid, the metal and the mould continued to cool to room temperature.

Both figures show very good agreement between the thermocouple results and the output from the thermal model simulation. The heat transfer coefficient in Figure 6-14 accounted for heat transfer by radiation and conduction as well as the effect of gap formation between the metal and mould during solidification. Figure 6-14 illustrates that the initial heat transfer coefficient between the metal and the mould was very high due to intimate contact between the molten metal and the mould interior wall. At the onset of solidification, the solidifying metal contracted away from the mould wall and resulted in an air gap. This air gap increased the resistance for heat transfer from the metal to the mould and the heat transfer coefficient decreased significantly.

The heat capacitance and conductivity terms are shown in Figure 6-15 and Figure 6-16, respectively. The thermal conductivity measurements for Stellite 3 were only

available for room temperature[24]. However, due to variations of thermal conductivity with temperature, the data for a similar Cobalt alloy, material designation WI-52[21], was adopted for Stellite Grade 3 and is presented in Figure 6-16. Similarly, the heat capacitance data in Figure 6-15 was compiled from a study on Stellite 21[22].

6.3 Summary

A sensitivity analysis was completed and showed the influence of casting parameters on the solidification time for the metal and on the thermal profiles through the mould. Based on these results, all the casting parameters had a varying degree of effect on the mould thermal profile during cooling. However, the solidification time for the molten metal was only affected appreciably by the mould thermal conductivity, metal superheat and to a lesser extent, the mould/air heat transfer coefficient.

Based on the results from the sensitivity analysis, the boundary conditions for the finite element model were calculated by trial and error from experimental thermocouple results from a simple cylindrical casting. This procedure also validated the assumed thermophysical properties for the mould and metal. The casting parameters obtained were then applied to more complex castings in the following sections.

Table 6-1 Sensitivity Analysis Parameters

Parameter	Base Value	Changed Property
Mould Conductivity (k, W/m/°C)	1.0	1.2
Mould Initial Temp. (°C)	982 °C	1037 °C
Air/Mould Heat Transfer Coeff. (h, W/m/°C)	20	30
Metal/Mould Heat Transfer Coeff. (h, W/m/°C)	2500	1250/5000
Metal Super Heat (°C)	1482 °C	1535 °C

Table 6-2 Sensitivity Analysis Results

Parameter	% Change of Parameter	Solidification Time (sec.)	% Change of Solidification Time	Reference Chart
Base	-	524.3	-	-
Mould Conductivity (k, W/m/°C)	20 %	498.3	-5 %	Figure 6-5
Mould Initial Temp. (°C)	2.2 %	515.3	-1.7 %	Figure 6-7
Air/Mould Heat Transfer Coeff. (h, W/m/°C)	50 %	482.2	-8.0 %	Figure 6-8
Metal/Mould Heat Transfer Coeff. (h, W/m/°C)	50 %	542.5	3.5 %	Figure 6-2
Metal/Mould Heat Transfer Coeff. (h, W/m/°C)	100 %	516.5	-1.5%	Figure 6-3
Metal Super Heat (°C)	3 %	597.6	14.0 %	Figure 6-6

Table 6-3 Measured thermocouple depth relative to the outside of the cylindrical casting.

Air Cool Experiment	Thermocouple Depth (cm)
Tm #1AC	0.9 cm
Tm #2AC	0.35 cm
Metal Pour Experiment #1 (MP1)	
Tm #1MP1	0.1 cm
Tm #2MP1**	0.2 cm
Tm #3MP1	0.65 cm
Metal Pour Experiment #2 (MP2)	
Tm #1MP2	0.3 cm

Table 6-4 Physical Properties of the Investment Mould[20]

Heat Capacitance Cp	$1.5 \cdot 10^3$ J/kg/K
Density ρ	$1.6 \cdot 10^3$ kg/m^3
α (ρ·Cp)	$2.4 \cdot 10^6$ J/m^3/K
Conductivity k	1.0 W/m/K

Table 6-5 Boundary Conditions Between the Mould and the Air

Ambient Air Temperature T_{amb} (°C)	30 °C
Heat Transfer Coefficient Between the Mould and Air (W/m^2/K)	20 W/m^2/K
Mould Emissivity	0.6

** A crack occurred at this thermocouple position producing a gap between the mould and the thermocouple junction. The data obtained from this thermocouple produced erroneous results and thus was disregarded.

Table 6-6 Physical Properties of Stellite Grade 3

Specific Heat (J/K/kg)	Figure 6-15
Conductivity (W/m/K)	Figure 6-16
Density	8.38 g/cm^3
Solidus Temperature (°C) [24]	1235 °C
Liquidus Temperature (°C) [24]	1320 °C
Latent Heat of Evolution (KJ/kg) [25]	245 kJ/kg

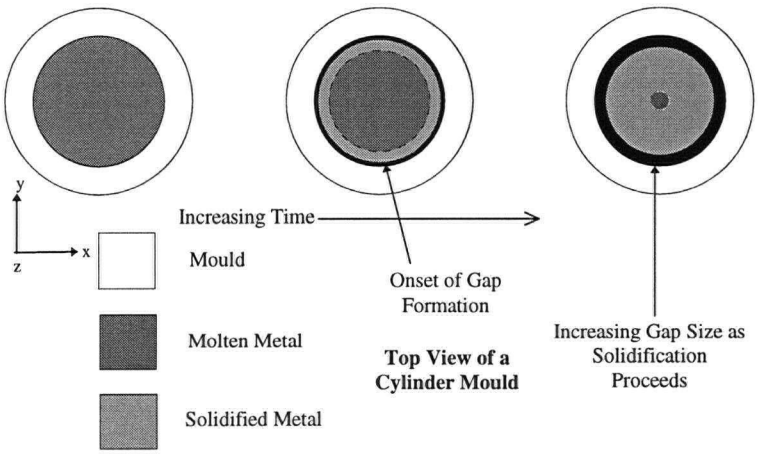

Figure 6-1 A graphical representation of gap formation at the mould/metal interface at the onset of solidification for a simple cylindrical mould configuration.

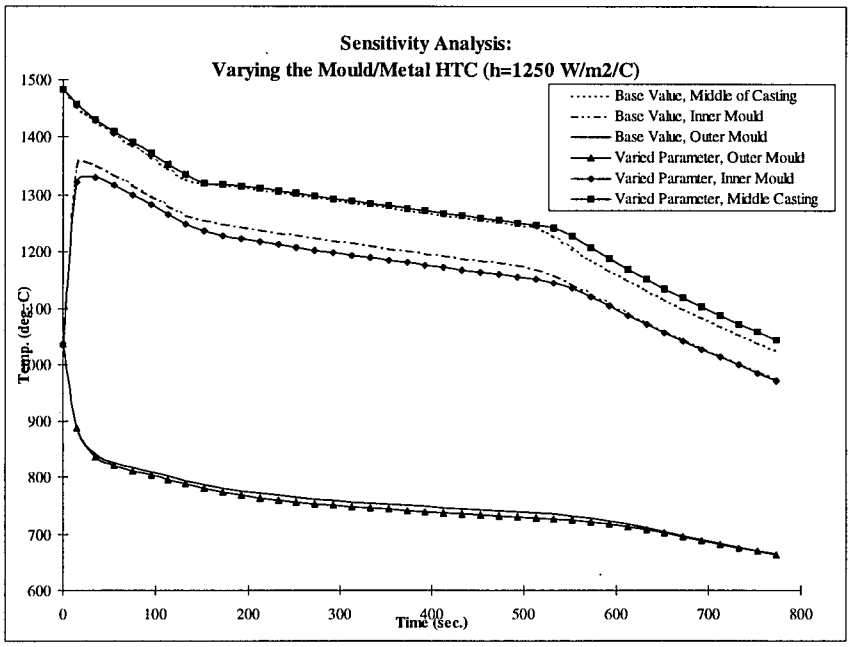

Figure 6-2 Varying the Mould/Metal Heat Transfer Coefficient Parameter from a base value of 2500 W/m^2/°C to 1250 W/m^2/°C.

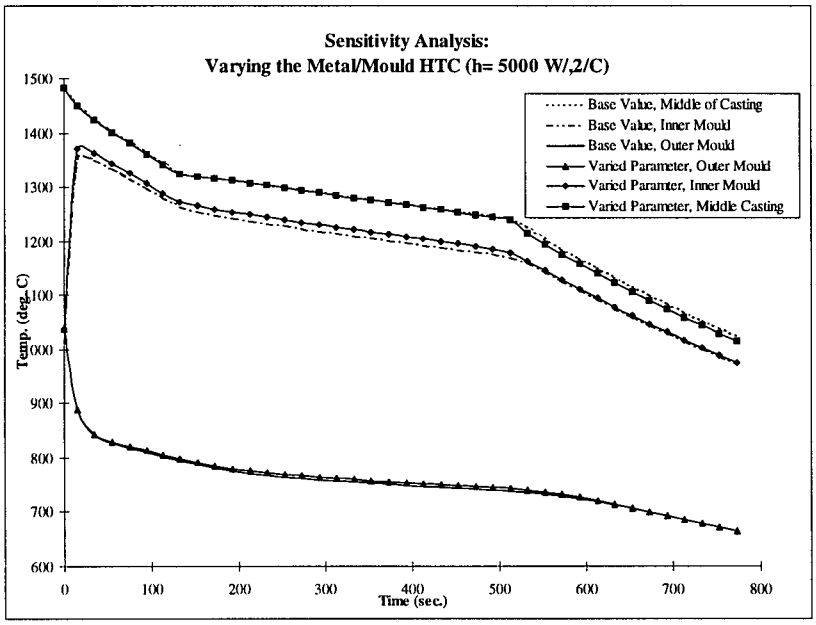

Figure 6-3 Varying the Mould/Metal Heat Transfer Coefficient Parameter from a base value of 2500 W/m^2/°C to 5000 W/m^2/°C.

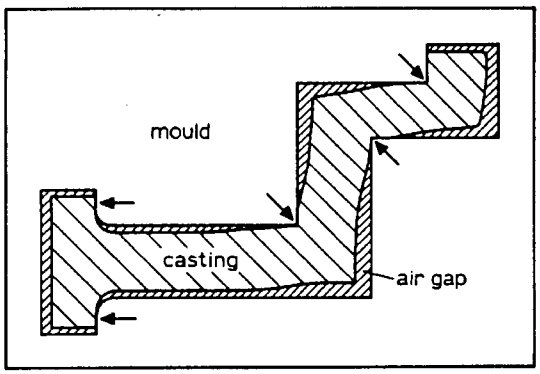

Figure 6-4 A schematic diagram showing the inhomogeneous gap formation in a simple two dimensional model.

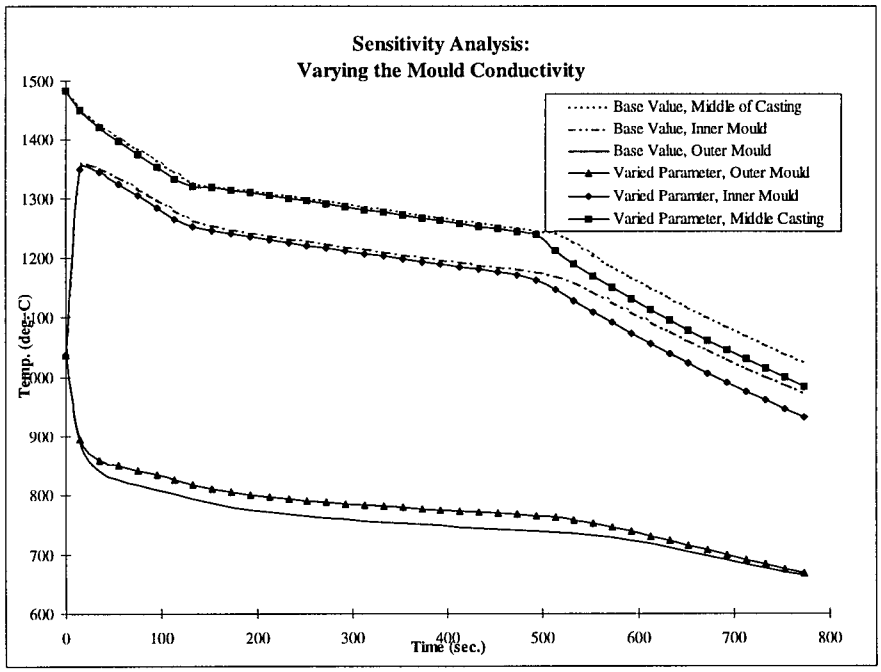

Figure 6-5 Model results by varying the Mould Conductivity from the base value of 1.0 W/m/K to 1.2 W/m/K.

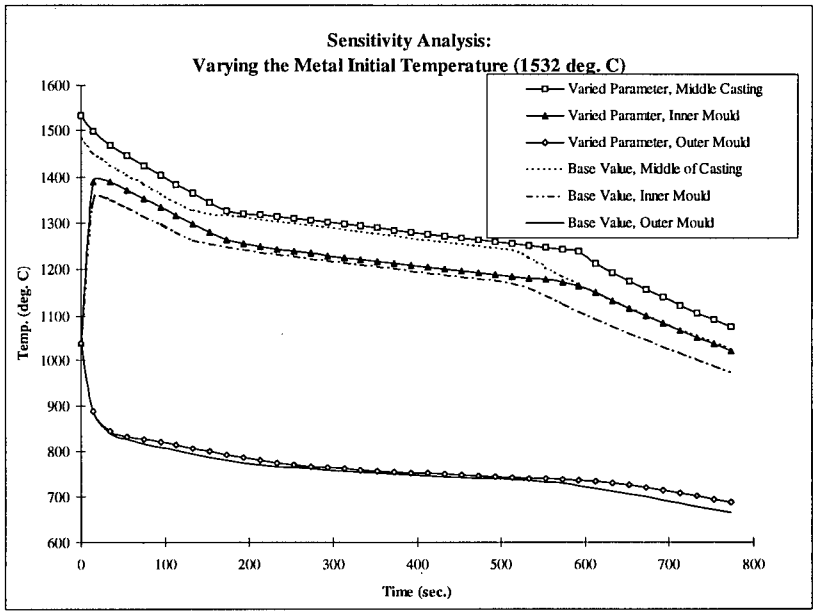

Figure 6-6 Model results by varying the Metal Initial Temperature from the base value of 1482 °C (2700 °F) to 1532 °C (2790 °F).

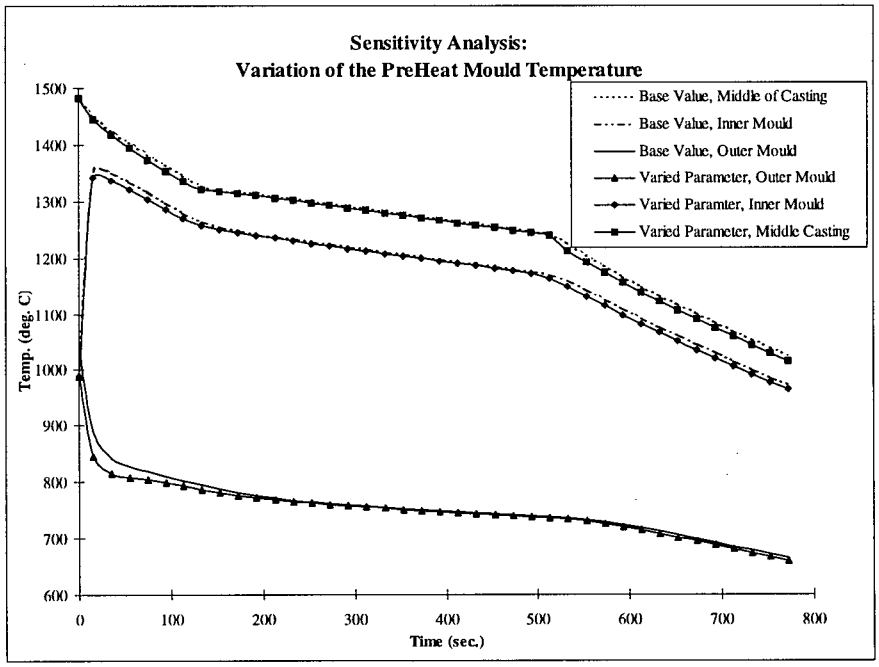

Figure 6-7 Model results by varying the mould preheat temperature from a base value of 1037 ° C (1900 °F) to 987 °C (1810 °F).

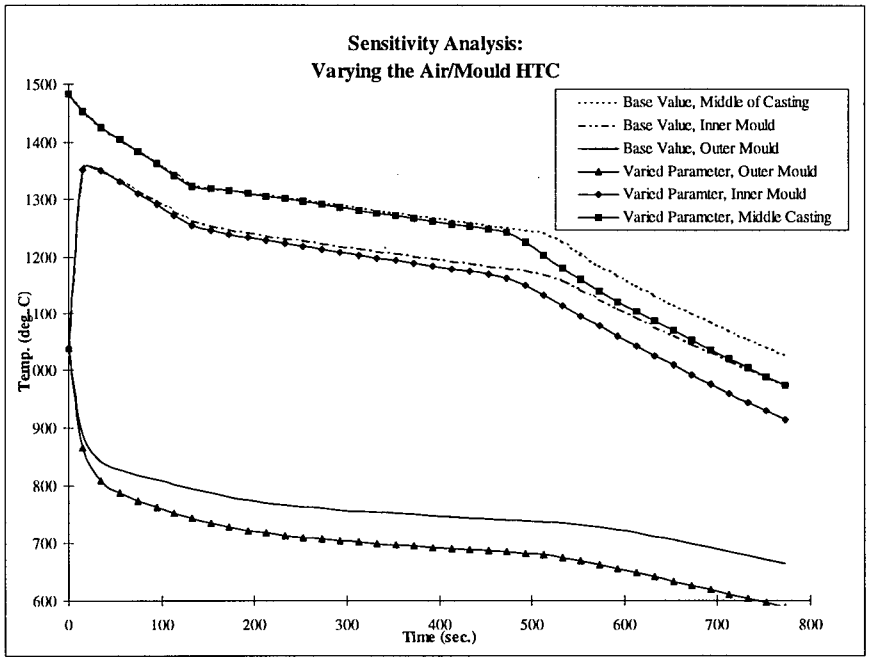

Figure 6-8 Model results by varying the air/mould heat transfer coefficient from a base value of 20 $W/m^2/°C$ to 40 $W/m^2/°C$.

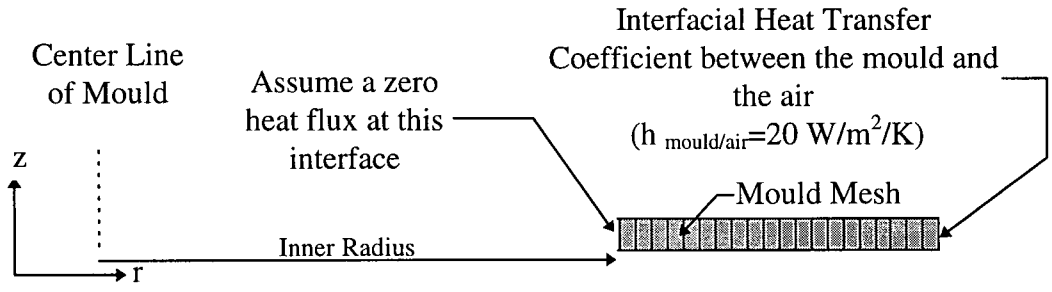

Figure 6-9 The one-dimensional axis symmetric computer model configuration used to simulate the cylindrical test mould air cool experiment.

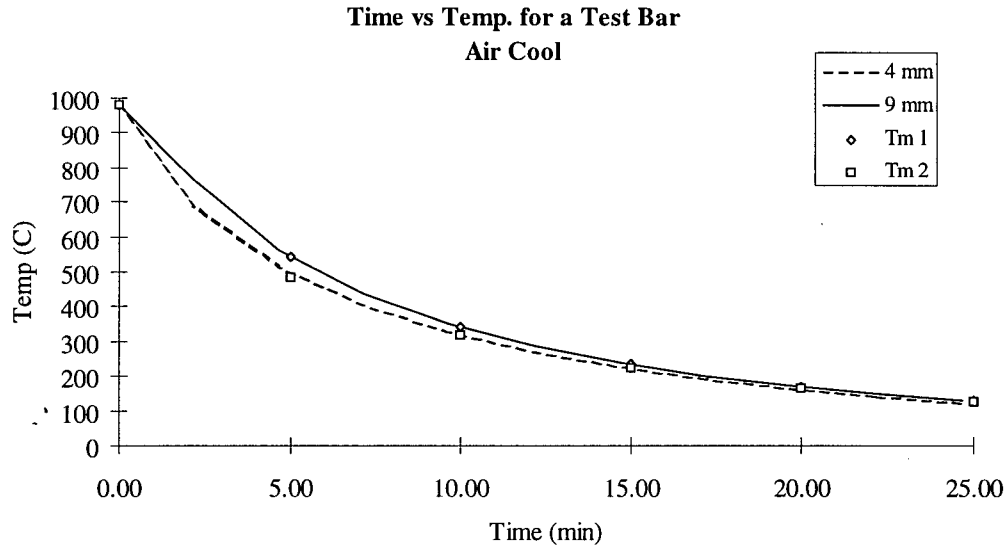

Figure 6-10 Validation of the mould physical properties and the heat transfer coefficient between the mould and the air against thermocouple data.

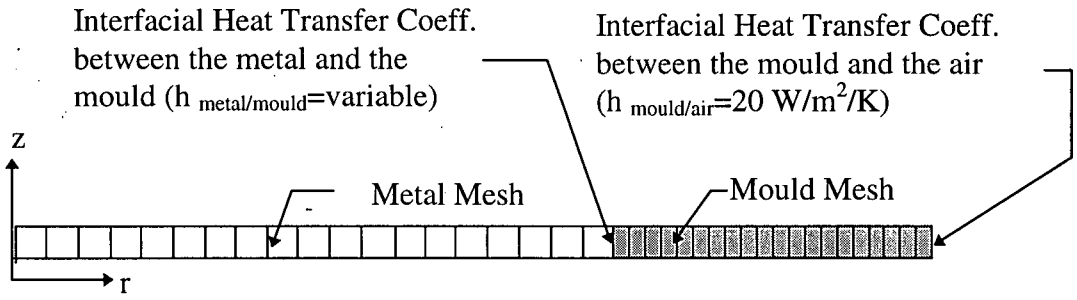

Figure 6-11 One-dimensional axis symmetric computer model configuration used to simulate the cylindrical test mould solidification experiment

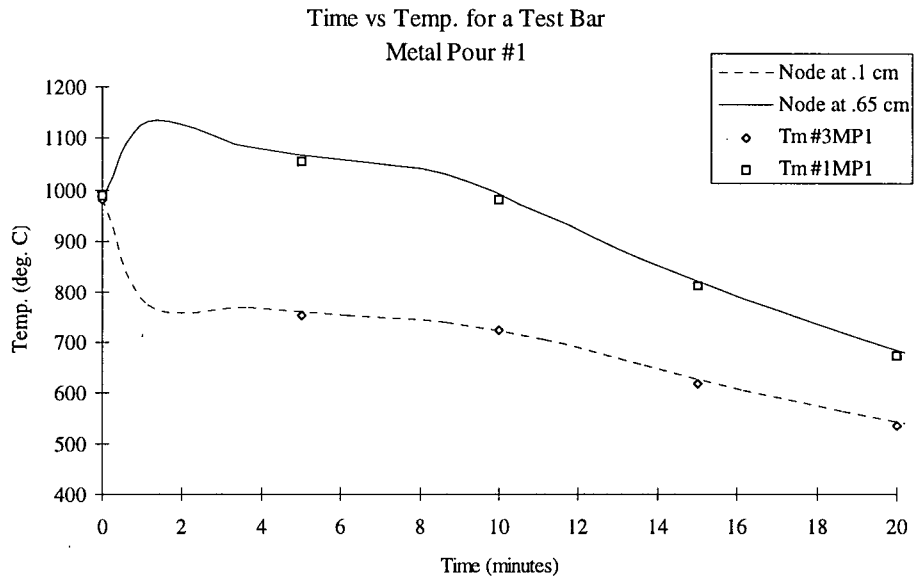

Figure 6-12 Thermocouple and thermal simulation (#1) results for the test cylindrical mould, mould preheat=1800 °F, metal temperature=2700 °F, refer to Table 6-3 for thermocouple position.

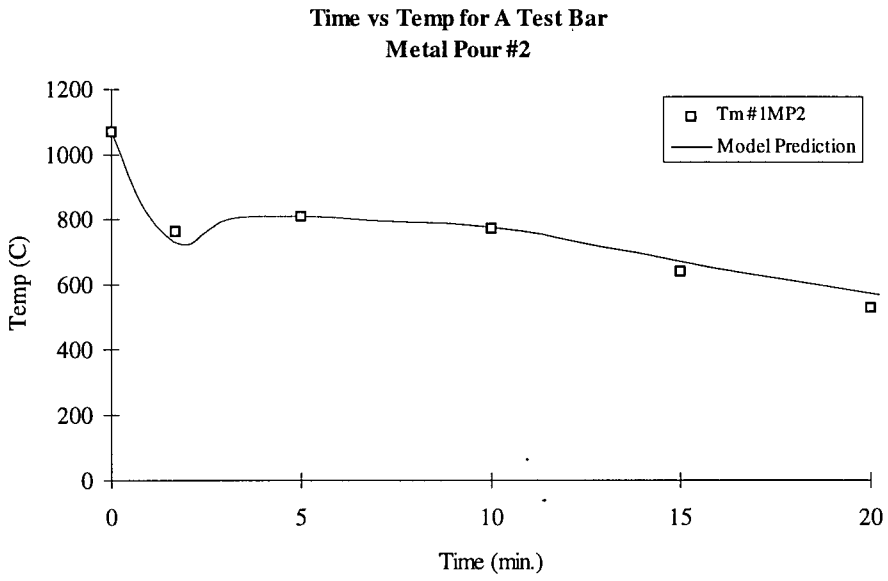

Figure 6-13 Thermocouple and thermal simulation (#2) results for the test cylindrical mould, mould preheat=1800 °F, metal temperature=2700 °F, refer to Table 6-3 for thermocouple position

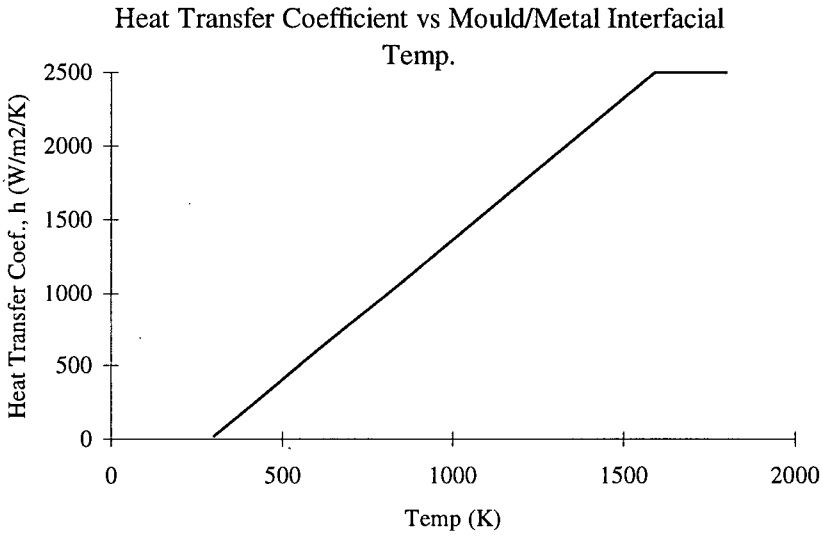

Figure 6-14 Graphical representation of the heat transfer coefficient between the metal and mould as a function of the interfacial temperature.

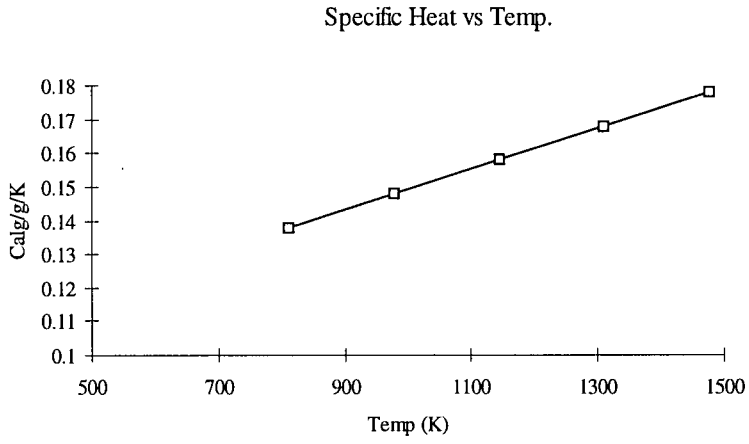

Figure 6-15 Variation in heat capacitance with temperature

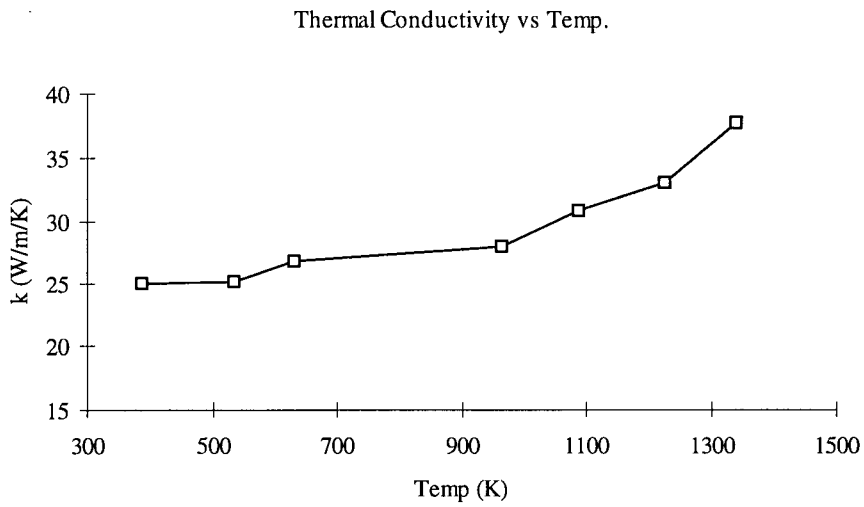

Figure 6-16 Variation in conductivity with temperature

7. Investment Casting Thermal Simulation Results

Having developed the model and validated the boundary conditions for a simple cylindrical casting, effort was focused on the development of a model for the actual diesel valve seal. Two models of the diesel valve seal were developed to assess the distribution of porosity in the problematic casting configuration. The first was a two-dimensional model of the casting and the second was a partial three-dimensional model to account for an increase in geometric and computational complexity. The rationale for this approach was that it allowed the predictive capability of each model to be assessed relative to the effort required to obtain the results, both in terms of the time required to develop the model and the computational resources needed to solve it.

7.1 Two Dimensional Model of the Valve Seal showing Porosity

A simple two-dimensional model consisting of a single cluster of valve seals was developed and run. A transverse slice through a single cluster, as shown in Figure 7-1, was used. The consequence of assuming two-dimensional heat flow was that the valve seal was treated as an infinite cylinder - i.e. there was no heat flow in the axial direction. Unfortunately, this was a poor representation of the actual heat flow that occurred in the component. Nevertheless, this approach was worth assessing since the model development time was short and the demand for computational resources was low.

The contour plots in Figure 7-2 (a-d) show the solidification front at various time intervals. Due to the configuration of the casting, solidification begins at the outer diameter at a point along the circumference furthest from the ingate, and the reason for

this is illustrated schematically in Figure 7-3. Referring to Figure 7-3, heat was removed initially from the mould surface by radiation, conduction and convection to the surrounding environment. Due to the mould configuration, heat was removed most rapidly from the outside of the mould surface on the side of the seal opposite to the ingate (labeled as 'a'). The outer surface of the mould, labeled as 'b' and 'c', was partially insulated due to self-radiation and thus solidification proceeded at a later time than region 'a'. Around the inside circumference of the mould, radiative heat exchange was significant and this limited heat loss. Heat may have been transferred from the center of the ring to the surrounding environment through conduction/convection to the air in the axial direction. Overall, it was difficult to quantify the amount of heat removed from the inner surface which points out the need for additional thermocouple measurements on this complex mould. Section 7.3 assessed the importance of heat removed from the inner surface of the mould during the cooling.

The directions with which solidification proceeded through the casting are illustrated in Figure 7-2 (a-d). As discussed above, solidification begins on the outer diameter of the seal at the point along the circumference furthest away from the ingate. The solidification front then continues around the circumference of the ring, and the last region to solidify is the metal adjacent to the ingate. From these solidification contour profiles, it is apparent that there is no encapsulation of liquid metal consistent with the absence of macroporosity in the casting. Figure 7-4 shows a contour plot of the local solidification time. This plot serves as an effective means of observing the progression of solidification in the casting and helps to predict areas that may develop macroporosity.

The model's thermal history was examined and contour plots were produced to show the thermal gradients, solidification velocity, and solidification time for use in the assessment of porosity using the Niyama and L.C.C. criteria. However, attention must be taken when employing the thermal gradient because for any particular node, the thermal gradient changes during the course of solidification. For example, contour plots at the onset of solidification, 50% solidified, and at the end of solidification are shown in Figure 7-5(a-c) respectively. As can be seen, the thermal gradients are more shallow throughout the casting at the onset of solidification (Figure 7-2 (a)) than at the end of solidification (Figure 7-2 (c)). Since both the Niyama and the L.C.C. criteria depend on the thermal gradient for the assessment of porosity formation, a temperature must be selected for the evaluation of the thermal gradient. Niyama *et al.*[12] raised concern regarding what temperature should be employed; For example, should it be at the end of solidification or at some solid fraction during solidification. The literature[6] suggested that, for many alloy systems, porosity can begin to occur at approximately 70% solid. At this solid fraction, liquid metal flows through a highly tortuous dendritic structure which offers a high degree of flow resistance. Porosity forms when the flow through the mushy zone is insufficient to fill the void created by the reduction in volume during cooling. Based on the literature[6], all calculations of the Niyama and the L.C.C. criteria use a thermal gradient calculated at a 70% solidification which corresponds to 1260 °C for Stellite Grade 3.

The thermal gradient contour plot, for the two-dimensional analysis at a solidified volume fraction of 70%, is shown in Figure 7-6. The thermal gradient contour plot was

compared with the schematic of the actual distribution of porosity (Figure 4-3). The porosity distribution was observed to occur when the thermal gradient was less than approximately 15 °C/cm. In comparison to the critical thermal gradient for porosity evolution for steel, as calculated by Pellini[9] and Pellini and Bishop[10], the present value was approximately five to six times higher.

The Niyama criteria[12], using the semi-empirical formulation of eqn. 2-6, suggested that areas with a ratio of less than 1 $°C^{1/2}/cm\ min^{1/2}$ are sensitive to the formation of porosity. With this value in mind, a contour plot of the porosity distribution (in red) predicted by the Niyama criteria was generated and is presented in Figure 7-7. Comparing the results of this plot (Figure 7-7) with that observed in the actual component (Figure 4-3), the results from the two-dimensional approach were unsatisfactory and the Niyama criteria under predicted the extent of the porosity. The results were worse for the L.C.C. criteria.

Unfortunately, the source of the poor agreement was unclear. It may have been a result of the assumption of a two-dimensional heat flow, or alternatively, a failure of the semi-empirically based Niyama or L.C.C. criteria to predict porosity in a Stellite alloy. This uncertainty illustrates the drawbacks of the empirical based approaches when they are applied outside the conditions for which they have been developed and verified.

7.2 Partial Three-Dimensional Model of the Diesel Valve Seal Showing Porosity

To determine whether the criteria or the thermal model was responsible for the poor agreement, a partial three-dimensional analysis was used to better reflect the heat

flow conditions prevailing in the valve seal. The computational size of the problem precluded an analysis of the entire cluster of seals with the existing hardware. Fortunately, the cluster could be subdivided by taking advantage of symmetries in the flow of heat and this reduced the size of the problem. The presence of seals on either side (Figure 7-1) allowed the flow of heat in a transverse plane to and from adjacent seals to be assumed negligible about a *y-z* and *x-z* plane bisecting the seal at the middle of the ingate (Figure 7-8). Likewise, a seal located approximately mid-height in the cluster had negligible heat exchange with seals located above and below. Hence, the analysis could be further sub-divided to a half section of two adjacent seals together with a quarter section of the down sprue and two half ingates, as shown in Figure 7-8. [††]

The partial three-dimensional diesel valve seal model was run, and a contour plot showing the solidification time at mid-height is shown in Figure 7-9. In comparison to the solidification time of the two dimensional model in Figure 7-4, the three-dimensional valve seal model solidified in about one fifth of the time. Thus, the effect of a three dimensional heat flow analysis had a profound influence on the rate of heat extraction.

The results of the thermal gradient analysis for the three-dimensional model are illustrated in Figure 7-10. When compared to the X-ray results in Figure 4-3, the porosity seemed to occur at thermal gradients less than approximately 5 °C/cm. This

---

[††] Note: this restricts the applicability of the analysis to those seals located at approximately half the height in the casting

value is closer to the findings of the previous study [9,10] which found the critical thermal gradient to be 3 °C/cm for steel.

Porosity predictions using the Niyama and the L.C.C. criteria are shown as mid-plane contour plots in Figure 7-11 and Figure 7-12 respectively. In comparison to the X-ray results in Figure 4-3, the model predictions closely agree with the actual porosity distribution found within the component. Thus, the assumption of an infinite cylinder used for the two-dimensional analysis was not valid for this casting configuration. Hence, the failure of the model to predict porosity was a result of the inadequate description of the heat flow and was not a result of the Niyama or the L.C.C. criteria.

7.3 Heat Flux at the Inner Mould Surface

There was some concern about the boundary condition for the inner mould surface/air interface, shown schematically in Figure 7-8. During cooling, the outer surface of the mould radiated heat to its surroundings and conducted heated through the ambient air. However, the inner mould surface radiated heat to itself and transferred heat to the air within the ring. If the air inside the rings was maintained at the same temperature as the mould surface (assuming no convection in the axial direction), and there was no net loss due to radiation, then one may assume there was negligible heat transfer through the inner mould surface to the atmosphere. However, it was more likely that there were convective air currents moving through the ring, transferring heat to the environment. Two models (with and without heat exchange on the inner mould surface) were constructed to assess the inner mould boundary conditions. These models were run

and the solidification times for specific nodes and the predicted porosity distributions were compared.

The thermal histories using the two sets of boundary conditions for three nodes are displayed in Figure 7-13. These particular nodes are found in the middle of the casting and mould at 90° circumferentially from the ingate, as illustrated in Figure 7-1. Applying a heat transfer boundary condition of h=20 $W/m^2/°C$ on the inner mould surface, as compared to zero heat flow, significantly affected the thermal history of these nodes, especially at the later stages of solidification. Also, heat flow through the mould's inner surface decreased the time for full solidification of node 3279 from 146 seconds (zero heat flow) to 114 seconds (h=20$W/m^2/°C$) , a change of about 28 %.

The predictions of porosity using the Niyama criteria for the two cases had varying results. When the heat transfer boundary condition (h=20 $W/m^2/C$, Tamb=30 °C) was applied to the inner mould surface, the Niyama criteria slightly over predicted the distribution of porosity in Figure 7-11 (θ=116.0, d=5.9 mm) relative to the X-ray results in Figure 4-3. However, when a zero heat flux boundary condition or perfect insulation was applied on the inner mould surface, the Niyama criteria under predicted the distribution of porosity (θ=100°, d=3.4 mm) when compared with the X-ray results. Hence, based on the prediction of porosity, the boundary conditions lie somewhere between the limiting conditions examined.

In order to quantify the heat transfer coefficient at the inner mould surface, extensive thermocouple measurements in this area would be required. Then, using a trial

and error approach, one could match the thermal history of this section of the mould with that of the thermocouple data by adjusting the inner mould heat transfer coefficient.

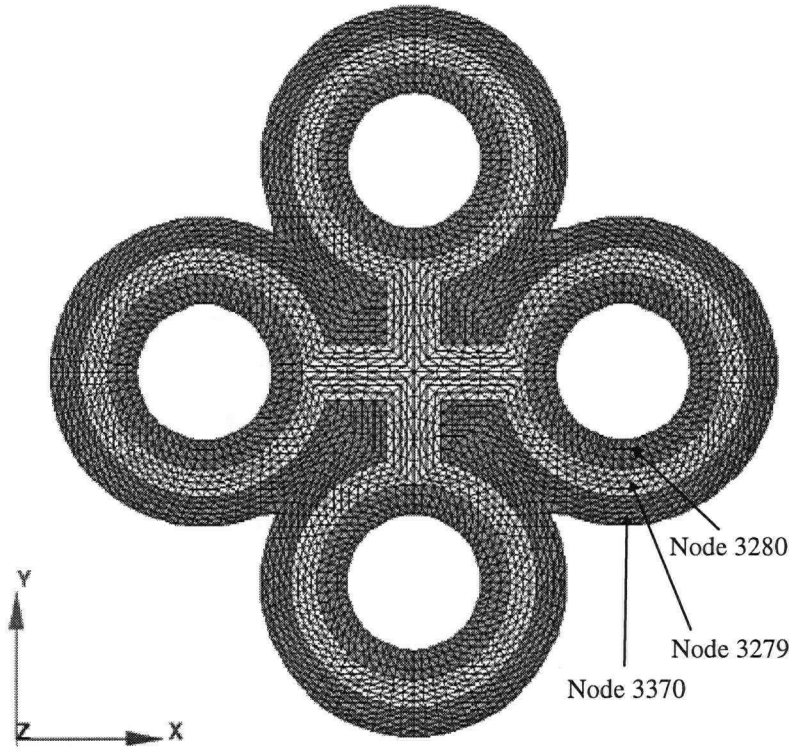

Figure 7-1 Two-dimensional finite element mesh used to simulate the heat flow through a transverse section of a single cluster for an investment cast diesel seal.

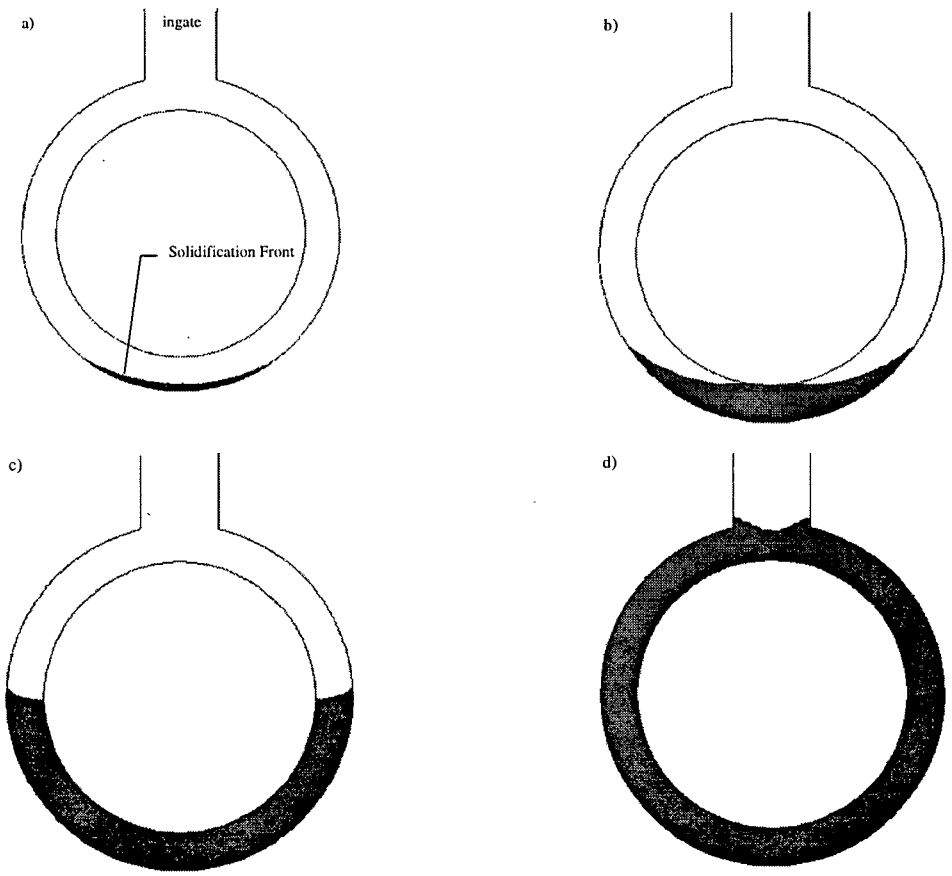

Figure 7-2 Contour Plots showing the front of the solidus isotherm for a single diesel valve seal at a)the onset of solidification, b) 20 seconds into solidification, c) 140 seconds into solidification d) 960 seconds into solidification (the mould is not shown in the diagram)

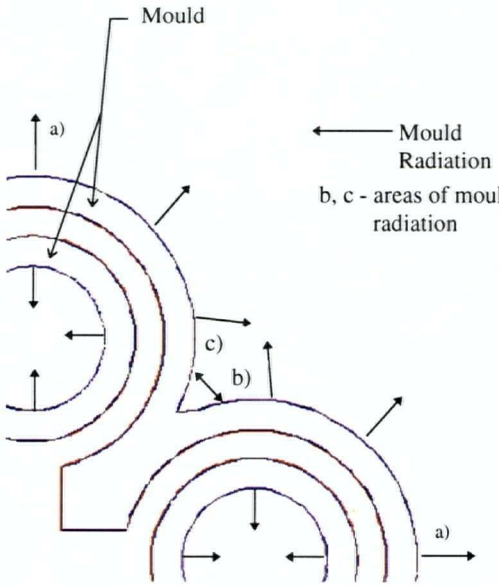

Figure 7-3 Diagram showing the removal of heat through radiation and heat conduction/convection from the outer surface of the mould.

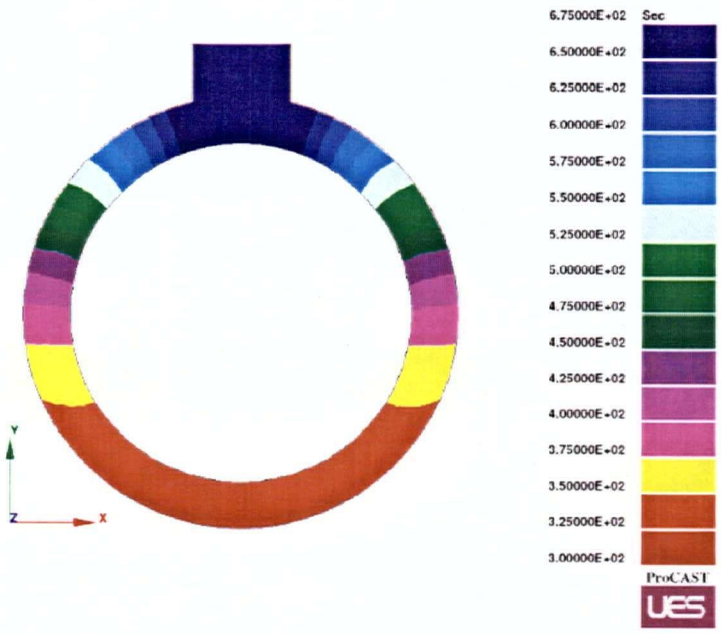

Figure 7-4 Solidification Time (sec.) for the two-dimensional analysis of the diesel valve seal.

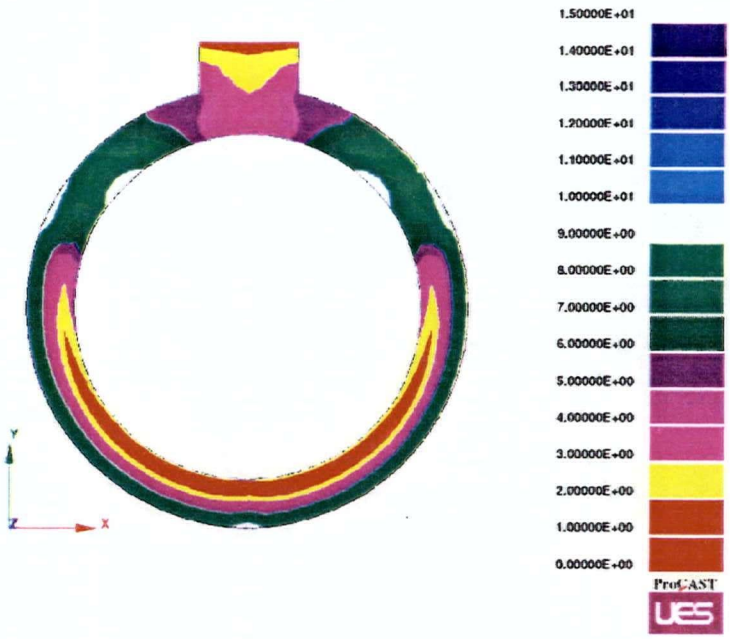

Figure 7-5a A contour plot showing the thermal gradient (°C/cm) when any particular element begins to solidify (1320 °C)

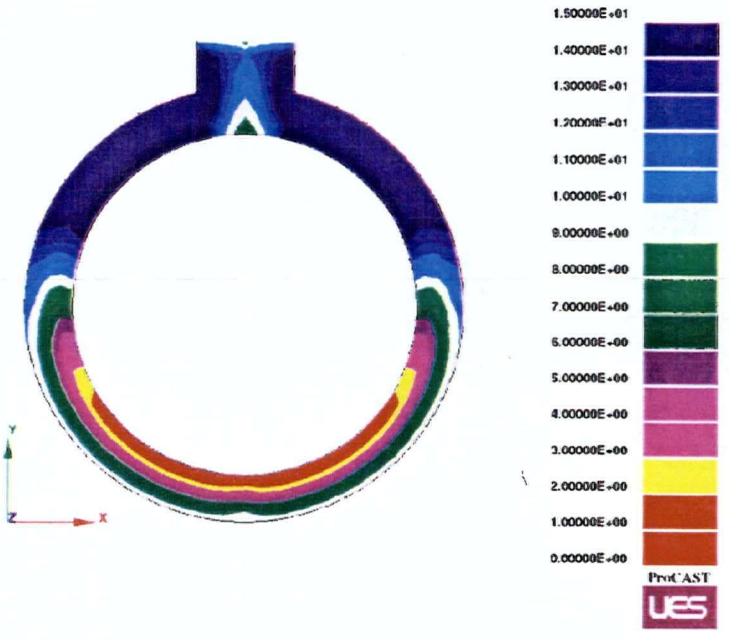

Figure 7-5b A contour plot showing the thermal gradient (°C/cm) when any particular element is at about 50% solidified (1280 °C)

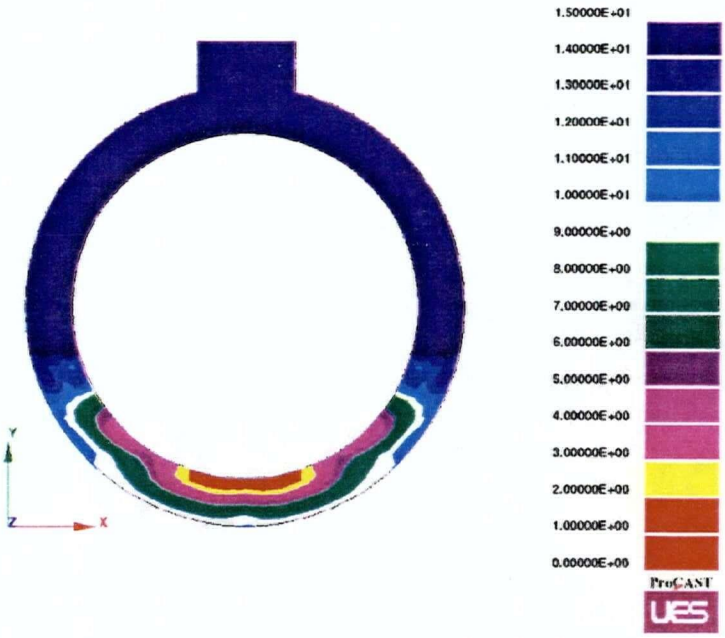

Figure 7-5c A contour plot showing the thermal gradient (°C/cm) when the element temperatures are at the end of solidification (1235 °C)

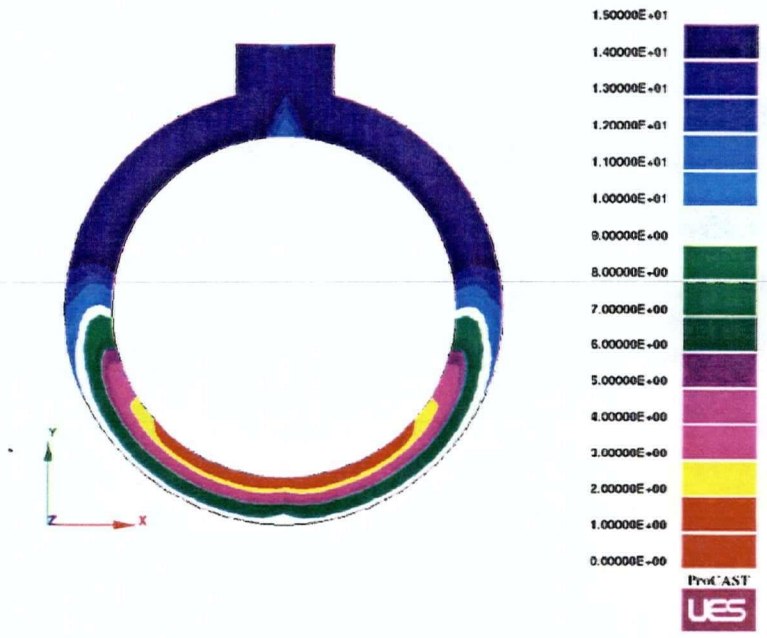

Figure 7-6 A contour plot showing the thermal gradient (°C/cm) at 70% solidified (1260 °C)

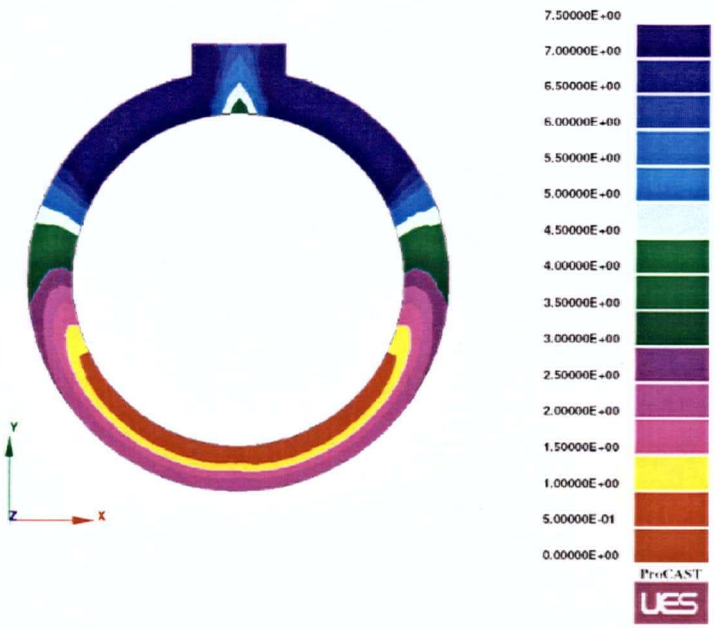

Figure 7-7 Two dimensional analysis showing the porosity prediction (in red) for a single diesel valve casting using the Niyama criteria ($°C^{1/2}/cm\ min^{1/2}$).

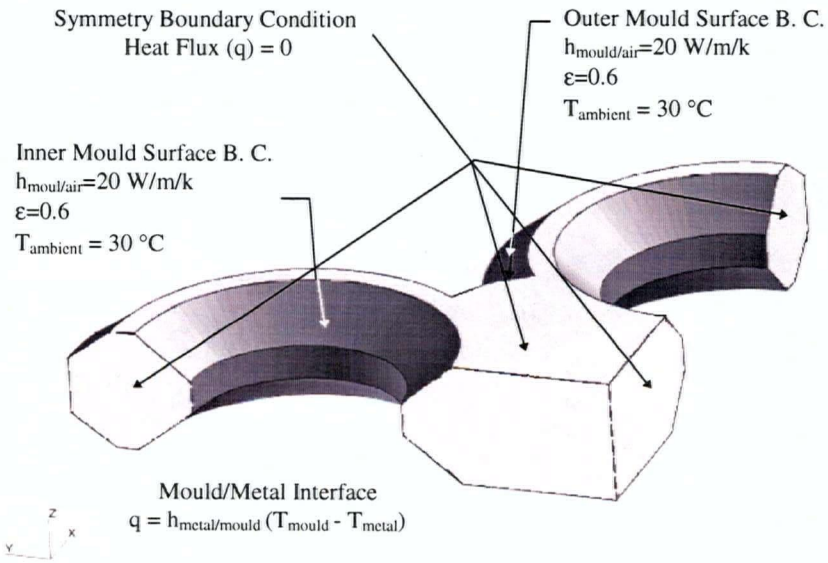

Figure 7-8 Diagram showing the boundary conditions for the partial three-dimensional model used to simulate the diesel valve casting

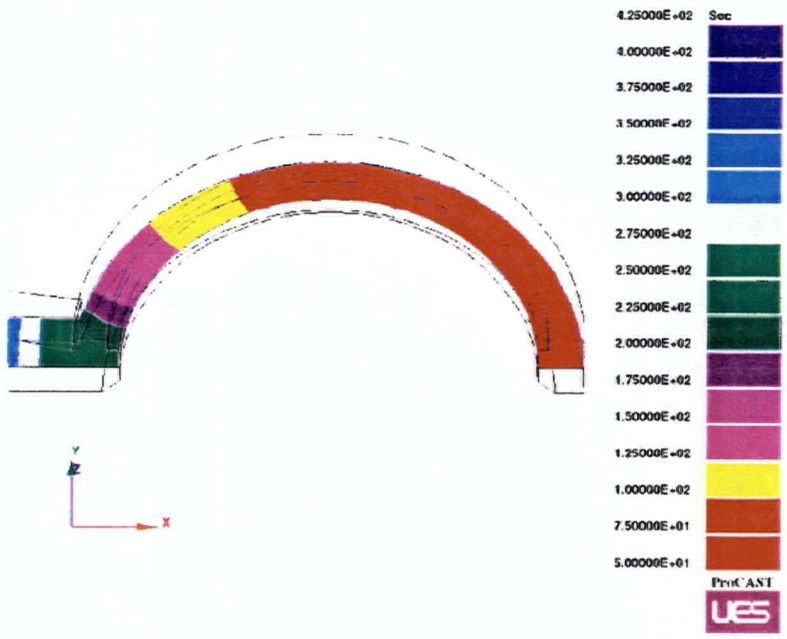

Figure 7-9 The solidification time (sec.) of a transverse slice through the diesel valve seal.

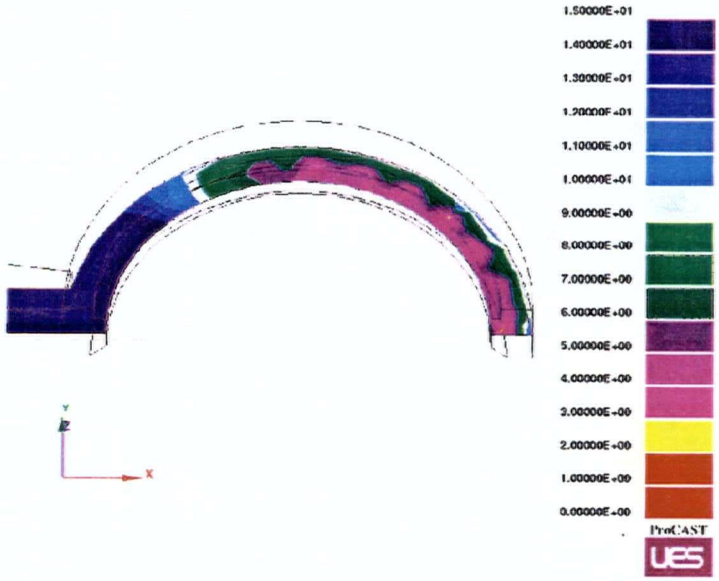

Figure 7-10 Thermal Gradient contour plot of a transverse slice through the diesel valve seal.

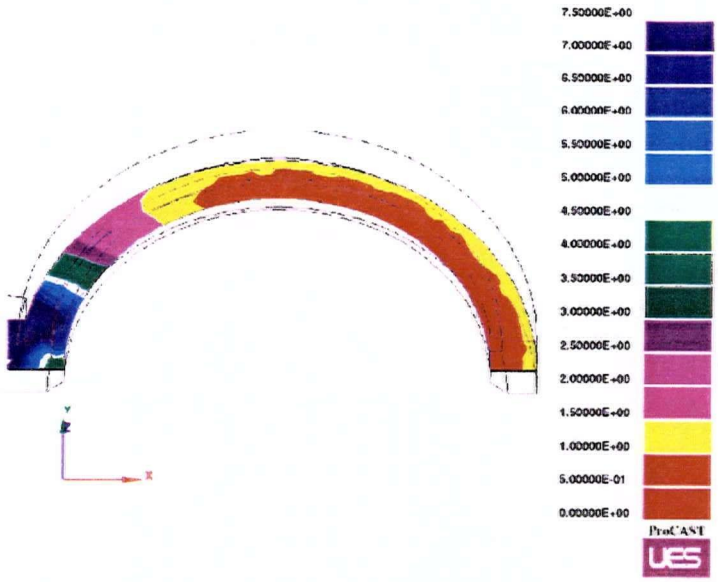

Figure 7-11 A transverse slice of the diesel valve seal showing the porosity prediction (in red) using the Niyama criteria (°C/cm/min$^{1/2}$), θ = 116.0, d = 5.9 mm

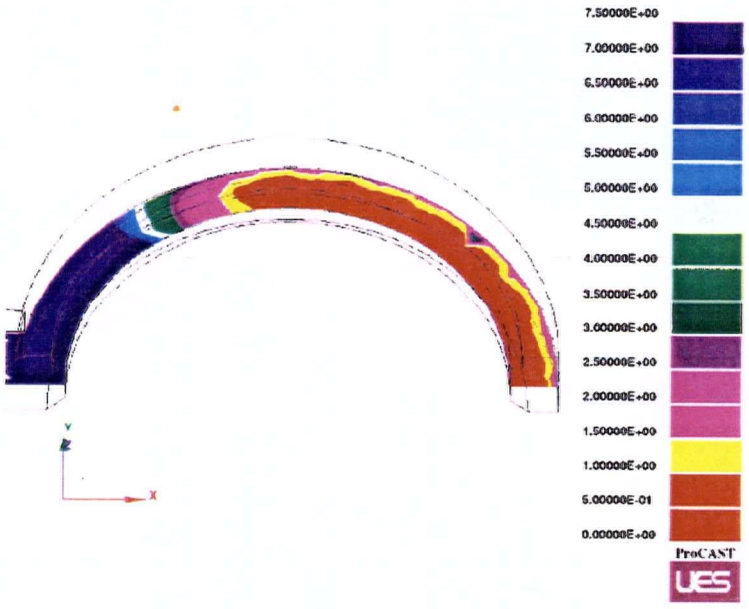

Figure 7-12 A transverse slice through the diesel valve seal showing the porosity prediction (in red) using the L.C.C criteria (°C min$^{5/3}$/cm^2), θ=107°, d=6.2 mm

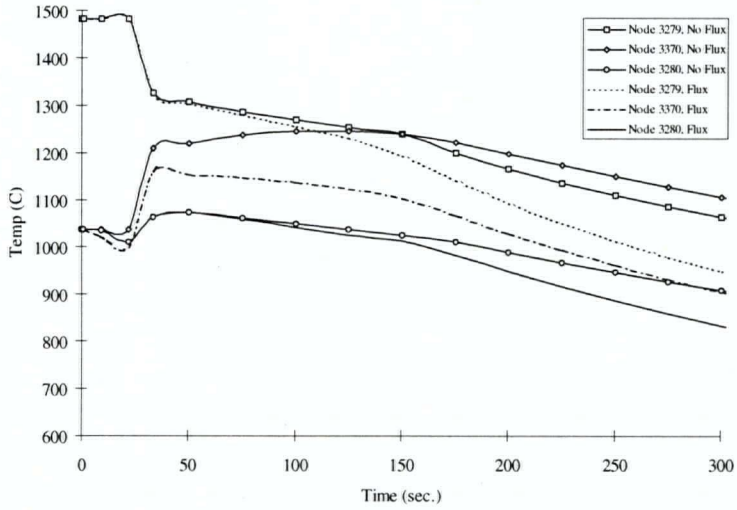

Figure 7-13 Graph showing the two sets Thermal Histories for Nodes 3280, 3279, 3370. No Flux assumes perfect insulation at the mould inner surface, Flux assumes an air/mould heat transfer coefficient.

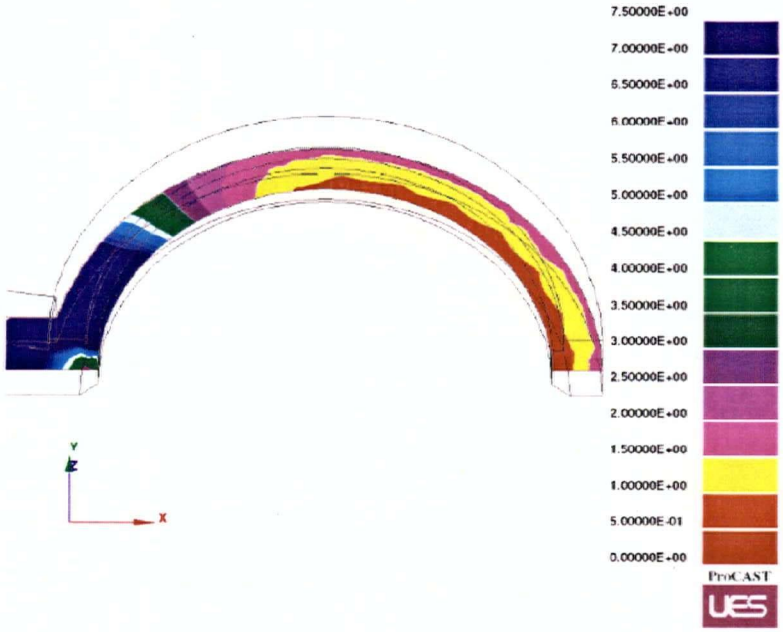

Figure 7-14 Results of a transverse slice through the diesel valve seal showing the porosity prediction (in red) using the Niyama criteria ($°C^{1/2}/cm/min^{1/2}$), assumes no heat flux through the inner mould surface. θ=101°, d=3.46 mm.

8. Reconfiguring the Mould to Obtain Zero Porosity using Modeling Techniques

Having completed an assessment of the porosity predictive capability of the model employing the Niyama and L.C.C. criteria, the focus was shifted to finding alternative feeding configurations to minimize porosity.

8.1 Feeding the Diesel Valve Seat Casting Using Two Ingates

A three dimensional model of the diesel valve seal was modified so that two ingates were used to feed the casting with the downsprue through the middle of the seal (Figure 8-1). The idea behind increasing the number of ingates was to manipulate the thermal history of the casting by altering the thermal gradient and solidification rate in order to reduce the porosity.

The model incorporated symmetry boundary conditions so that only a quarter of the casting had to be modeled, as shown in Figure 8-2a. The model encompassed a quarter section of both the downsprue and the casting, and one half of an ingate feeding the casting. Heat transfer at the mould/metal interface was accounted for using the temperature variant heat transfer coefficients developed in Chapter 6. Referring to Figure 8-2b, zero heat transfer was assumed on the top and bottom faces of the mould because of the presence of additional seals above and below. A heat transfer coefficient of 20 $W/m^2/°C$ was employed on the outside surface of the mould.

The model was run, and a contour plot showing the solidification time is shown in Figure 8-3. In comparison with the solidification time for a single ingate configuration in Figure 7-9, the effect of having one casting per layer and the new placement of the downsprue through the ring, collectively decreased the solidification time by approximately 40 seconds.

A thermal gradient contour plot through the mid-plane of the casting was calculated at 70% solidified (1260 °C) and is shown in Figure 8-4. This plot shows that regions of low thermal gradients (below the 5 °C/cm criteria) exist close to the inner surface, across from the downsprue and between the ingates. In comparison to the thermal gradient contour plot of the casting with a single ingate, shown in Figure 7-10, the effect of having two ingates decreased the size of the region with a low thermal gradient.

Applying the Niyama and the L.C.C. criteria to the thermal history resulted in the contour plots shown in Figure 8-5 and Figure 8-6, respectively. Both criteria predicted porosity adjacent to the inner diameter between the two ingates. In comparison to the porosity predicted from the previous casting with a single ingate in Figure 7-11 and Figure 7-12, the problematic area decreased in size. The present study did not incorporate a fluid model during the thermal simulations. Therefore, this decrease in porosity could only be attributed to the effect of an additional ingate and central downsprue on the diffusive flow of heat.

8.2 Feeding the Diesel Valve Seal Using Three Inner Ingates

In an attempt to further reduce the porosity, a third ingate was added to the diesel valve seal as shown in Figure 8-7. Again, the model configuration, shown in Figure 8-8, utilized symmetry boundary conditions to reduce the size of the analysis to only a third of the casting. The boundary conditions at the mould/metal and the mould/air interfaces were the same as those adopted in the previous analysis.

The model was run and the solidification time contour plot through the mid-plane of the casting is shown in Figure 8-9. Increasing the number of ingates from two to three did not increase the solidification time appreciably (Figure 8-3 and Figure 8-9).

The thermal gradient contour plot in Figure 8-10, shows that there were still areas in the mid-plane that had low thermal gradients at 70% solid fraction. Applying the Niyama and the L.C.C. criteria to the model resulted in the contour plots shown in Figure 8-11 and Figure 8-12, respectively. As can be seen, there were still regions where there was a high probability of porosity formation. However, when compared to using only two ingates, three ingates decreased the problematic areas in the diesel valve seals by about 50%.

8.3 Feeding the Diesel Valve Seal Using Four Inner Ingates

As shown in the previous models, increasing the number of ingates for the diesel seal casting progressively decreased the problematic regions. A final attempt to model the diesel valve seal using four inner feed ingates was run with the configuration shown in Figure 8-13. To the limit the computational requirements, symmetry boundary

conditions were utilized which yielded a final model configuration in Figure 8-14. The model was comprised of two half ingates and quarter sections of the downsprue and the diesel valve seal.

The model was run, and the resulting solidification time contour plot is shown in Figure 8-15. In comparison to the previously run model in Figure 8-9, there was a slight increase in the solidification time for the diesel valve seal when the number of ingates was increased from three to four.

The thermal gradient contour plot, shown in Figure 8-16, reveals only a small, localized region comprised of low thermal gradients of 5°C/cm or less. The Niyama criteria (Figure 8-17) predicted a small localized pocket (in red) with a high probability for porosity formation. However, the L.C.C. criteria plot in Figure 8-18 shows only high contour values (greater than 2 °C $\cdot min^{5/3}/cm^2$), and this indicated that there was an unlikely chance of porosity formation at the problematic inner surface.

8.4 Discussion

The valve seal mould design was investigated to determine the effects of the incremental additions of ingates on porosity. The intent was to modify the thermal history of the casting so that the model would predict little or no porosity in the problematic areas. The problematic areas in the original casting were composed of shallow thermal gradients (less than 5°C/cm), where as feeding the casting from four ingates resulted in much steeper gradients. Hence, employment of four ingates and the new placement of the downsprue through the center of the casting reduced porosity

formation. Furthermore, this finding was also confirmed by the Niyama and L.C.C. criteria, which showed a reduction in the volume of material for porosity formation.

8.5 Feeding the Diesel Valve Seal from the Top Using Four Ingates

In contrast to the optimum mould configuration determined in the previous sections with ingates feeding the casting from the inner diameter of the seal, Deloro Stellite utilized four ingates located on the top of the casting (Figure 8-19). According to Deloro Stellite personnel, the optimized configuration successfully eliminated porosity. To verify this, the new configuration was modeled (Figure 8-20) which consisted of a quarter downsprue and diesel valve seal, and two half ingates. Boundary conditions for this model were similar to previous models in that symmetry boundary conditions, and metal/air and metal/mould interfacial heat transfer coefficients were employed at their respective faces (Figure 8-20) .

The model was run, and a mid-plane contour plot of the solidification time is shown in Figure 8-21. In comparison to the solidification time for the four inner feeding ingates, the time was approximately 40 seconds less.

Applying the Niyama and L.C.C. criteria to the new casting configuration (Figure 8-23 and Figure 8-24 respectively), porosity adjacent to the mould surface was predicted. The Niyama criteria (Figure 8-23) predicted porosity around the entire inner diameter of the diesel valve seal, while the L.C.C. criteria (Figure 8-24) predicted a localized pocket at the inner diameter between the two ingates. This model, using four top feeding ingates, predicted a large area of porosity and this disagreed with actual observations.

Upon examination of the differences in the geometry, it was apparent that the symmetry boundary conditions on the top and bottom of the casting (in the z direction) may not have been a valid assumption in the "top feed" configuration. To better reflect the heat flow conditions of the diesel valve seal, a system of three seals was modeled utilizing the boundary conditions in Figure 8-25.

A contour plot showing the thermal gradient through the mid section of the middle diesel valve seal is shown in Figure 8-26. In this plot, a pocket of low thermal gradients (< 5 °C/cm) was found adjacent to the inner diameter between the two ingates. As shown in previous models, this area of low thermal gradients may be prone to porosity formation.

Predictions of porosity utilizing the Niyama and the L.C.C. criteria are shown as mid-plane contour plots through the middle seal casting in Figure 8-27 and Figure 8-28 respectively. These plots predict a pocket of porosity at the inner diameter between the two ingates (shown in red).

The model utilizing four top fed ingates predicted very little porosity (Figure 8-27 and Figure 8-28) relative to the porosity found in the seal using a single ingate (Figure 4-3). Increasing the number of ingates from one to four and repositioning the downsprue altered the thermal gradients and solidification time of the system with the effect of a reduction of porosity. A summary of the porosity predictions using the Niyama and the L.C.C. criteria is tabulated in Table 8-1 with a reference schematic in Figure 8-29.

8.6 Examination of Porosity in the Optimized Casting

In order to asses the model predictions, the optimized diesel valve seal casting configuration was sectioned (Figure 8-30) to examine the extent of porosity in the areas suggested by the model analysis as potential areas containing porosity. This figure shows that there is an obvious porosity array (macro and microporosity) located within the downsprue, but there is no visible porosity in the actual diesel valve seal at this magnification. However, upon closer inspection of area "A" in Figure 8-30, shown in Figure 8-31, there is indeed porosity as suggested by the model. Further magnification (Figure 8-32) shows a network of porosity, at the scale of the interdendrite spacing. The porosity is not oriented in any direction, but rather evenly dispersed. It is much different than the porosity distribution in the original casting. The porosity shown in Figure 8-32 underwent image analysis and the computer calculated the porosity to be 2.75 % of the area. This is much smaller in comparison to the previous values calculated for the original casting configuration.

8.7 Advantages and Disadvantages for the New Casting Configuration

Clearly, there is an obvious advantage with the new casting configuration as there is an inherent reduction of porosity in the problematic areas. However, there is a drawback to the new configuration in that there is a greater demand for metal in the new gating system with four top fed ingates. As shown in Table 8-2, the initial mould configuration using a single ingate, required approximately 271 grams of metal per valve seal, including the downsprue, ingate, and component. The final mould configuration

using four top feed ingates, required approximately 562 grams. This is approximately twice as much metal as the single ingate configuration.

Increasing the size and number of ingates to feed metal to the casting elevates the cost of production. Any excess metal that is consumed during the casting process is removed from the component during the later stages of fabrication and is "thrown" in the scrap metal pile. For cheaper materials, this is not as great a concern but Stellite is an expensive alloy and loses some of its value from a virgin to a scrap condition. There is also a greater consumption of electricity per valve seal employing the larger gating systems to melt the metal for a casting. There is also a labor factor which also has to be considered i.e. more ingates may require more grinding/machining to complete the finished product. In order to assess its feasibility, the new casting configuration should undergo a cost evaluation to discern whether the new configuration is economically acceptable or other process routes must be considered.

There are other mechanisms that can be used to influence the thermal history of a casting. For example, heat sinks and insulation are commonly used in foundries as a method for controlling heat flow in order to minimize microporosity and eliminate macroporosity. Understanding the effect of these methods to control cast quality is of vital importance in a modern day foundry, but is beyond the scope of this investigation.

Table 8-1 Summary of porosity predictions for the various models and the actual porosity found in the two castings (one outer feed ingate and four top feed ingates)

Model, Porosity Criteria	Circumferential Angle (θ)	Depth of Porosity (d)
2-D one ingate, Niyama	128 °	2.7 mm
3-D one ingate, Niyama	232 °	5.9 mm
3-D one ingate, L.C.C.	212 °	6.2 mm
3-D one ingate, Niyama, interior surface insulated	200 °	3.4 mm
3-D one ingate, L.C.C., interior surface insulated	184 °	3.9 mm
two ingates, Niyama	42 °	3.1 mm
two ingates, L.C.C.	37 °	3.2 mm
three ingates, Niyama	35 °	3.2 mm
three ingates, L.C.C.	10 °	3.1 mm
four inner ingates, Niyama	< 5°	1.4 mm
four inner ingates, L.C.C.	nil	-
four top ingates, modeled a single layer, Niyama	90 °	3.9 mm
four top ingates, modeled a single layer, L.C.C.	34 °	3.9 mm
four top ingates, modeled three layers, Niyama	20 °	3.3 mm
four top ingates, modeled three layers, L.C.C.	12 °	3.0 mm
Actual Porosity from the single ingate casting	98 °	5.6 mm
Actual Porosity from the four top ingates casting	6 °	3.1mm

Table 8-2 The approximate weight of metal to make a single diesel valve seal (including gating, downsprue, and casting, this value does not take into account the pouring cup)

Casting	Approx. Weight of Metal
one gate (Figure 7-8)	271 grams
two gates (Figure 8-2)	527 grams
three gates (Figure 8-7)	546 grams
four inner gates (Figure 8-13)	538 grams
four top gates (Figure 8-19)	562 grams

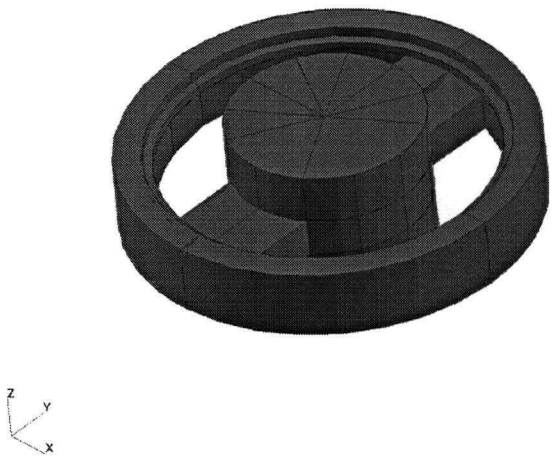

Figure 8-1There dimensional diagram for a new diesel valve seal configuration using two ingates to feed the casting.

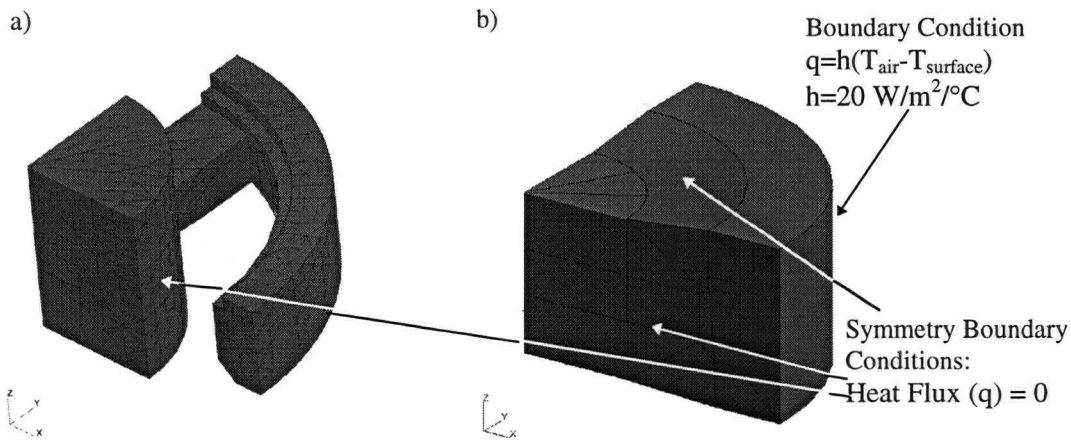

Figure 8-2 Three dimensional model used to simulate the configuration in Figure 8-1; a) without the mould shell, b) with the mould shell showing the boundary conditions.

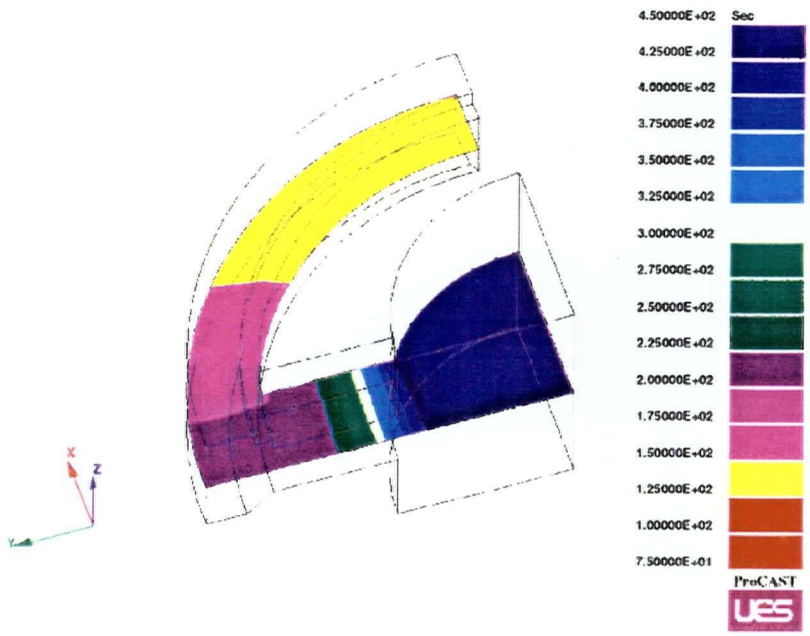

Figure 8-3 Solidification Time contour plot through the mid-plane of the Diesel Valve Seal Casting using two ingates to feed the casting.

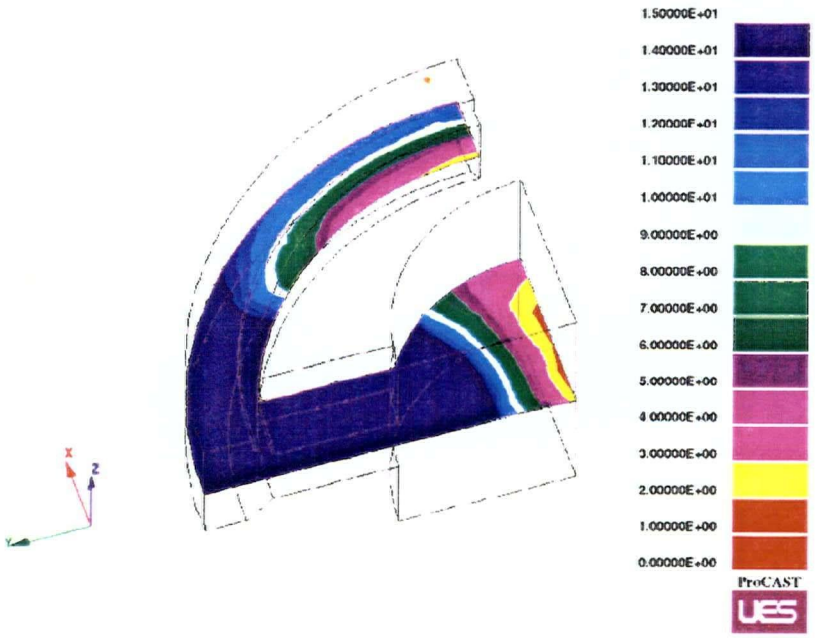

Figure 8-4 Thermal Gradient (°C/cm) Contour Plot through the mid-plane of the Diesel Valve Seal Casting using two ingates, Thermal Gradient taken when an element obtains 70% volume fraction Solid (1260 °C).

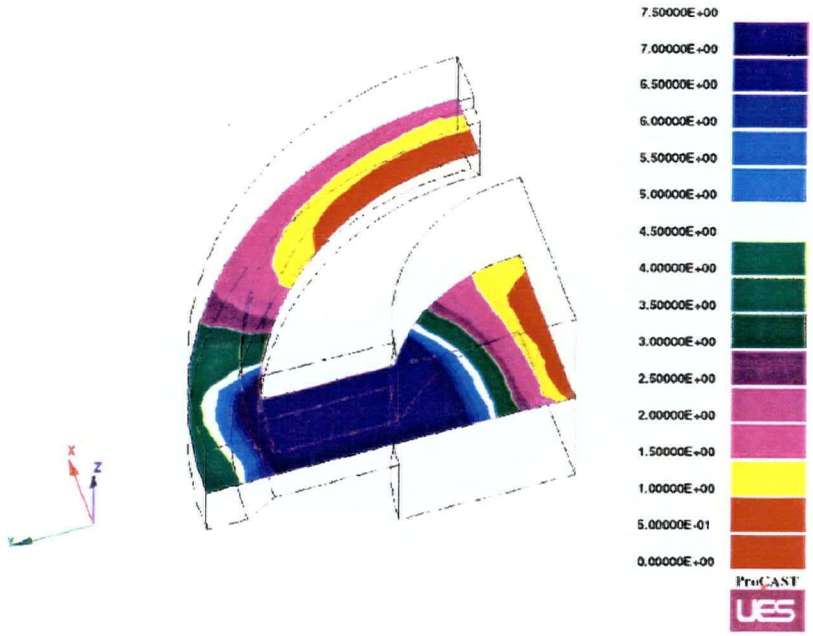

Figure 8-5 Niyama criteria ($°C^{1/2}$ $min^{1/2}$/cm) Contour Plot through the mid-plane of the Diesel Valve Seal, Thermal Gradient (°C/cm) taken at 1260 °C

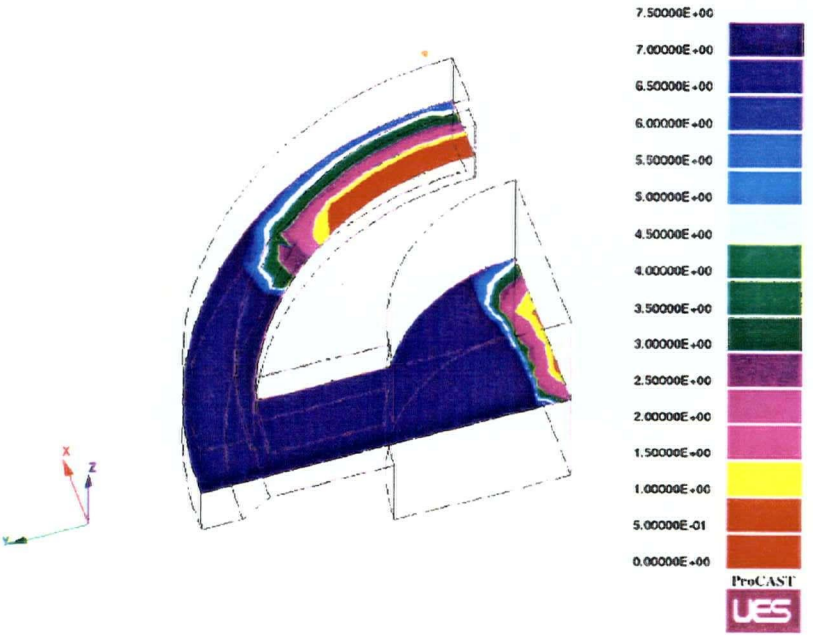

Figure 8-6 L.C.C. criteria (°C $min^{5/3}/cm^2$) Contour Plot through the mid-plane of the Diesel Valve Seal, Thermal Gradient (°C/cm) taken at 1260 °C

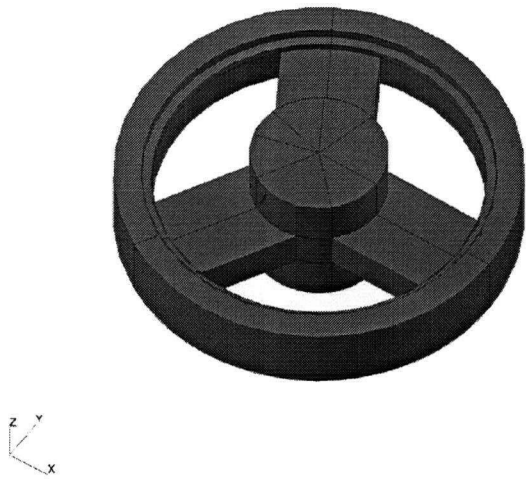

Figure 8-7 Three dimensional schematic of the new casting configuration using three ingates to feed the casting. The mould is not included in this diagram.

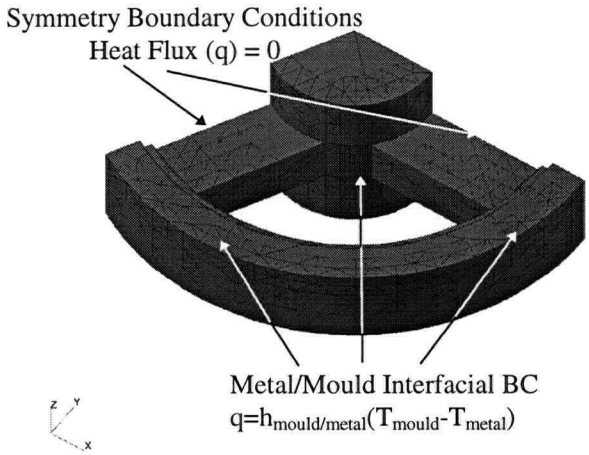

Figure 8-8 The model configuration using three ingates to feed the casting. This mould is not included in this diagram.

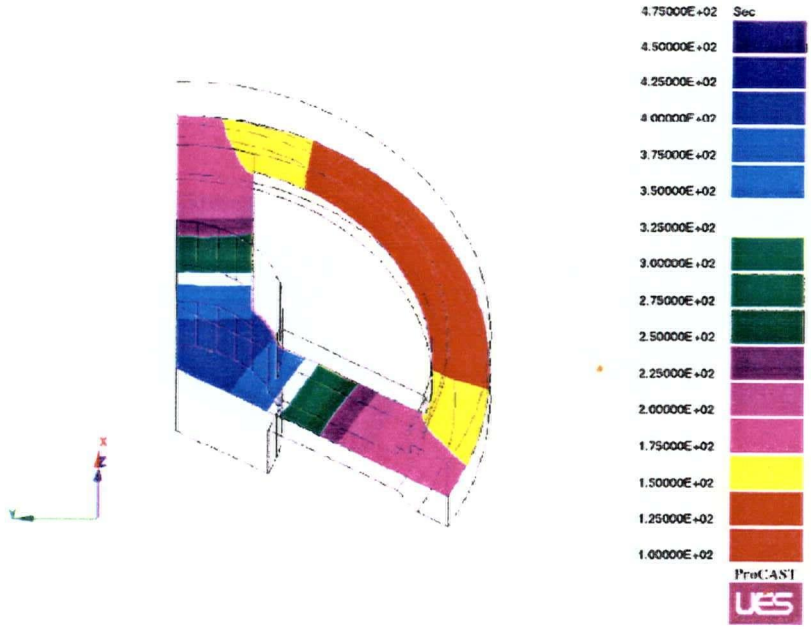

Figure 8-9 Solidification Contour Plot through the mid-plane of the Diesel Valve Seal using three ingates to feed the casting.

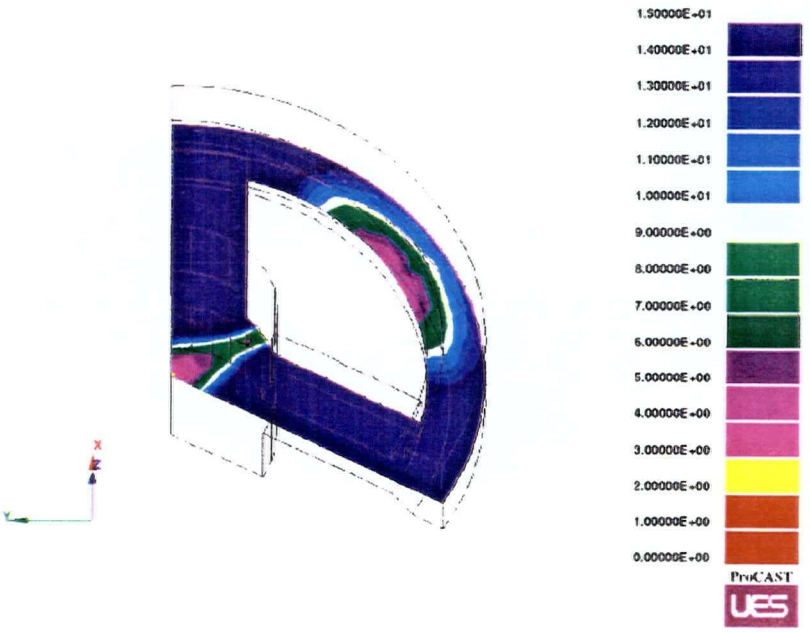

Figure 8-10 Thermal Gradient (°C/cm) Contour Plot through the mid-plane of the Diesel Valve Seal Casting using three ingates, Thermal Gradient taken when an element obtains 70% volume fraction Solid (1260 °C).

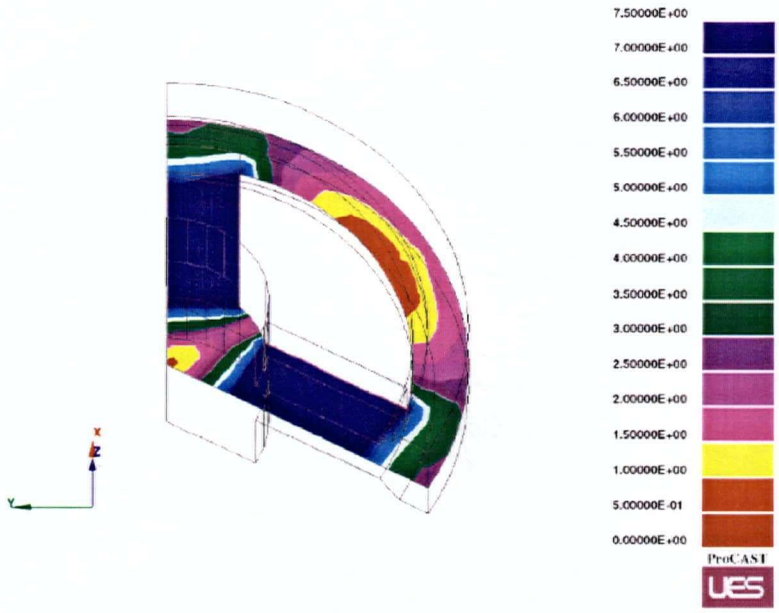

Figure 8-11 Niyama criteria ($°C^{1/2}$ $min^{1/2}$/cm) Contour Plot through the mid-plane of the Diesel Valve Seal using three ingates, Thermal Gradient (°C/cm) taken at 1260 °C

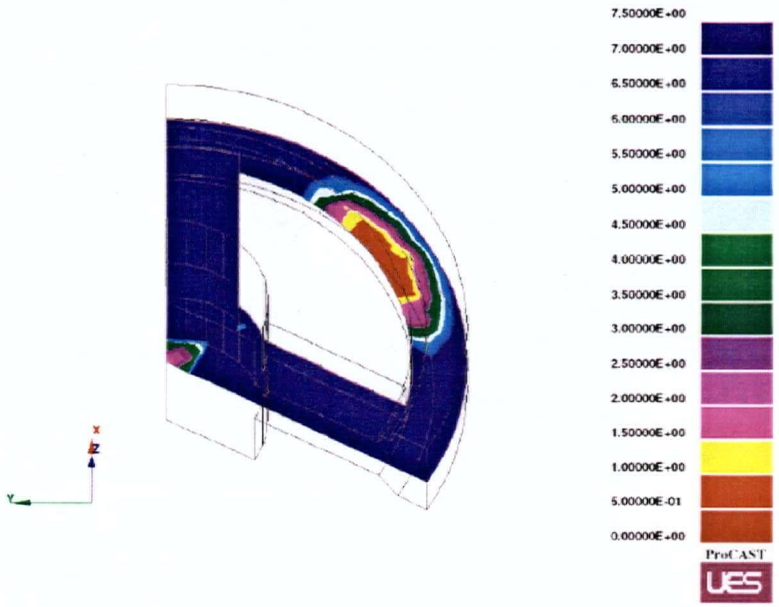

Figure 8-12 L.C.C. criteria ($°C\ min^{5/3}/cm^2$) Contour Plot through the mid-plane of the Diesel Valve Seal using three ingates, Thermal Gradient (°C/cm) taken at 1260 °C

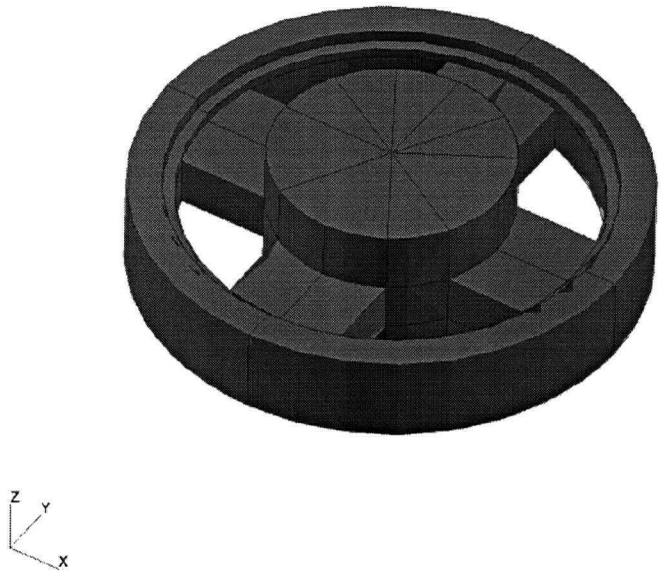

Figure 8-13 Three dimensional schematic of the new casting configuration using four ingates to feed the casting from the inner surface. The mould is not included in this diagram.

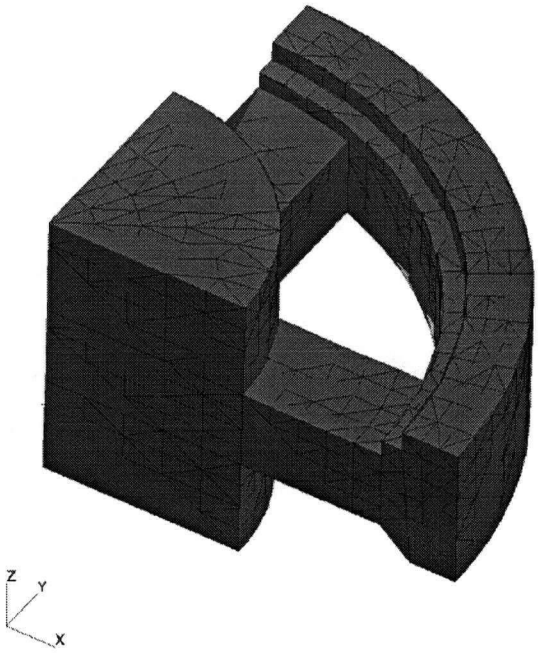

Figure 8-14 Three dimensional model diagram using four ingates to feed the casting from the inner surface. The mould is not included in this diagram.

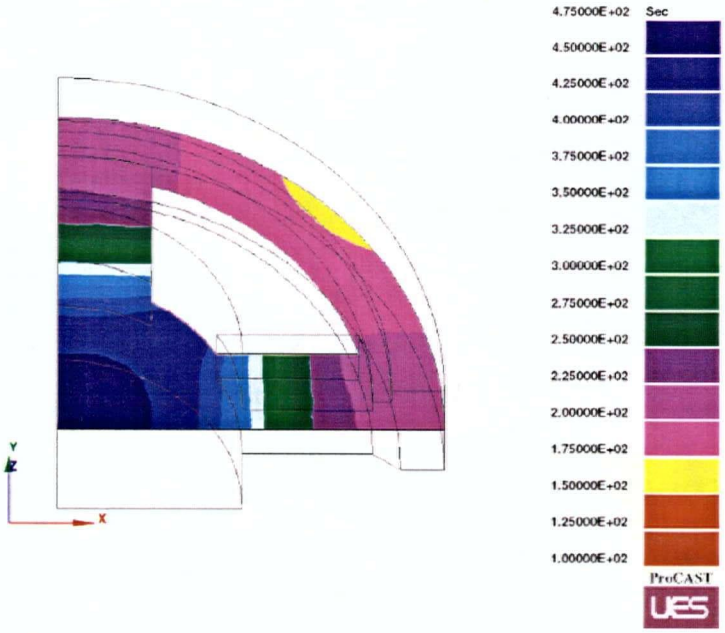

Figure 8-15 Solidification Time contour plot through the mid-plane of the casting using four inner surface ingates to feed the diesel valve seal.

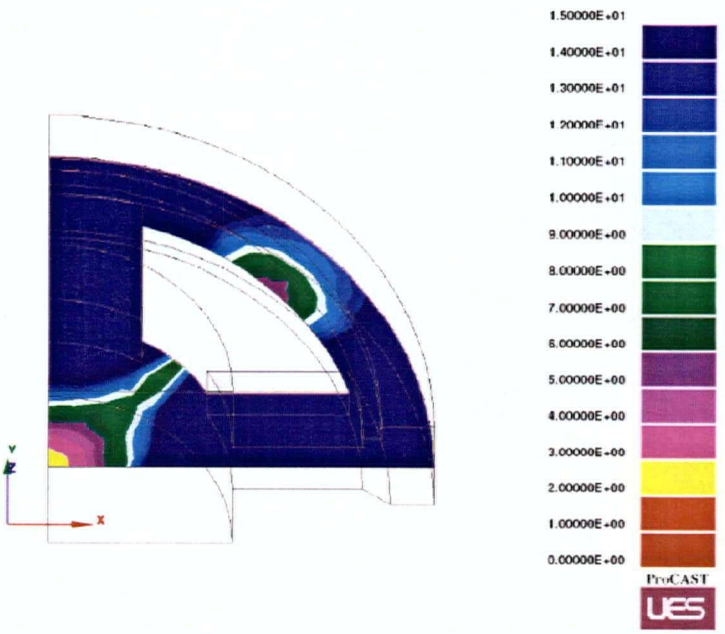

Figure 8-16 Thermal Gradient (°C/cm) Contour Plot through the mid-plane of the Diesel Valve Seal Casting using four inner surface ingates, Thermal Gradient taken when an element obtains 70% volume fraction Solid (1260 °C).

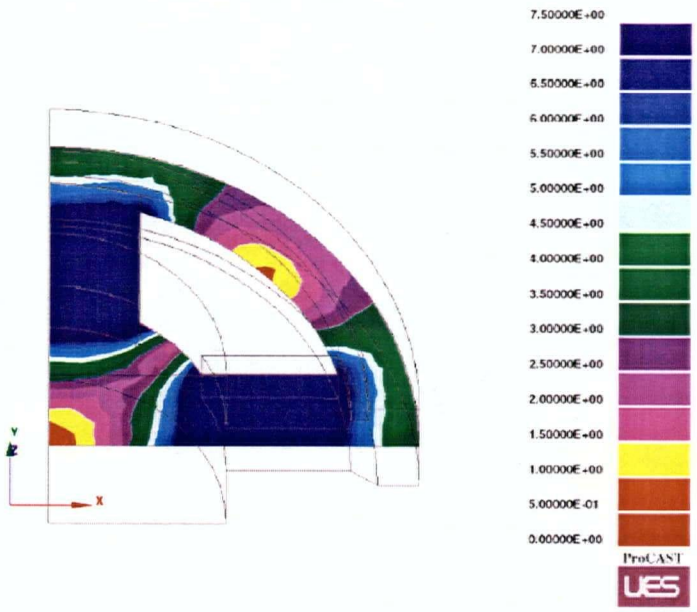

Figure 8-17 Niyama criteria (°C$^{1/2}$ min$^{1/2}$/cm) Contour Plot through the mid-plane of the Diesel Valve Seal using four inner surface ingates, Thermal Gradient (°C/cm) taken at 1260 °C

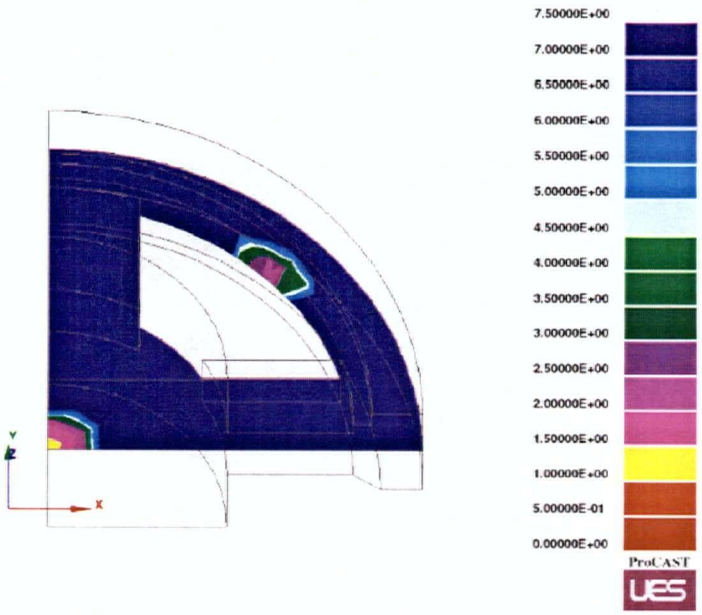

Figure 8-18 L.C.C. criteria (°C min$^{5/3}$/cm^2) Contour Plot through the mid-plane of the Diesel Valve Seal using four inner surface ingates, Thermal Gradient (°C/cm) taken at 1260 °C

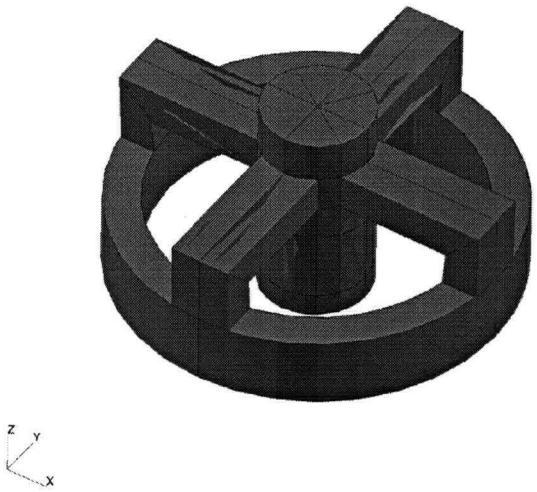

Figure 8-19 Three dimensional schematic of the new casting configuration using four top feeding ingates to feed the casting. The mould is not included in this diagram.

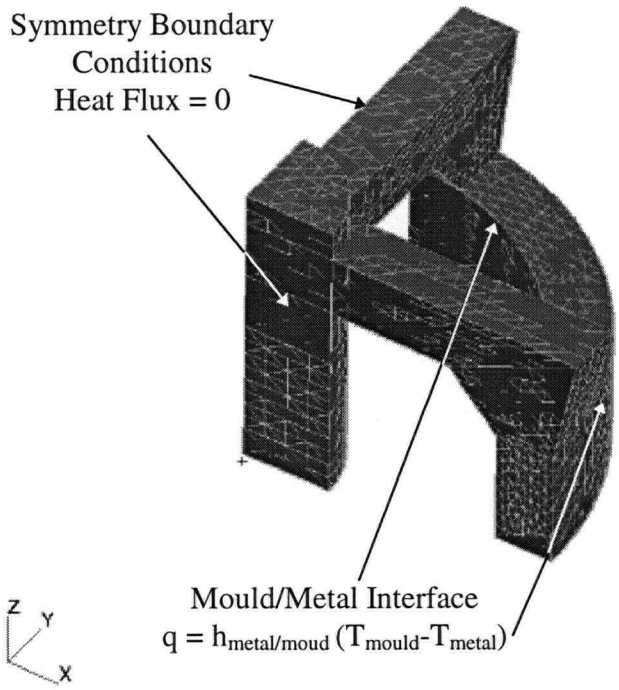

Figure 8-20 Three dimensional model diagram using four top feeding ingates to feed the casting. The mould is not included in this diagram.

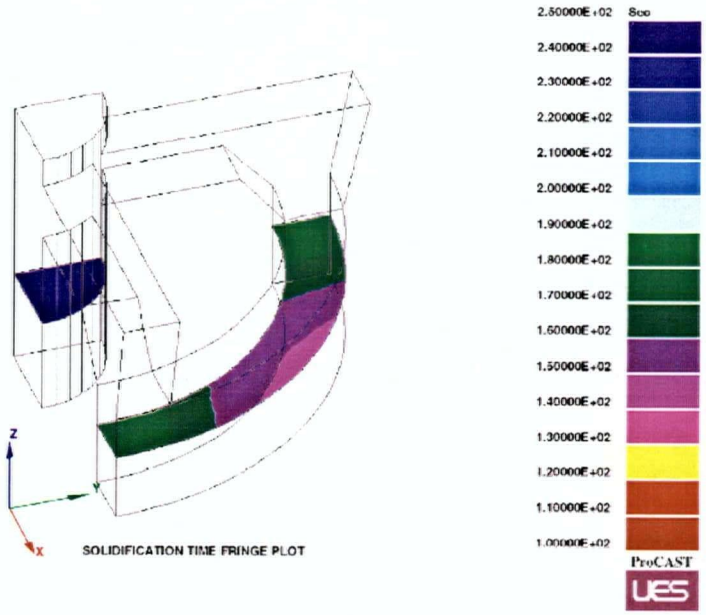

Figure 8-21 Solidification Time contour plot through the mid-plane of the casting using four top feeding ingates to feed the diesel valve seal.

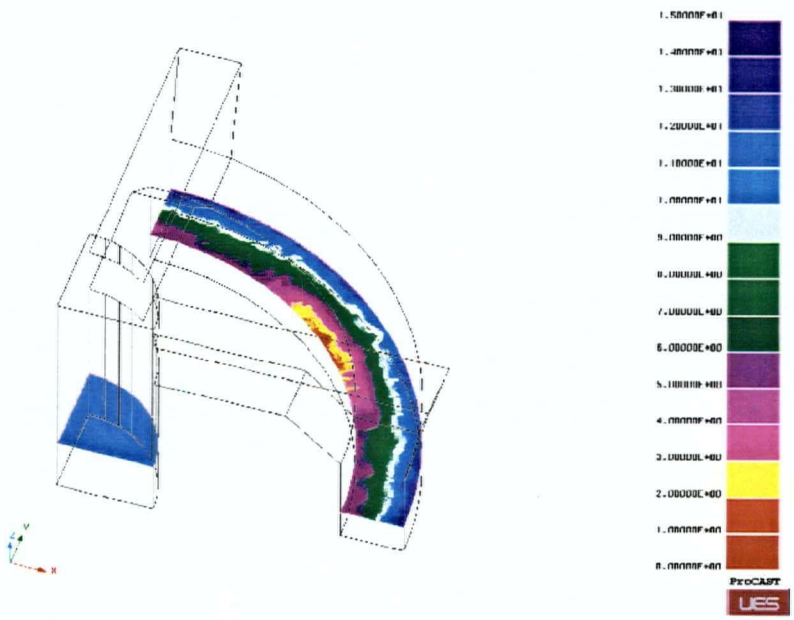

Figure 8-22 Thermal Gradient (°C/cm) Contour Plot through the mid-plane of the Diesel Valve Seal Casting using four top feeding ingates, Thermal Gradient taken when an element obtains 70% volume fraction Solid (1260 °C).

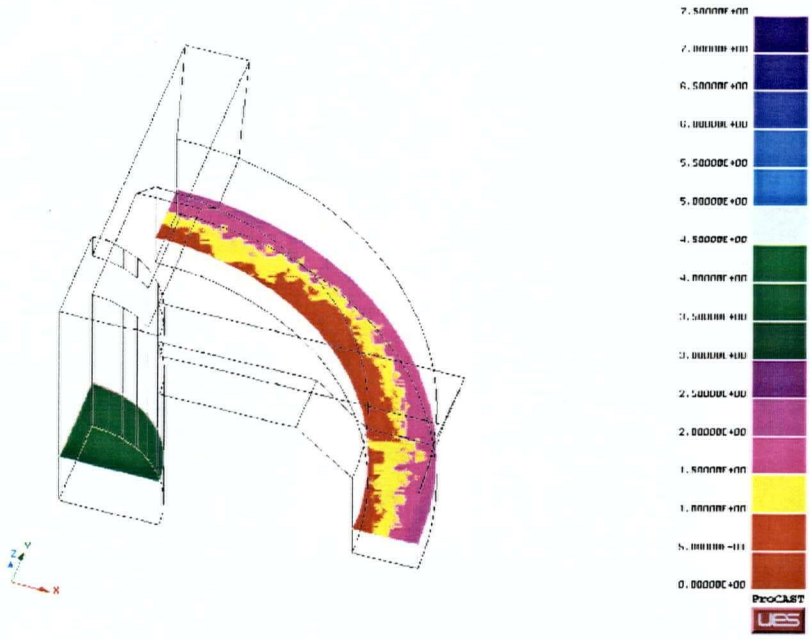

Figure 8-23 Niyama criteria ($°C^{1/2}$ $min^{1/2}$/cm) Contour Plot through the mid-plane of the Diesel Valve Seal using four top feeding ingates, Thermal Gradient (°C/cm) taken at 1260 °C

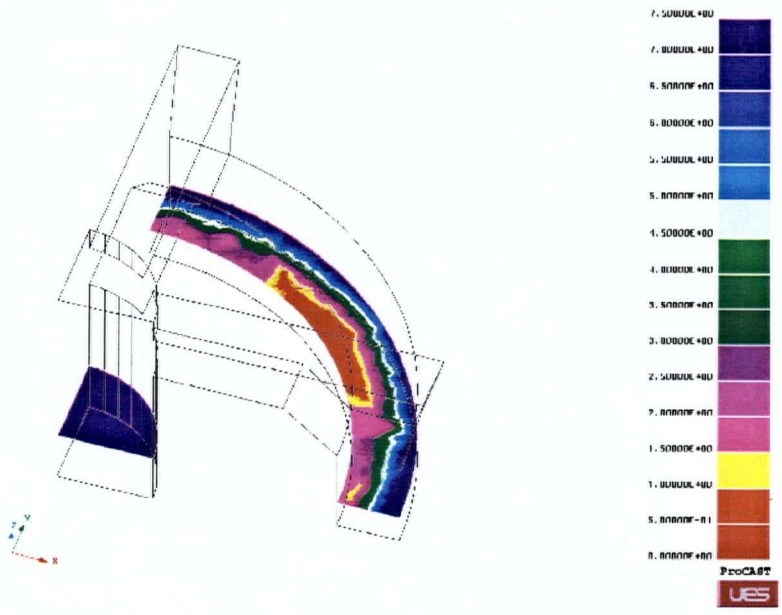

Figure 8-24 L.C.C. criteria (°C $min^{5/3}/cm^2$) Contour Plot through the mid-plane of the Diesel Valve Seal using four top feeding ingates, Thermal Gradient (°C/cm) taken at 1260 °C.

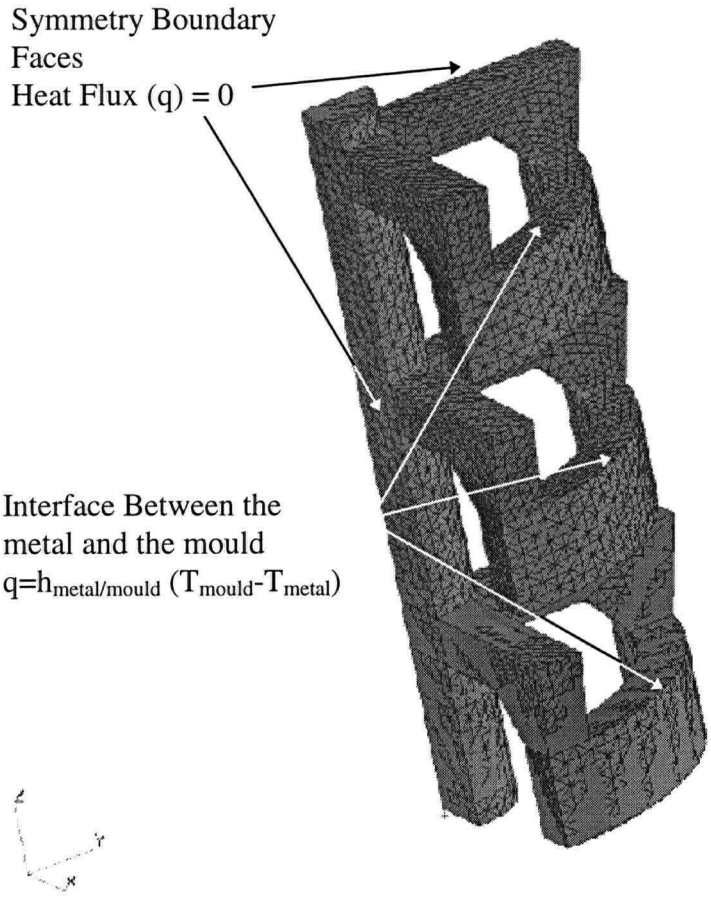

Figure 8-25 Three dimensional model diagram using three layers of four top feeding ingates to simulate the new casting configuration from Deloro Stellite. The mould is not included in this diagram.

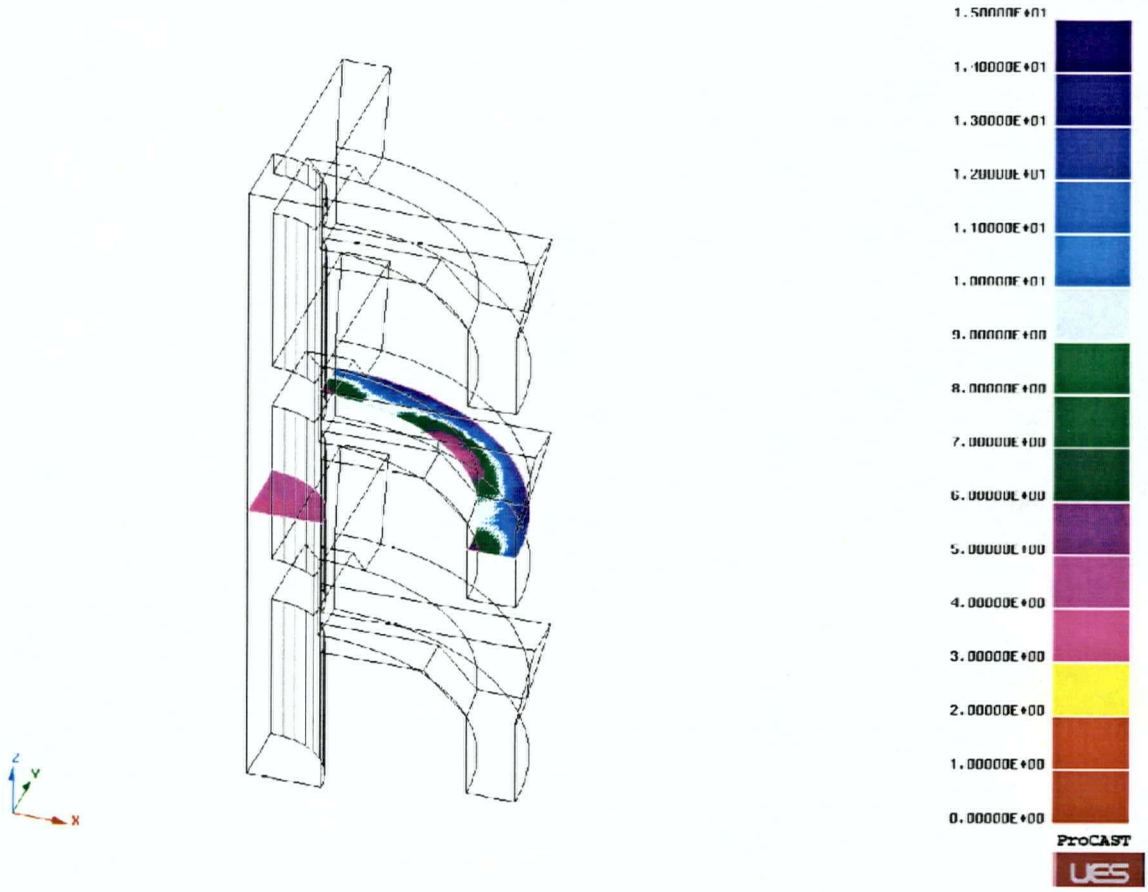

Figure 8-26 Thermal Gradient (°C/cm) Contour Plot through the mid-plane of the Diesel Valve Seal Casting using four top feeding ingates, model incorporates three layers of the casting, Thermal Gradient taken when an element obtains 70% volume fraction Solid (1260 °C).

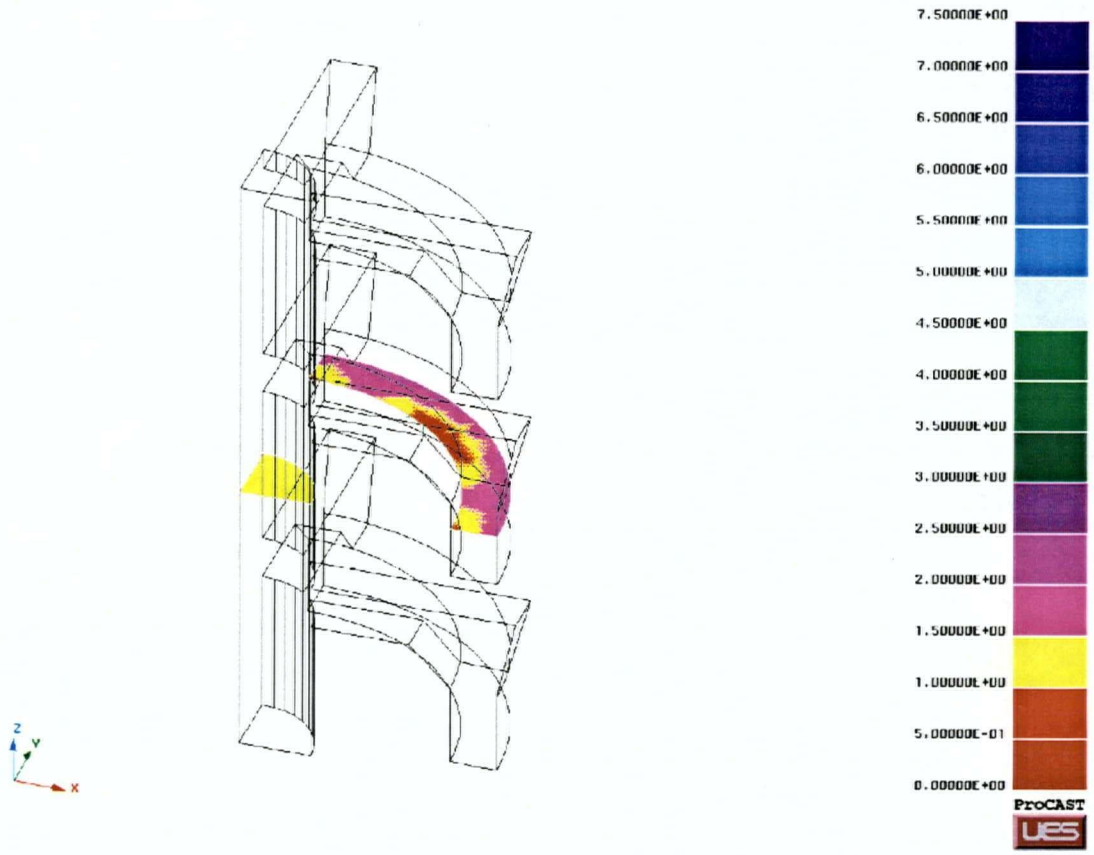

Figure 8-27 Niyama criteria ($°C^{1/2}$ $min^{1/2}$/cm) Contour Plot through the mid-plane of the Diesel Valve Seal using four top feeding ingates, model incorporates three layers of the casting, Thermal Gradient (°C/cm) taken at 1260 °C

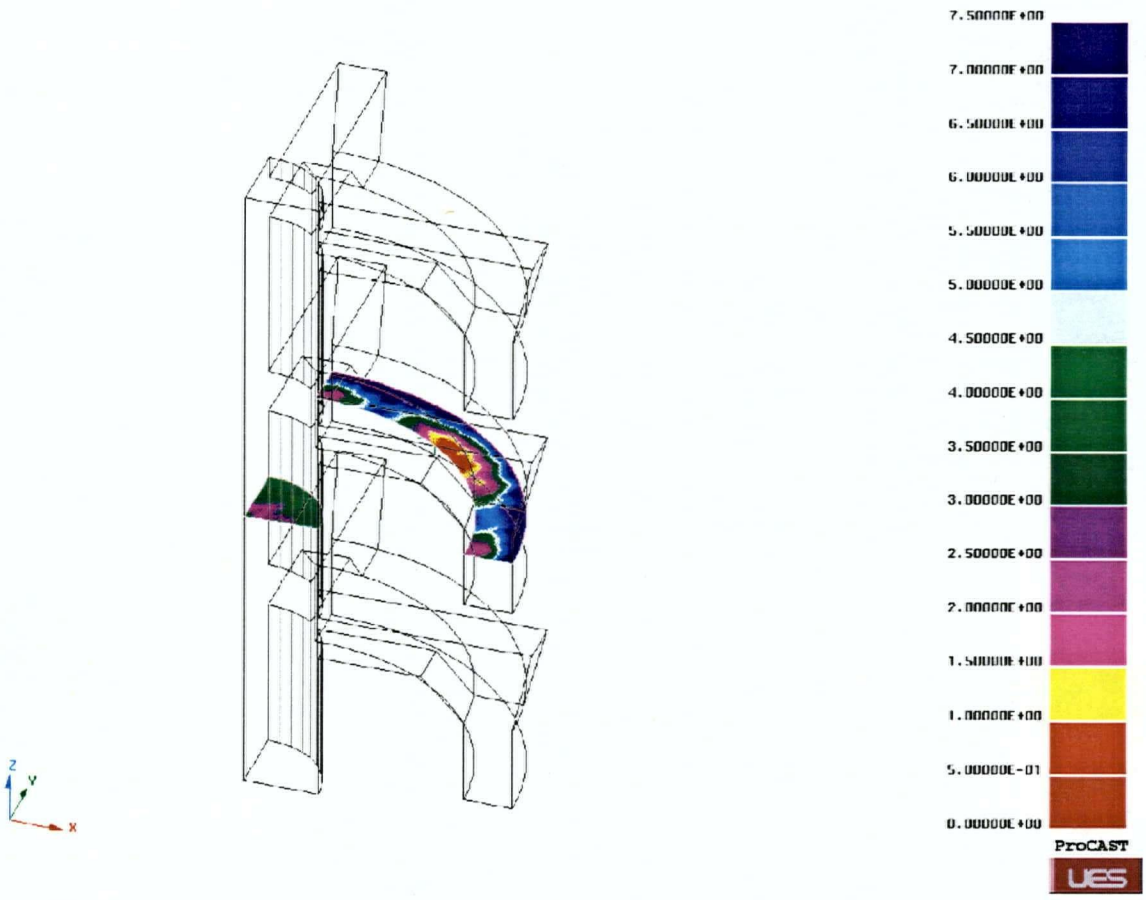

Figure 8-28 L.C.C. criteria (°C $min^{5/3}/cm^2$) Contour Plot through the mid-plane of the Diesel Valve Seal using four top feeding ingates, model incorporates three layers of the casting, Thermal Gradient (°C/cm) taken at 1260 °C.

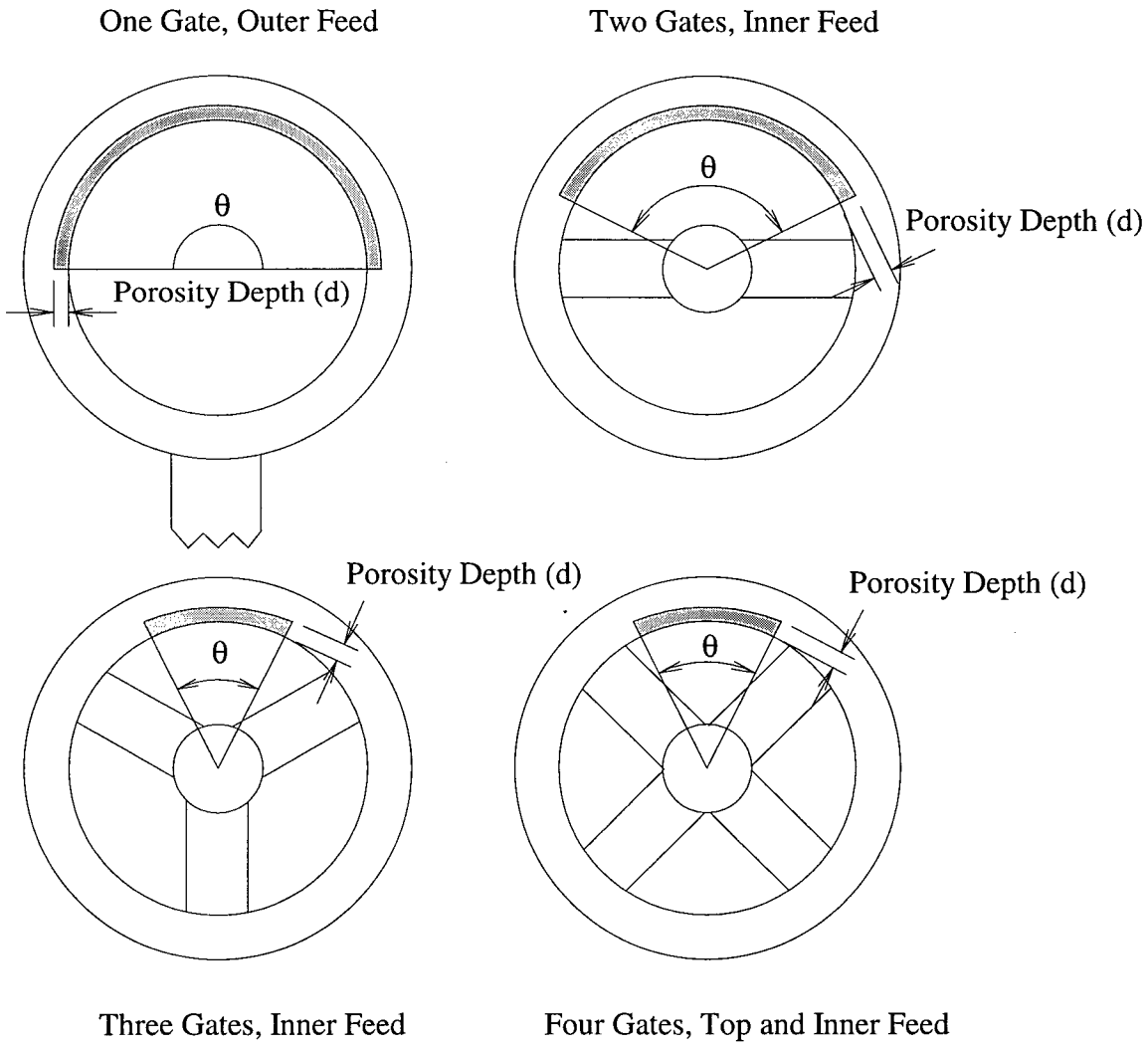

Figure 8-29 Schematic diagram of the diesel valve seal showing the circumferential angle and depth of porosity for the model results in Table 8-1.

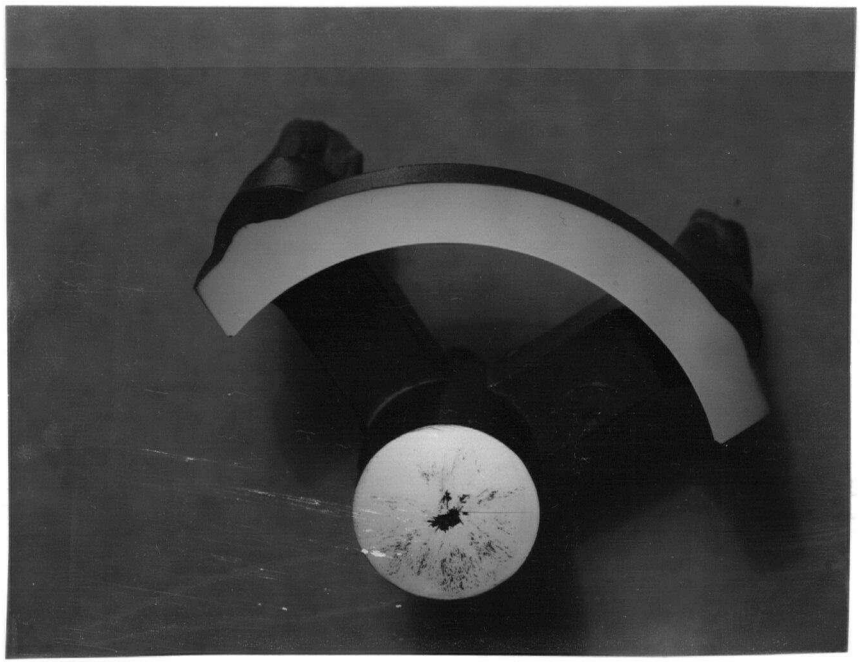

Figure 8-30 A quarter section of the new Diesel Valve Seal casting showing an obvious network of porosity in the downsprue. No visible porosity in the casting at this magnification.

Figure 8-31 A magnified photograph of microporosity found on the surface of the casting at Point A from Figure 8-30 . (unetched, mag.=12.8x)

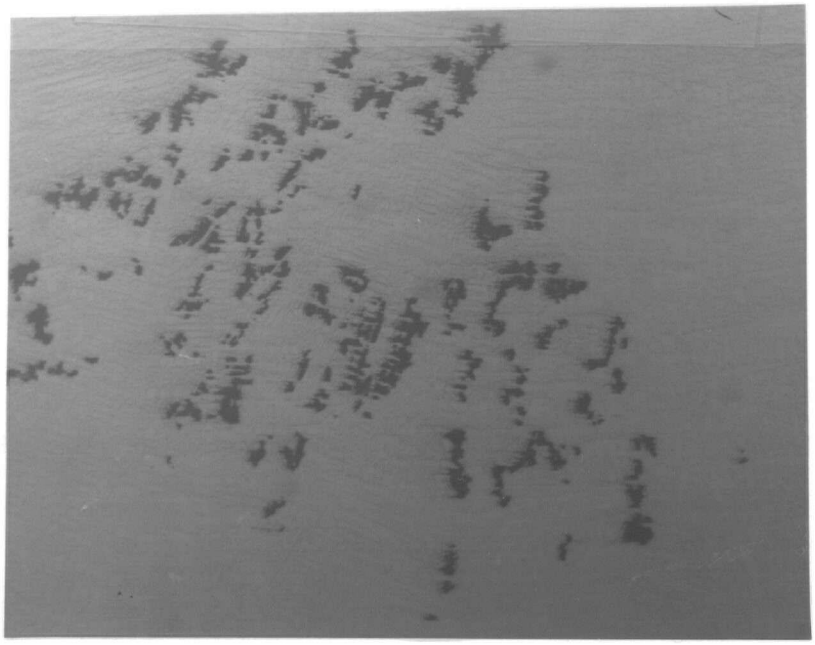

Figure 8-32 A close up of the porosity found in Figure 8-31. Porosity = 2.75 % area (unetched, mag.=50x)

9. Future Work

Thermal modeling is an excellent tool for cast/mould optimization, but it is only as effective as the boundary conditions employed. The sensitivity analysis showed that the casting parameters and consequently can influence the thermal history of the system which in turn influences the model for porosity prediction. This study assumed that the heat transfer coefficient at the mould/metal interfaces was homogeneous throughout the system. Realistically, however, this is not the case due to gap formation and metal impingement at the mould/metal interface. This can affect the local thermal history of the metal system and consequently influence the ability of the criteria to predict porosity in a complex casting geometry. To increase one's confidence in the model, one would have to increase the complexity of the models by taking into consideration gap formation and metal impingement on the mould and hence, the effective local interfacial heat transfer coefficient.

Another area of concern is the mould thermal physical properties. The investment mould consists of layers of stucco whose density changes throughout the wall thickness which influences the rate of heat diffusivity. It would be beneficial to study and understand the effect of heat diffusivity as a function of mould composition and density.

10. Summary and Conclusions

A simple casting was used to assess the sensitivity and quantify the metal and mould's physical properties, and the boundary conditions at the mould/metal and mould/air interfaces. The boundary conditions obtained were then applied to a complex model of a diesel valve seal fed by a single outer ingate. The porosity found in this casting was predicted successfully using the L.C.C. and the Niyama criteria.

The mould was then reconfigured on the computer. The downsprue was repositioned and the number of ingates was increased until a casting configuration was found with a "zero or close to zero" porosity prediction. A casting, consisting of four inner feed ingates and a downsprue located through the center of the ring predicted a close to zero porosity rating. At Deloro Stellite Inc., the diesel valve seal mould was reconfigured using four top feeding ingates and nine castings per stand. According to the Deloro Stellite personnel, this casting configuration resulted in a porosity free casting. However a model of the Deloro Stellite configuration was run, and a small pocket of porosity was predicted at the inner diameter metal surface between the ingates. Upon close inspection of the actual casting from Deloro Stellite, microporosity was found in this region.

In two separate cases, microporosity was predicted successfully in a Stellite Grade 3 investment casting system using the Niyama and the L.C.C. criteria. These two criteria were relatively simple to use because the only data required for their formulations was

derived from the thermal history of the casting (thermal gradient, solidification time, solidification velocity).

11. References

[1] Investment Casting Handbook 1980, Investment Casting Institute, 1979.

[2] Smart, R. F., Fifty Years of Investment Casting, Metallurgia, November, 1985, pp. 458-459.

[3] Campbell, J., Feeding Mechanisms in Castings, AFS Cast Metals Research Journal, 1969, vol. 5., no. 1, pp. 1-8.

[4] Kubo, K. and Pehlke, R. D., Mathematical Modeling of Porosity Formation in Solidification, Metallurgical Transactions, Vol. 16B, June, 1985, pp. 359 - 366.

[5] Piwonka, T. S. and Flemings, M.C., Pore Formation in Solidification, Trans. of the Met. Soc. of AIME., Vol. 236, 1966, pp. 1157 - 1165.

[6] Davies, V. De. L., Feeding Range Determination by Numerically Computed Heat Distribution, AFS Cast Metals Research Journal, June, 1975, Vol. 11, pp. 33-44.

[7] Minakawa, S., Samarasekera, I. V., and Weinberg, F., Centerline Porosity in Plate Castings, Metallurgical Transaction B, Vol. 16B, 1985, pp. 823 - 829.

[8] Suri, V. K., Paul, A. J., El-Kaddah, N., and Berry, J. T., Determination of Correlation Factors for Prediction of Shrinkage in Castings – Part I: Prediction of Microporosity in Castings; A Generalized Criterion, AFS Transactions, 1994, pp. 861 - 867.

[9] Pellini, W. S., Factors Which Determine Riser Adequacy and Feeding Range, AFS Transactions, 1953, pp. 61 - 80.

[10] Bishop, H. F. and Pellini, S., The Contribution of Riser and Chill-Edge Effects to Soundness of Cast Steel Plates, AFS Transactions, 1950, pp. 185 - 197.

[11] Niyama, E., Uchida, T., Morikawa, M., and Saito, S., Predicting Shrinkage in Large Steel Castings from Temperature Gradient Calculations, AFS International Cast Metals Journal, June, 1981, pp. 16 - 22.

[12] Niyama, E., Uchida, T., Morikawa, M., and Saito, S., A Method of Shrinkage Prediction and Its Application to Steel Casting Practice, AFS International Cast Metals Journal, Sept., 1982, pp. 52 - 63.

[13] Lee, Y. W., Chang, E., and Chieu, C. F., Modeling of Feeding Behavior of Solidifying Al-70Si-0.3Mg Alloy Plate Casting, Metallurgical Transactions B, 1990, pp. 715 - 987.

[14] Minakawa, S., Samarasekera, I. V., and Weinberg, F., Centerline Porosity in Plate Castings, Metallurgical Transaction B, Vol. 16B, 1985, pp. 823 - 829.

[15] Deloro Stellite Engineering Specification No 4521B, April 6, 1993, Preparation and use of Cobalt Aluminate "Blue" Primary Coat.

[16] Deloro Stellite Engineering Specification No 4523C April 6, 1993, Preparation and Use of Fascote™ Back-Up Coatings.

[17] Sairset Material Data Sheet, A. P. Green Refractories Co., Mexico, Missouri, USA, May, 1988.

[18] Deloro Stellite Engineering Specification No 4500 Series.

[19] ProCAST User's Manual, Version 2.2, UES, Inc., 1994, pp. 288 - 289.

[20] Dominic, B, Mathematical Modeling of Heat Transfer in the Vacuum Investment Casting of Superalloy IN718, Masters' of Applied Science Thesis, UBC, December, 1993.

[21] Thermal Conductivity Metallic Elements and Alloys, Thermophysical Properties of Matter, IFI/Plenum, New York-Washington, Volume 1, 1970.

[22] Specific Heat Metallic Elements and Alloys, Thermophysical Properties of Matter, IFI/Plenum, New York-Washington, Volume 4, 1970.

[23] Handbook of Thermophysical Properties of Solid Materials, Alloys, The Macmillan Company, New York, Volume II, 1961.

[24] Engineering Alloys Digest Inc., New Jersey, August 1961.

[25] Okazaki, M., Takahashi, J., Kimura, H. and Ida, K, Estimation of Solidification Time During Casting by Use of a Heat Transfer Model, Journal of Dentistry Res., October, 1982, pp. 1188 - 1191.